UNIVERSITY OF CALIFORNIA,
IRVINE

Assaying mitochondrial metabolism and morphology through super-resolution microscopy

DISSERTATION

submitted in partial satisfaction of the requirements
for the degree of

DOCTOR OF PHILOSOPHY

in Biomedical Engineering

by

Chia-Hung Lee

Dissertation Committee:
Professor Peter J. Burke, Chair
Professor Michelle Digman
Professor Gregory Brewer

2024

DEDICATION

In the hopes that this work may in some way contribute

to the exploration of mitochondrial metabolism.

I dedicated this work to my dear family

MingChe, XiaoChi, ChiaEn, Vicky, Stella, Zoey,

and friends

ChiaWei, Evan, Ken, Todd, Sungsik, Lindsay, Song, Charmeine, Becky, Sangjun, Dandan,

for their company and support in this fantastic journey.

TABLE OF CONTENTS

Page

LIST OF FIGURES

Page

LIST OF TABLES

Page

ACKNOWLEDGEMENTS

I wish to thank Dr. Peter J Burke, my committee chairman and research advisor for his countless hours of reflecting, reading, encouraging, and most of all patience throughout the entire process. I also wish to thank my committee members Dr. Michelle Digman and Dr. Gregory Brewer, who were more than generous with their expertise and precious time.

I would like to thank my school division and all funding sources for allowing me to conduct my research and providing any assistance requested. Special thanks go to the members of the BME department for their continued support.

I would like to acknowledge and thank my collaborators, Dr. Douglas C. Wallace, Dr. Kamel Haddadi, Dr. JiangHong Rao, Dr. Yumay Chen, Dr. Phang-Lang Chen, and Sangjun Noh for their support and guidance in all the research projects we have done in this thesis. Their excitement and willingness to provide feedback made the completion of this research an enjoyable experience.

VITA

Chia-Hung Lee

EDUCATIONS

2024	Ph.D. in Biomedical Engineering, University of California, Irvine
2021	Teaching Assistant, Graduate School of Biomedical Engineering, University of California, Irvine
2020	Data Scientist Intern, Medtronic Inc.
2017-18	R&D Engineer, Quark Biosciences Inc.
2015	M.S. in Mechanical Engineering, National Tsing Hua University
2013	B.S. in Biomedical Engineering, National Tsing Hua University

FIELD OF STUDY

Mitochondrial ultrastructure and metabolism, Electrophysiology, Super-resolution microscopy, Photobleaching and phototoxicity, Microfluidics, Bio-image analysis

PUBLICATIONS

1. **Chia-Hung Lee**, Douglas C. Wallace, and Peter J. Burke, "Photobleaching and phototoxicity of mitochondria in live cell fluorescent super-resolution microscopy", *Mitochondrial Communications*, 2024.
2. **Chia-Hung Lee**, Douglas C. Wallace, and Peter J. Burke, "Super-Resolution Imaging of Voltages in the Interior of Individual, Vital Mitochondria", *ACS Nano*, 2023.
3. **Chia-Hung Lee**, Yumay Chen, Ping Wang, Douglas C. Wallace, and Peter J. Burke, "A Three-Dimensional Printed Inertial Microfluidic Platform for Isolation of Minute Quantities of Vital Mitochondria", *Analytical Chemistry*, 2022.
4. **Chia-Hung Lee** and Peter J. Burke, "NanoStat: An open source, fully wireless potentiostat", *Electrochimica Acta*, 422, 2022.
5. Dandan Ren, Zahra Nemati, **Chia-Hung Lee**, Jinfeng Li, Kamel Haddadi, Douglas C. Wallace & Peter J. Burke, "An ultra-high bandwidth nano-electronic interface to the interior of living cells with integrated fluorescence readout of metabolic activity", *Scientific Reports*, 10, 2020.

ABSTRACT OF THE DISSERTATION

Assaying mitochondrial metabolism and morphology
through super-resolution microscopy
by

Chia-Hung Lee

Doctor of Philosophy in Biomedical Engineering

University of California, Irvine, 2024

Professor Peter J. Burke, Chair

Analysis of mitochondrial structure and function is increasingly being recognized as central to understanding human health and disease. Mitochondria ultrastructure has been extensively characterized with transmission electron microscopy (TEM) and CryoTEM in fixed cells. Yet mitochondria within tissue cells can have markedly different structures and functions. Only through imaging functional, intact mitochondria can one ascertain information about the electrophysiology of the organelle. Hence, there is a critical need to be able to characterize the structure and function of the individual isolated mitochondrion.

Our work aims to delve into procedures for characterizing the mitochondrial structure and function of isolated, functional mitochondria using super-resolution microscopy. This revealed that we can use super-resolution quantification of mitochondrial membrane potential using lipophilic cationic dye fluorescence to characterize the respiratory function of individual isolated, functional mitochondria in a way not possible in whole cells, potentially permitting elucidation of differences between individual mitochondria. Finally, by careful analysis of structure dyes and voltage dyes (lipophilic cations), we demonstrate that most of the fluorescent signal seen from voltage dyes is due

to membrane-bound dyes, and develop a model for the membrane potential dependence of the fluorescence contrast for the case of super-resolution imaging, and how it relates to membrane potential. This quantitative voltage-dependent membrane binding model explains why super-resolution images of lipophilic cationic dyes show strong intensity near the cristae and not in the matrix. This model enables quantitative imaging of super-resolution voltages inside functional, intact mitochondria with super-resolution.

INTRODUCTION

Mitochondrial ultrastructure and functions are tightly related. The mitochondrial inner membrane is highly in-folded into double membrane structures known as cristae. These cristae are closed at the intersection with the intermembrane space between the inner and outer mitochondrial membrane to create closed cristae lumens. The ETC pumps the protons into the cristae lumens on which the ATP synthases are bound. Cleavage of Optic atrophy-1 (OPA1), which is located at the site where the cristae lumen is closed, releases the protons and disrupts the coupling between the ETC and ATP synthase. The mitochondrial system is important for multiple other mitochondrial functions including mitochondrial membrane dynamics, thermogenesis, Ca^{2+} homeostasis, redox signaling, and apoptosis. Mitochondria ultrastructure has been extensively characterized with transmission electron microscopy (TEM) and CryoTEM in fixed cells. However, only by imaging functional, intact mitochondria can one ascertain information about the electrophysiology of the organelle. Because the cristae are about 100 nm wide, they cannot be studied with diffraction-limited microscopy. Recently, this limitation has been addressed using super-resolution microscopy. In this dissertation, we demonstrate approaches to assay isolated mitochondrial functions and ultrastructure using super-resolution microscopy.

In Chapter 1, we demonstrate using inertial microfluidics successfully separating intact mitochondria from cell lysates and validate their functions using the Seahorse XF analyzer. Our result showed a comparable respiratory control ratio (RCR) to the traditional method while we observed the more appearance of tubular isolated mitochondria, indicating a gentler isolating process to preserve intact mitochondria.

In Chapter 2, we introduce the NanoStat, an innovative, cost-effective, open-source potentiostat. Electrochemical techniques beautifully merge electricity with chemistry, providing an extensive array of tools for the quantitative analysis of various analytes crucial for sensing and biomedical diagnostics. This compact device, incorporating minimal integrated circuits and a handful of components, is notable for its web-server functionality accessible globally via a browser.

In Chapter 3, we demonstrate the procedure to quantify mitochondrial membrane potential using super-resolution microscopy with lipophilic cationic dye fluorescence, and to characterize the respiratory function of individual isolated mitochondria. By careful analysis of structure dyes and voltage dyes, we demonstrate that most of the fluorescent signal seen from voltage dyes is due to membrane-bound dyes, and develop a model for the membrane potential dependence of the fluorescence contrast for the case of super-resolution imaging, and how it relates to membrane potential.

In Chapter 4, we present empirical data on the effects of photobleaching and phototoxicity on mitochondria during super-resolution imaging of mitochondrial structure and function using Airyscan and the fluorescent structure dyes Mitotracker green (MTG), 10-N-nonyl acridine orange (NAO), and voltage dye Tetramethylrhodamine, Ethyl Ester (TMRE). We discern two related phenomena. First, phototoxicity causes a transformation of mitochondria from tubular to spherical shape, accompanied by a reduction in the number of cristae. Second, phototoxicity impacts the mitochondrial membrane potential. Through these parameters, we discovered that upon illumination, NAO is much more phototoxic to mitochondria compared to MTG or TMRE and that these parameters can be used to evaluate

the relative phototoxicity of various mitochondrial dye-illumination combinations during mitochondrial imaging.

In Chapter 5, we summarize and state the future direction to extend our studies in mitochondrial metabolism.

Chapter 1. A 3D PRINTED INERTIAL MICROFLUIDIC PLATFORM FOR ISOLATION OF MINUTE QUANTITIES OF VITAL MITOCHONDRIA

1.1 Introduction

Mitochondria play a critical role in life, death, and pathology.[1–6] Assays of mitochondrial function such as membrane potential, respiration rate, and pH provide a host of information about these electro-physiologically active organelles.[7,8] To dissect the function, it is necessary in many cases to remove mitochondria from cells or tissues for further analysis. Although contextual information is lost, significant control is gained, similar to how single-cell analysis provides important information about cellular biology, even though cells are removed from the organism.

Mitochondria burn dietary calories using oxygen to provide the chemical energy needed to do work, maintain ATP levels, and heat to maintain body temperature. As a toxic by-product, mitochondria produce much of the endogenous cellular oxygen radicals or reactive oxygen species, a process believed to eventually result in declining organ function, aging, and death.[9] A growing body of evidence suggests that the regulation of metabolism is important in an even wider variety of biological processes, including stem cell differentiation, cancer, [10] neurodegenerative diseases, and diabetes. [5,6,11,12] As a specific example, inheritance patterns of one of the electron transport chain complexes (complex II, succinate dehydrogenase) have identified succinate dehydrogenase as a tumor suppressor gene, although the mechanism that relates to the defect in this particular electron transport chain component and tumorigenesis is still not understood in detail. [6,13–21] We anticipate that the availability of improved tools for studies of bioenergetics to the broader biological community will enable these and other links to be explored in more meaningful ways, leading to further understanding of the links between energy, health, and disease.

Exquisite, precise studies of the electron transport chain are possible in isolated mitochondria, as opposed to whole, intact cells. The electron transport chain is a set of four mitochondrial inner membrane protein complexes that use the chemical energy stored in pyruvate to pump protons out of the inner matrix and maintain an electrochemical gradient across the mitochondrial inner membrane ($\Delta P = \Delta\Psi m + \Delta\mu H+$). $\Delta\Psi m$ is a voltage, whereas $\Delta\mu H+$ is a pH gradient (typically less significant). The fifth complex (ATP synthase) uses the membrane potential to drive the phosphorylation of ADP to ATP. The rate of mitochondrial respiration and the oxygen consumption of freshly isolated mitochondria is measured in many labs [22] using various substrates and inhibitors (as well as other regulatory chemistries, such as ATP/ADP ratio, Ca++, and other mimics of the cytoplasm) to differentiate the function of the five key complexes of the electron transport chain. [23,24] Although not identical to their exact behavior in intact cells, [22] these studies of each component of the electron transport chain allow exquisite, sensitive measures of mitochondrial components not possible in whole cells.

A traditional isolation process relies on mechanical lysis of the cell plasma membrane followed by a differential centrifugation. [23,25] The mitochondria are only viable for about an hour after this process (i.e., they consume oxygen, convert ADP to ATP, and sustain a membrane potential). There is significant risk to damage of the mitochondrial membrane

integrity. Common methods for mitochondria isolation are through the density-gradient centrifugation or immune-isolation method; both require processing such as cell lysis, fractionation, and purification and usually take around 2–3 h, while the isolated mitochondria are vulnerable and can only survive a few hours after sorting processes. In addition, the disruption and damage caused during centrifugation procedures to the fragile mitochondrial membranes could also harm its functionality. These become an obstacle for mitochondria research and clinical applications. As a result, it is critical to have a fast, stable, and validated technology to isolate and assay vital mitochondria from cells and tissues.

Reproducibility of mitochondrial assays is also an issue. In a study published in 2004, [26] a set of tissue from the bovine skeletal muscle was divided and sent to 14 different labs around Europe. In this blind study, each lab was asked to assay the activity of the mitochondrial complexes using spectrophotometry. Note that this did not require intact organelles, only active enzyme complexes. Thus, this test was less stringent than the technology we aim to present here, which is to assay the respiration of an intact organelle. Nevertheless, in spite of this very straightforward assay, the labs came up with varying results that were off in the simple metric of enzyme activity by up to an order of magnitude. These are assays on which clinical decisions are made, and research is based on these assays. Therefore, we claim that there is a reproducibility issue with mitochondrial functional assays.

Microfluidic isolations using inertial microfluidics for micrometer and sub-micrometer particles have been utilized in multiple biological applications in the past decade (e.g., WBC and RBC sorting, CTC detection, and viral recovery from blood [27–35]). Among all applications, inertial microfluidics stands out as one of the most promising solutions for mitochondria isolation without damage to the membrane and function. [29] The mechanism of inertial microfluidics separating particles utilizes the balancing of inertial lift force and the "Dean" drag force to drive particles to different equilibrium positions in the microchannel based on their sizes. To manipulate single-micron size or sub-micron size particles, further investigation in channel geometry designs has been done, for example, spiral, serpentine, or trapezoidal spiral channel designs to induce secondary flow and thus enhance the Dean drag forces for small particle concentrations. However, the complexity of the channel structure brings up difficulties in traditional SU8 photolithography fabrication. Recently, additive manufacturing has become a powerful platform to fabricate three-dimensional (3D) functional microfluidic systems from polymeric materials. [33] Benefiting from the stereolithography apparatus (SLA) technique, the resolution for microfabrication and prototyping has reached under 100 μm, which has met the criteria for most microfluidic applications.

Tesauro et al. [29] demonstrated the feasibility of using inertial microfluidics to isolate mitochondria from cell lysates. They followed the SU8 soft-lithography techniques generating a four-loop spiral geometry PDMS channel and were able to reach up to 90% isolation efficiency. In their research, the apurinic/apyrimidinic endonuclease 1 (APE1) activity of unsorted and sorted liver mitochondria was measured to validate whether the retrieved mitochondria retain the biological functionality. However, to evaluate the dysfunction of isolated mitochondria, the gold standard is through measurements of mitochondrial respiration as electron transport chain and oxidative phosphorylation reflect

the concerted function of intact, fully functional mitochondria. The isolation procedure can easily leave functional "pieces" of mitochondria such as active enzymes, but only respiration demonstrates the function of the entire organelle. Until now, all previous papers related to mitochondria isolation using inertial microfluidics demonstrated only proof of vitality and function of mitochondria, such as the ATP assay, ROS measurement, or MitoTracker dyes.

To quantify organelle integrity, the respiratory control ratio (RCR) is usually used. [7,8] This empirical parameter is based on the observation that mitochondria damaged during isolation show an increased proton leak of the inner membrane as compared to undamaged mitochondria, hence an increased state 4 respiration rate. The RCR is typically defined as the ratio of the state 3 to state 4 respiration rate (achieved using different substrates for the electron transport chain). The RCR assay thus measures the "leakage" of membrane potential quantitatively: Higher RCR means less damage to the mitochondria during the isolation process.

In this research, we demonstrate a fast and easy-to-use 3D printed microfluidic platform for mitochondria isolation based on inertial microfluidics. We present and quantify the RCR of this isolation technology and protocol and demonstrate that it produces vital mitochondria from cell lysates with the same quality (measured via the RCR) as mitochondria isolated using benchtop centrifuges. The advantages of this are (i) automated vs manual centrifugation step, reducing operator dependence of the process; (ii) ability to isolate small quantities of mitochondria; and (iii) the possibility to integrate with other on-chip assays such as on-chip cell lysis, [36] mitochondrial sorting, membrane potential, pH assays, [37–39] and even single mitochondria respiration assays. [40] Additional possible advantages include the following: (i) Time to analysis from cell harvest to mitochondrial downstream functional analysis is dramatically shortened (a few minutes vs an hour) as compared to centrifugation and mechanical lysis. Once isolated, the mitochondria are immediately available for subsequent downstream analysis. (ii) Oxygenation stability. The samples are not subject to repeated cycles of hypoxia/normoxia, an inadvertent side effect of multiple centrifugation steps, and a potential complication for studies of metabolism. (iii) Thermal control. The demonstrated process allows control of the temperature during the isolation and analysis process. Many of the centrifugation processes require changes in temperature, and some assays do not allow temperature control at all. (iv) Mechanical protection. In contrast to mechanical centrifugation, the demonstrated process is extremely gentle.

The intended use case for this technology is where cell materials are sparse or rare, such as in patient biopsies or research applications where large quantities of the starting tissue are prohibitively expensive. Such may be the case, for example, in personalized medicine [41,42] where specific chemotherapies where mitochondria isolated from tumor biopsies are treated in vitro with different target chemotherapies to decide on a course of treatment for a patient. [43] Another example is in muscle biopsies of babies and young children, where the absolute minimum amount of tissue is desired in this painful procedure. Another example is in the case of assaying mitochondria from a single cell. None of the above use cases is possible with traditional isolation techniques based on differential centrifugation. All the examples above are enabled by the technology presented in this paper.

Separation Mechanism

In the Navier–Stokes equation at low Reynolds numbers, the Stokes (F = ma) terms are usually set to zero, which is equivalent to neglecting the effect of inertia on the fluid flow. However, in microfluidic systems, this is not completely justified. [28,44] While fluid flow remains laminar (since turbulence typically sets in at around R ~2000), non-trivial inertial effects become apparent and can be exploited and engineered. The key effect in curved microfluidic channels is that these inertial effects give rise to secondary flow effects not considered in most laminar flow applications, the most dominant being the generation of two symmetric vortices in the channel called "Dean's vortices". [45] The dimensionless "Dean number (D_e)" captures the magnitude of this effect. The calculation of De is given by

$$D_e = \frac{\rho U_f D_h}{\mu}\sqrt{\frac{D_h}{2R}} = R_e\sqrt{\frac{D_h}{2R}}$$

where ρ is the density of the fluid medium, Uf is the average fluid velocity, μ is the fluid viscosity, R is the radius of curvature of the channel, Dh is the hydraulic diameter of the channel, and Re is the flow Reynolds number. In our system, we estimate that Re is around 6.65 and De is around 0.9 (Supporting Information).

In spiral or curvilinear channels, the interplay of the net inertial lift force (F_L) and Dean drag force (F_D) gives rise to the Dean coupled inertial migration of particles. The ratio of inertial lift force to Dean drag force is a key parameter (R_f) to characterize particle inertial focusing. This inertial force ratio, $R_f = a^2R/D_h^3$, is useful for predicting particle behavior where R is the largest radius of curvature in the system. For particle focusing in a continuously curving channel, it is observed that the Rf needs to be > 0.04 [28] (or $a/D_h > 0.07$ [46]). In our designed channel size, the a/D_h ratio is around 0.01 for isolated mitochondria, which indicates that the inertial lift forces will be small on particles with sizes as small as mitochondria. Therefore, instead of concentrating on the mitochondria, we are trying to concentrate the large debris and thus separate them from mitochondria. We choose the double-inlet Spiral/Dean flow fractionation (DFF [47]) to achieve the isolation of smaller micro- or nanometer-sized elements through well-controlled Dean migration. We also discuss the friction effect due to the channel roughness in the Supporting Information.

A particularly important use case is the separation of particles based on their physical properties [27,29–35] such as size, charge, mass, etc. The Dean flow-based force will exhibit different drags on different particle sizes as they sample different flow velocity field profiles. This has been exploited for two types of separation: "soft" and "hard" particles. The "hard" particles are latex beads done mostly for test and demonstration purposes. The "soft" particles are blood cells, which have a deformable lipid bilayer cell wall. Only one case of mitochondria has been shown. Mitochondria can be considered somewhere between soft and hard as the lipid bilayer is rich in cardiolipin giving different mechanical properties as compared to cell walls and because the viscosity of the internal matrix of mitochondria is much higher than the cytoplasm. These are only qualitative statements as a detailed mechanical model of the deformation properties of isolated mitochondria has never been published and is not known quantitatively. For this reason, also, one should not expect

experiments in either cells or latex beads to be representative of mitochondria separation experiments.

In spite of this uncertainty, Tesauro et al.'s report [29] has shown interior microfluidic separation, but they did not show the vitality of the isolated mitochondria and they used photolithography. In our work, we have scaled the channel dimensions of their design by 2× (h = 50–100 μm, w = 100–200 μm) to relax the manufacturing tolerance due to the simplified 3D printing technology we used. This gave rise to comparable flow velocities; the channel area was 4× larger in our work, and the optimal flow rate was 3× larger (60 vs 20 μL/min). Their hydraulic diameter was 66.7 μm vs ours at 133.3 μm. Therefore, the mechanism of separation in our work vs Tesauro et al.'s is expected to be the same. In spite of a lack of a detailed quantitative model of the separation mechanism, the method works, once optimized for flow rates, and does not damage mitochondria, in our extremely low cost to produce 3D printed channels. We now discuss in more detail the inertial lift force in our geometry. The inertial lift force is predicted to asymptotically scale as U2/H2 for fixed particle size and medium density, [28,48] where U is the mean flow velocity and H is the channel dimension. Therefore, the lift force for our geometry is comparable to that of the narrower channels in Tesauro et al.'s since our H is 2× larger, and our U is 3× larger. Thus, in our work, consistent with Tesauro et al.'s, the inertial lift force for mitochondrial particles is sufficient for separation and concentration.

The mechanism of separation is a balance of the inertial lift force and the Dean drag force. In contrast to prior work where separation of particles of different sizes is achieved, we only seek to separate mitochondrial particles from everything else, similar to the way a high g centrifuge separates mitochondrial particles but does not sort particles based on size. The detailed balance of forces can in principle be simulated and calculated, but this is notoriously difficult to perform precisely. For example, in Di Carlo's report [28] and Zhang et al.'s report [44], it is stated that "the exact mechanism and location of the superposition of secondary flow and lift effects are complex and unknown experimentally and theoretically such that I currently can only speculate in Figure 1-5 on the precise combined behavior." Thus, similar to the literature, we are only demonstrating that the two forces can be balanced but not providing a detailed location within the channel that they are focused on the equilibrium concentration. In contrast to other literature, we are not separating different particles of the minor difference in size but only separating mitochondrial particles from much larger cellular debris such as the nucleus as well as much smaller molecular contents, such as RNA and ribosomes.

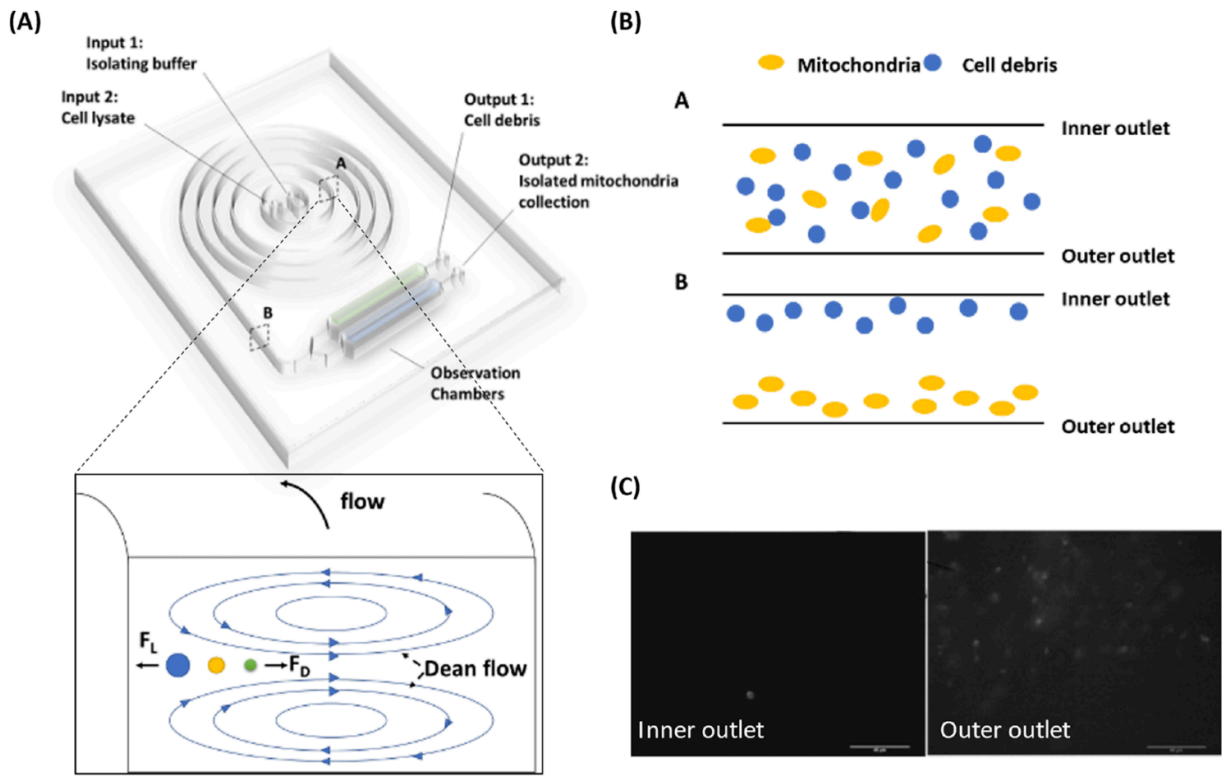

Figure 1-1. The schematic figure for the inertial microfluidic platform of mitochondria isolation. (A) The cross-sections A and B show the migration of isolated mitochondria undergoing secondary flow and (B) the final distribution of mitochondria and cell debris. (C) Collection of isolated mitochondria stained with MitoTracker Green from the inner outlet and from the outer outlet (40× objective, scale: 20 µm).

1.2 Materials and Methods

1.2.1 Platform Design and Fabrication

In this study, an inertial microfluidic platform was fabricated using a high-resolution SLA 3D printer (Peopoly Moai) featuring 70 µm XY resolution and 25 µm Z resolution (Figure 1-1 and Figure 1-2). The platform was first drafted using commercial CAD drawing software (Solidwork) and transformed into STL format. The file was then sliced in the Z direction using Ultimaker Cura software. The sliced file was then sent to the 3D printer with a UV wavelength of 405 nm. The UV light was projected from the bottom of the resin bath. Afterward, the platform was cleaned with ethanol and exposed to a UV light with 405 nm wavelength within a curing chamber for the post-curing process. The channel width was 200 µm with 500 µm spacing in between, and the channel height was 100 µm. The design was based on the principle described in Bhagat et al.'s report [49] with a/D_h ratio of ~0.01, where a is the diameter of the particle and Dh is the hydraulic diameter of the channel. Later, tubes were connected to the microchannel by tweezers and sealed with epoxy instant mix glue (Loctite) to form the closed microchannels. ARcare 90445, a medical grade pressure-sensitive double-sided adhesive (Adhesive Research), was attached onto the platform to seal and form the closed channel, while the other side was attached to a rigid and transparent

plastic plate to avoid tape debonding caused by high injecting pressure during fluidic manipulation.

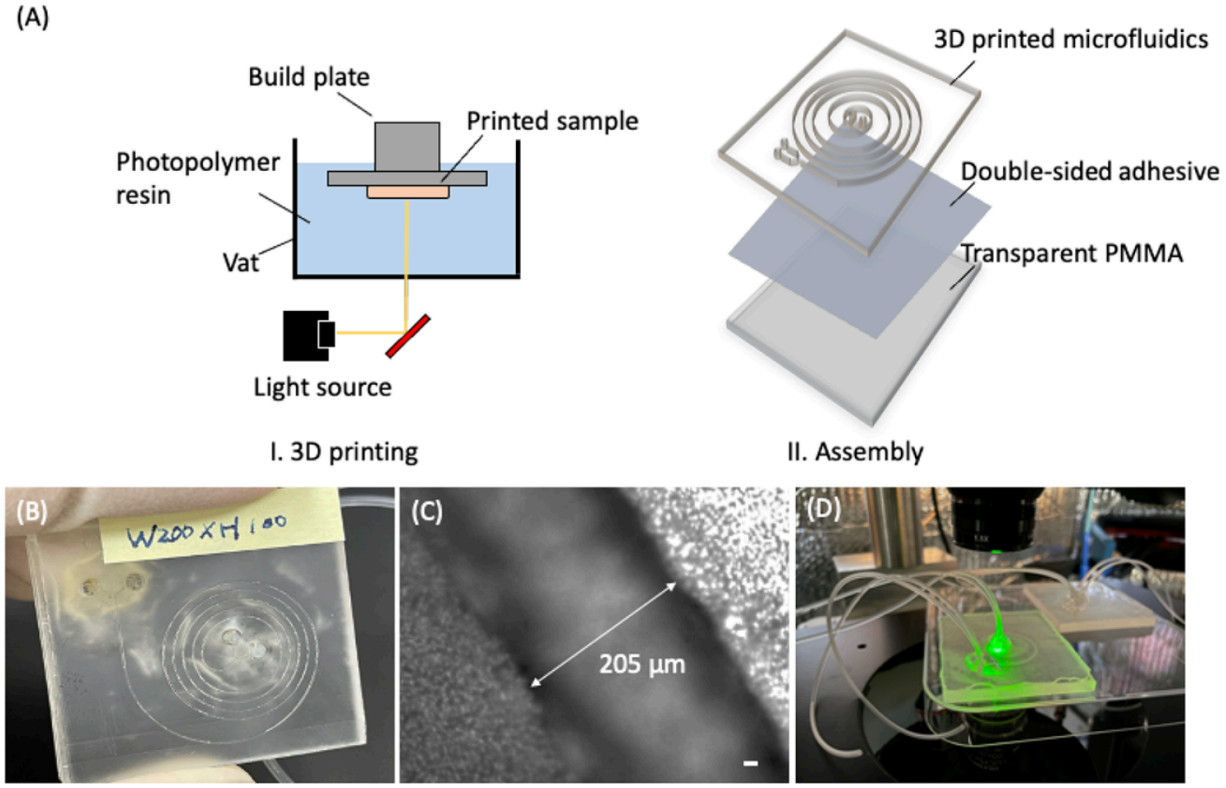

Figure 1-2. Fabrication and imaging setup. (A) The manufacturing process of (I) 3D printing and (II) microfluidic platform assembling. (B) Picture of the 3D printed microfluidic platform. (C) Channel dimension checks under the microscope (channel width: 205 µm; 20×, scale: 20 µm). (D) Microfluidic platform on the imaging system.

1.2.2 Preparation of Mitochondria from the HeLa Cell Culture

HeLa cells used in this research were purchased from ATCC. The cells were cultured for 2–3 days in 75 cm^2 tissue flasks at 37 °C and 5% CO2. MitoTracker Green (ex/em 490/516 nm) at 100 nM was added and incubated for 30 min. The protease trypsin was used to detach cells from the flask, and the same amount of medium was later added to stop the reaction. The cell collections were centrifuged for 5 min at 1000g, and the pellets were resuspended in ice-cold RBS buffer (5 mM KCl, 1 mM $MgCl_2$, 20 mM HEPES (pH 7.0)) and incubated on ice for 10 min. After incubation, the solution was transferred into a glass homogenizer and we performed 40 strong strokes separately using loose and tight stroking. The homogenate was then recentrifuged at 12,000g for 20 min at 4 °C. The collected supernatant was the isolated mitochondria. Figure 1-3A shows the common procedures of mitochondria isolation through differential centrifugation, immune capturing with magnetic microbeads, and inertial microfluidics. Fluorescence imaging of isolated mitochondria from cultured cells was used to observe the migration results under inertial focusing.

1.2.3 Preparation of Mitochondria from the Mouse Heart

A fresh mouse cardiac tissue was retrieved using established methods. [50] After retrieval, the minced tissue was transferred into a falcon tube with 5 mL of ice-cold RBS buffer (5 mM KCl, 1 mM $MgCl_2$, 20 mM HEPES (pH 7.0)) added and the tube was then incubated on ice for 10 min. After incubation, the solution was transferred into a glass homogenizer and we performed 40 strong strokes separately using loose and tight stroking. Next, we centrifuged the homogenate at 1000g for 5 min at 4 °C to remove large-scale debris. Half of the supernatant was collected for inertial microfluidic testing use (Solution B), and the rest was recentrifuged at 12,000g for 20 min at 4 °C as a control sample of purified isolated mitochondria using standard methods. The pellet was collected and resuspended in RBS buffer (Solution A) as the comparison group (Figure 1-3B). All animal experiments were carried out in an ethical manner, in accordance with the protocols approved by the IACUC committees at the University of California, Irvine.

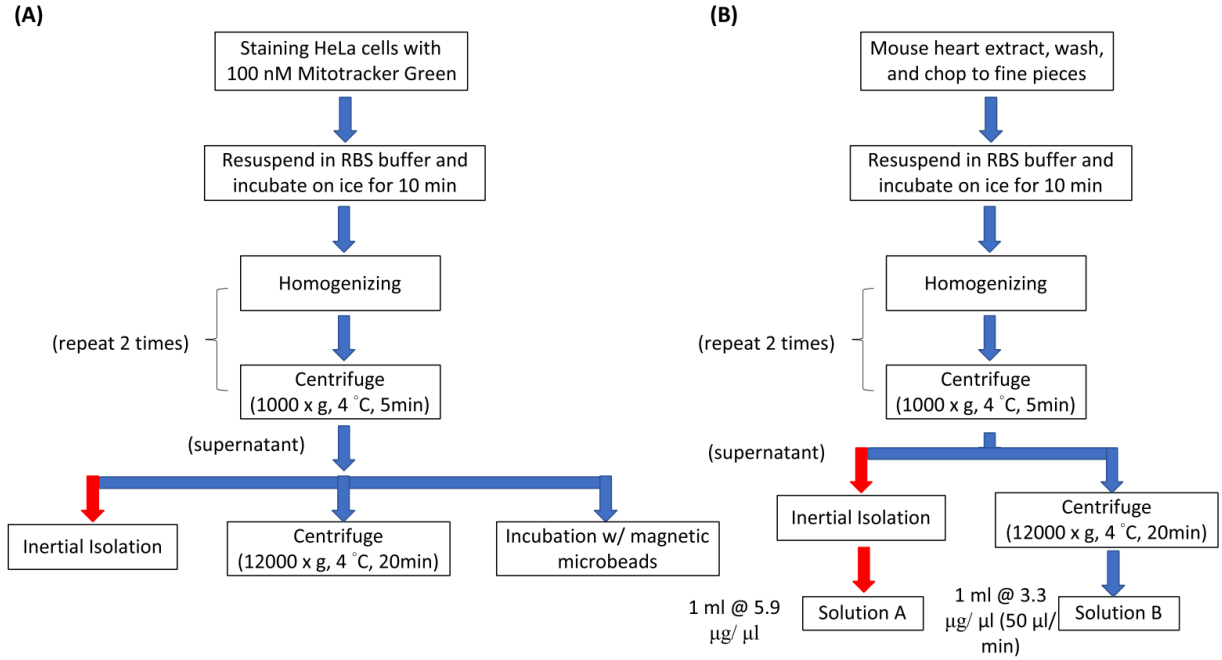

Figure 1-3. Protocols for isolation of mitochondria retrieved from (A) cell culture and (B) fresh mouse cardiac tissues.

1.2.4 Microscopy and Image Analysis

Slides were analyzed with an Olympus IX71 microscope using 20× (LUCPlanFLN, 20×, NA = 0.45, Olympus) and 40× objectives (PlanApo 40×, NA = 0.95, Olympus). The fluorophores were excited by UV LEDs (M490L3, 350 mA, THORLABs). Fluorescence signals from MitoTracker Green were selectively filtered through a dichroic and bandpass filter (excitation: 490 nm, emission: 516 nm).

1.2.5 Mitochondria Respiration Assay

An Agilent Seahorse XFe24 analyzer was used for measuring the oxygen consumption rate (OCR) of isolated mitochondria according to established protocols. [51] This provides a

standard and comprehensive method of assessing the key parameters of mitochondrial function in isolated mitochondria: basal respiration, ATP-linked respiration, H+ (proton) leak, maximal respiration, spare respiratory capacity, and non-mitochondrial respiration. The respiratory control ratio (RCR) can easily be calculated as the ratio of state 3 to state 4 respiration.

After the protein concentration is determined, aliquots of the isolated mitochondria solution were inserted into the wells (10 μg/well, at least 4 wells/sample) at a final concentration of 10 μg of mitochondria in 50 μL of 1× MAS buffer (Sucrose 70 mM, Mannitol 220 mM, KH_2PO_4 10 mM, $MgCl_2$ 5 mM, EGTA 1 mM, fatty acid free BSA 0.2 %, PIPES 25 mM, pH 6.8 at 37 °C) with substrates (5 mM pyruvate and 5 mM malate). Mitochondria were plated onto a Seahorse culture plate and centrifuged at 2000g for 20 min at 4 °C. MAS (450 μL, 1×) was added to each well and incubated at a 37 °C, non-CO2 incubator for 8 min.

The four injection ports were filled with (i) 55 μL, 40 mM ADP, (ii) 60 μL, 25 μg/mL oligomycin, (iii) 65 μL, 40 μM FCCP, and (iv) 70 μL, 40 μM Rotenone. The experimental procedure is described below:

1. Measuring the basal respiration of isolated mitochondria.
2. Adding ADP, rapid oxygen consumption, and the formation of ATP (state 3).
3. Adding oligomycin, the ATP synthesis inhibitor (state 4).
4. Adding FCCP, the uncoupler.
5. Adding Rotenone, interfering with complex I in the ETC.

1.2.6 Definition of Isolation Efficiency

To determine the isolation efficiency of the inertial microfluidic method, 1 mL of the retrieved mitochondria concentrations from both inner and outer outlets was measured using the Bradford assay. For example, the isolated mitochondria concentrations under a flow rate of 50 μL/min were measured to be 1.58 μg/μL in the inner outlet and 3.33 μg/μL in the outer outlet. The isolation efficiency was then defined as 3.33/(1.58 + 3.33) = 68%. To determine the isolation efficiencies versus the flow rates, three distinct measurements were examined under each flow rate.

1.3 Results and Discussion

The retrieved amount of the isolated mitochondria concentration using the inertial microfluidic method relies on (i) the concentration of lysate and (ii) the length of isolating time. Unlike the centrifugation method having a fixed isolation time, the inertial method is more suitable for a small amount of requirements (10 pg of mitochondria can be sorted out in 5 s with the inertial microfluidic method compared to 20 min in the traditional centrifugation method).

1.3.1 Isolation Efficiency vs Flow Rate

Although there has been extensive theoretical and computation analysis of ideal submicron particles such as latex beads, [27–35] the exact parameters for mitochondria isolation need to

be determined empirically due to the lack of models with enough sophistication to predict quantitative yield. Thus, the optimized flow rate for sorting was determined empirically. From our experiences, an average of up to 73 % of mitochondria could be retrieved from the inner outlet when using a flow rate of 50 µL/min (Figure 1-4).

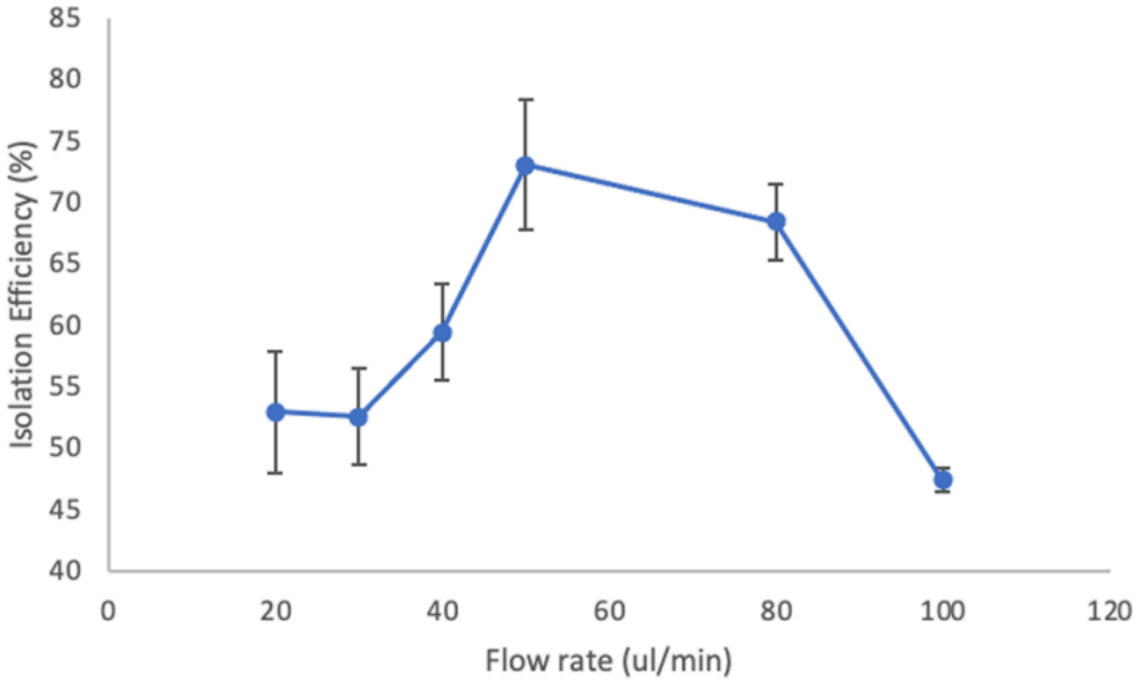

Figure 1-4. Isolation efficiency of mitochondria under different flow rates using inertial microfluidics.

1.3.2 Oxygen Consumption Rate for Isolated Mitochondria

To further investigate whether the retrieved mitochondria retain their biological functionality, an Agilent Seahorse XFe24 analyzer was used for measuring the oxygen consumption rate (OCR) of isolated mitochondria. The isolated mitochondria under 50 µL/min flow rate were tested and compared to the traditional centrifugation method. A measure of "coupling" that retains utility is the respiratory control ratio (RCR), an empirical parameter frequently used for assessing the integrity of the mitochondria preparation (Figure 1-5).

The respiratory control ratio (RCR) was from state 3 (ADP)/state 4 (oligomycin). The RCR value from the mitochondria from the control group is used as the indicator of the quality of the mitochondrial preparation. As the result showed, the RCR values are calculated to 3.9 ± 0.7 and 3.8 ± 1.5 corresponding to isolated mitochondria that undergo the centrifugation method and inertial microfluidic method with 50 µL/min, respectively. The error bars are according to the measurements of multiple wells. This work has shown for the first time the use of microfluidic centrifugation for isolation of vital mitochondria. The RCR is as good as or better than traditional differential centrifugation.

The fact that the results from inertial microfluidic and traditional centrifugation give rise to no difference in the respiration results in Figure 1-5 is the most important point of this work:

This proves that the inertial microfluidic method, with all of its advantages (discussed in more detail below), produces isolated mitochondria with the same quality and quantitative properties of mitochondria isolated and studied with traditional centrifuges, a body of knowledge that has been proven over 30 years of research and thousands of papers. [7]

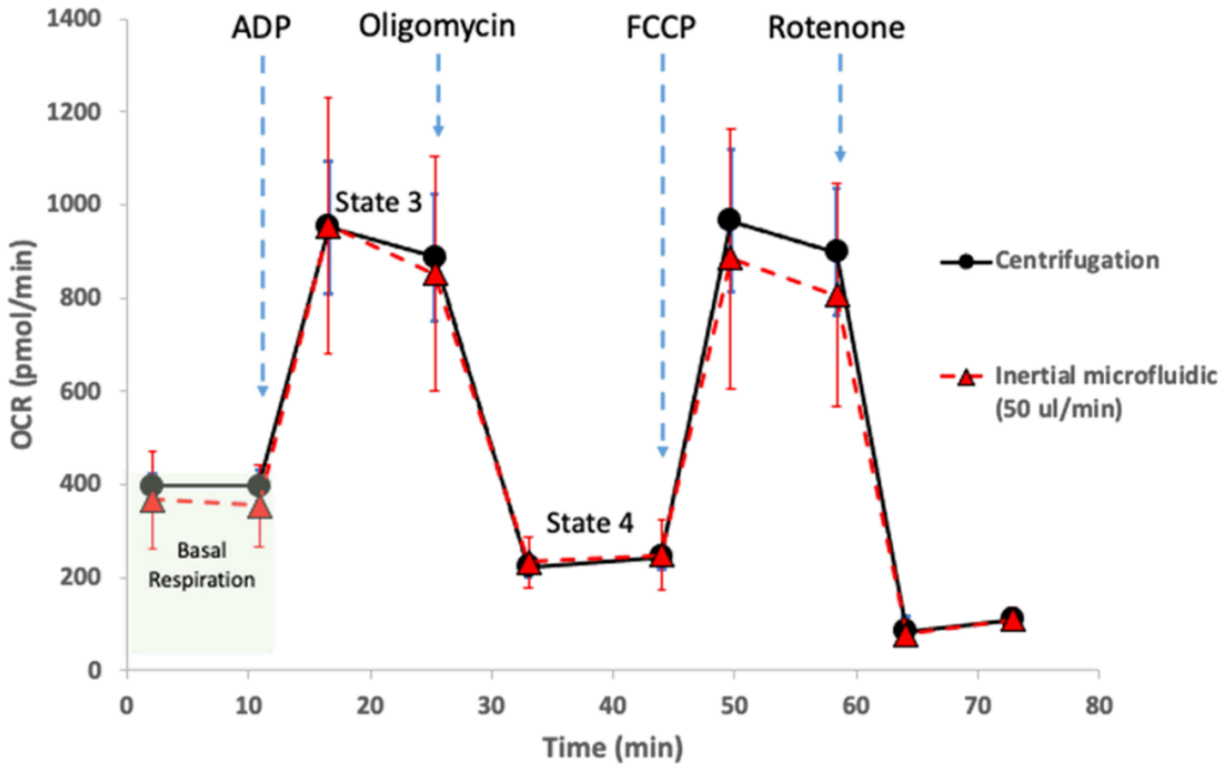

Figure 1-5. Oxygen consumption rate (OCR) of isolated mitochondria under different isolation procedures and conditions.

1.3.3 Comparison to other isolation methods

The motivation of this work is to build a fast and solid method for a small amount of requirements of isolated mitochondria. In Table 1-1, we compare and summarize our proposed inertial microfluidic method to the differential centrifugation (DC), antibody-coated magnetic beads, affinity purification using magnetic beads, and MITO-Tag.

DC is the most common laboratory method with standardized procedures and is suitable for most kinds of cell lines. DC is also suitable for preparing a massive number of mitochondria. The disadvantage of DC is that the entire protocol takes about 1–2 h, and the centrifugation procedure could cause disruption to mitochondria. Therefore, the integrity of mitochondria must be checked carefully after isolation. Magnetic beads coated with antibodies have been used to isolate mitochondria in many reports. Horing-Do et al. [52] propose using microbeads conjugated with anti-TOM22 antibodies to achieve mitochondria isolation in a high-gradient magnetic field. The purity of mitochondria isolated in their protocol is comparable to mitochondria obtained using the ultracentrifuge method. However, this separation procedure takes approximately an hour from initial cell homogenization and the mitochondria cannot be released from magnetic beads, which may affect the mitochondrial

ultrastructure and cover epitopes on the mitochondrial outer membrane. To minimize the interference in subsequent mitochondria structural or functional studies, Liao et al. [53] apply the concept of using nickel ions to isolate recombinant proteins that are tagged with multiple histidine (His) residues to isolate highly purified mitochondria from yeast. The mitochondria concentrated from cells expressing Tom70–6xHis were incubated with Ni-NTA magnetic beads and then separated under magnetic fields. However, ultracentrifuge is required in their protocol and the incubation time of mitochondria with magnetic beads highly affects the isolation efficiency. Another example is from Bayraktar et al. [54] presenting MITO-Tag mice, which enable rapid isolation of mitochondria from specific cell types in vivo (3–5 min). Instead of using an endogenous outer membrane protein, they chose an epitope-tagged recombinant protein [55] to be the immunopurification handle because of the high sensitivity and specificity of various epitope tags and their cognate antibodies. By controlling the expression of Cre recombinase, they can restrict epitope tagging of mitochondria to a specific cell type and consequently immunoisolate mitochondria with cell-type specificity from a piece of tissue without the need for cell sorting.

On the other hand, the retrieved amount of the isolated mitochondria concentration using the inertial microfluidic method relies on (i) the concentration of lysate and (ii) the length of isolating time. Unlike the centrifugation method having a fixed isolation time, the inertial method is more suitable for a small amount of samples. For example, with this technique, 10 pg of mitochondria can be sorted out in 5 s with the inertial microfluidic method. This is approximately the number of mitochondria expected from a single cell. In Figure 1-5, the OCR data shows that the inertial microfluidic method can generate isolated mitochondria with integrity as good as the traditional method but faster when a small number of isolated mitochondria are required. In addition, we can always do batch processes to increase the yield and do not need a professional specialist to handle the process.

Mechanism	Yield	Duration	Pros	Cons
1. Differential centrifugation (DC)	7 ~ 50 μg per 10^6 cells. (Depends on cell types)	90-120 minutes.	✓ Cultured cells are standardized models and easily obtained. ✓ Mitochondria of higher purity can be prepared using a sucrose gradient.	✓ The integrity of mitochondria must be checked carefully after isolation. ✓ All the experiments that require intact mitochondria must be performed within 3 hours after isolation.
2. Antibody- coated Magnetic beads	~4 times more compare to ultracentrifugation method.	15 – 60 minutes of incubating mitochondria with antibody-coated magnetic beads.	✓ High purity of isolated mitochondria.	✓ Mitochondria cannot be released from magnetic beads. ✓ May affect mitochondrial ultrastructure and/or cover epitopes on the mitochondrial outer membrane.
3. Affinity purification using magnetic beads	100 μg of mitochondria from 1g of wet yeast.		✓ High purity of isolated mitochondria. ✓ Mitochondria are released from magnetic beads. ✓ Does not require large number of starting materials and ultracentrifugation.	✓ Not suited for large amounts of mitochondrial preparation. ✓ Centrifugation required. ✓ Incubation time highly affects the isolation efficiency.
4. MITO-Tag	N/A	3.5 min immunoprecipitation with anti-HA bead.	✓ Epitope-tagged recombinant protein increases sensitivity. ✓ Utility for assessing mitochondrial metabolism in vivo.	✓ Transfection of epitope-tagged constructs are required.
5. Inertial microfluidics (This proposal)	2 pg per second.	Depends on the number of mitochondria needed. (Seconds – Minutes)	✓ Simply injecting lysate through a microfluidic channel.	✓ Require small number of mitochondria. ✓ Continuous batch process. ✓ Simple equipment and no need of training.

Table 1-1 Comparison of mitochondria isolation between the centrifugation method and inertial microfluidic method proposed in this article.

1.3.4 Calculation of Reynolds number and Dean number

The Reynolds number (Re) is defined as the ratio of inertial force to viscous (or friction) force, and can be expressed as: $Re = \rho u D_h / \mu$, Where

Re = Reynolds Number (non-dimensional),

ρ = density (kg/m^3),

u = velocity based on the actual cross-sectional area of the duct or pipe (m/s),

μ = dynamic viscosity (Ns/m^2),

Dh = hydraulic diameter (m), which is 4A/P, where A is the cross-sectional area of the flow, and the P is the perimeter of the cross-section.

We use the water density 1000 kg/m^3 and the dynamic viscosity is 0.001 Ns/m^2

to do the calculation.

The flow rate (Q) is calculated by A * V', where A is the cross-section area and V' is the average velocity. Therefore, the average velocity is calculated as:

60 (μl/min) / 20000 (μm^2) = 5 * 1010 (μm^3/min)/ (2 * 104) (μm^2) = 2.5 * 106 μm/min = 0.05 m/s.

The hydraulic diameter is calculated by:

4 * (width * height)/(2 * width + 2 * height) = 4 * (100 um * 200 um)/ 600 um ~= 133 um.

Therefore, the Re is calculated as:

1000 (kg/m^3) * 0.05 (m/s) * 1.33 * 10^{-4} (m) / 0.001 (Ns/m2) ~= 6.65.

The Dean number (De) is calculated as:

Re * (Dh /2R)

Where R is the radius of curvature and we calculated it to be ~ 3 mm. Therefore, the De is calculated as = 6.65 * (133(μm)/(2 * 3000) (μm))$^{0.5}$ ~= 0.9 (order of 0.1)

1.3.5 Channel roughness

To determine the surface roughness of the walls, we took SEM images of the fabricated devices (Figure 1-6) and measured the roughness on the bottom of the channel using Dektak. Based on these images we estimate the wall surface roughness to be under 2 microns. Since this is much less than the channel width, we believe this does not significantly affect the separation efficiency.

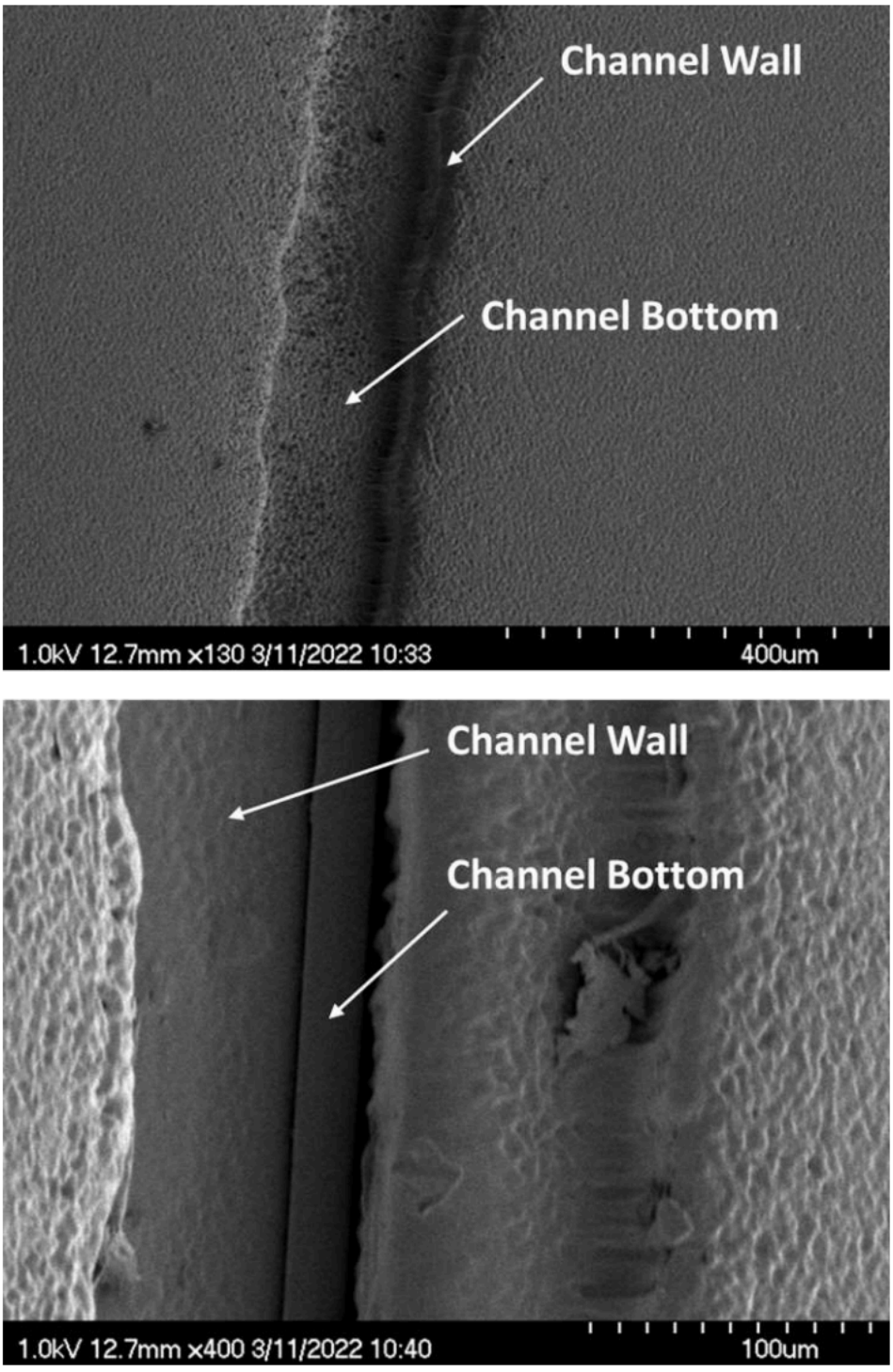

Figure 1-6. SEM image of microchannel sidewalls coated with 5 nm Iridium (a) curvature channel, (b) straight channel.

1.4 Conclusion

This work has shown for the first time the use of microfluidic centrifugation for the isolation of vital mitochondria. The RCR, the "industry standard" for the determination of the integrity

and quality of the isolated organelle, is as good as or better than traditional differential centrifugation. We anticipate that the availability of improved tools for studies of bioenergetics to the broader biological community will enable bioenergetics to be explored in more meaningful ways, leading to further understanding of the links between energy, health, and disease, for both research and clinical diagnosis of mitochondrial diseases. Now that we can isolate mitochondria from a small number of cells, it is within the realm of possibility to push this to the single-cell level with on-chip, single-cell lysing technology. Coupled with on-chip downstream sorting and analysis of the hundreds of mitochondria from a single cell, this could enable for the first-time technology to assay functional heteroplasmy of mitochondria at the single-cell level.

Chapter 2. NANOSTAT: AN OPEN-SOURCE, FULLY WIRELESS POTENTIALSTAT

2.1 Introduction

Electrochemcal techniques interface the world of electricity to the world of chemistry utilizing a mature, broad, and powerful suite of tools for quantitative analysis of composition of analytes for sensing and biomedical diagnostics. [56] These include DNA, RNA, proteins, aptamers, peptides lipids, metabolites, small molecules, trace metals, and even virions, such as the COVID19 virion. The simplest of the techniques require only resistance measurement whereas the most sophisticated techniques utilize signal processing and precise, coordinated timing of voltage and current waveforms (such as steps, pulses, etc. used in cyclic voltammetry, square wave voltammetry, chronoamperometry, and normal pulse voltammetry) with ultra low noise and ultra high gain analog circuitry to extract every possible piece of information about the analyte of interest.

While typical tools are benchtop standalone instruments costings thousands to tens of thousands of dollars, recent trends in the literature have used smaller and smaller custom boards with fewer and fewer components. [57] In the extreme, all signal processing and data storage in the cloud is handled off-board, with the potentiostat only doing the most low level work, the digitized signals immediately broadcast as unprocessed digitized voltages for could based processing on custom software on wired or wireless linked PCs or smartphones. This often is sold as “wearable” electronics, although the battery is still an issue, and an external processor with signal processing capability, memory, and storage capacity is required, typically referred to ambiguously as “the cloud”. The control machine is either a smartphone of PC. It is advertised as “the cloud” because the PC /smartphone is connected directly to the internet, but the electrochemical sensor is NOT. While this technology definitely has its place and advantages, this is a bit misleading, because all smartphones and PCs are internet connected these days, so to call the electrochemical sensor connected to a PC or smartphone “cloud connected” is almost a tautology.

Furthermore, this approach requires custom, often proprietary software specific to the operating system of the off-chip architecture (e.g. Windows, Linux, Android, iOS, etc.). The trend has been to use the lowest possible architecture on the sensing chip such as 8 bit Atmega or at best 32 bit ARM (STM32) microcontrollers, with minimal on board intelligence, memory for at most a few traces, no internet connectivity (only Bluetooth, which is peer to peer and requires custom software) and little to no ability to serve files or graphical representation of data.

Many or most such solutions are proprietary, expensive, and closed source. The only open source solutions (reviewed in detail later in this paper) require the user to source the parts and separately solder them manually or place them manually and reflow solder them in their own labs. Both of these are laborious and require special skills. Manual pick and place is prone to error as the size of the components gets smaller, limiting the miniaturization potential. The alternative approach presented in this paper is to employ automated pick and place machines that, unlike human hands, can handle extremely small surface mount (SMD) parts as well as employ automated reflow soldering, which is more economical and can be ordered and manufactured from vendors at low cost without the need for any manual

assembly at all. The boards come shipped to the user ready to operate “out of the box”. Finally, the CAD files are based on expensive, commercial, proprietary software that needs to be installed on a desktop PC for design changes.

In this work (Figure 2-1), we present a fully open source hardware and software design for a potentiostat (the “NanoStat” that 1) can serve all the results via a web page hosted on board the microcontroller itself 2) can be connected to from the internet from anywhere in the world via a web browser and 3) contains only 2 key integrated circuits (ICs) other than the voltage regulator, battery management, and USB ICs and a handful of discrete components: (a) a single microcontroller with on board WiFi, memory and signal processing with a complete file system and (b) a single chip analog front end. The entire system fits on a 20 x 40 mm board, with battery operation can run 6 h in active mode and even longer in sleep mode. As such, this is the world’s smallest web-server (WiFi) enabled potentiostat. The cost is ultra low, under 25 dollars in small quantities fully assembled with no soldering needed. The CAD designs are also provided on a free, web based CAD program accessible from anywhere in the world with only a web browser.

We anticipate that the application of this could be very large, from biomedical sensing in the clinic, to remote monitoring of unattended “motes”, to even possibly sensing aerial pathogens such as COVID in large public spaces without the need for anything other than a web browser for remote monitoring from anywhere in the world. Furthermore, any lab with a modest budget, including garage DIY, K-12 education, and modern university labs that need sophisticated electrochemical analysis with minimal investment of time and money, can benefit from this work. Finally, we propose to use this software suite as the kernel of a future open source, general purpose electrochemistry suite. Similar to how Linux is an open source operating system for modern PCs, abstracted from the hardware, we propose an open source project for electrochemistry, also abstracted from the hardware, and based on our initial foundational web-based work presented in this paper, which we call “OpenEChem”.

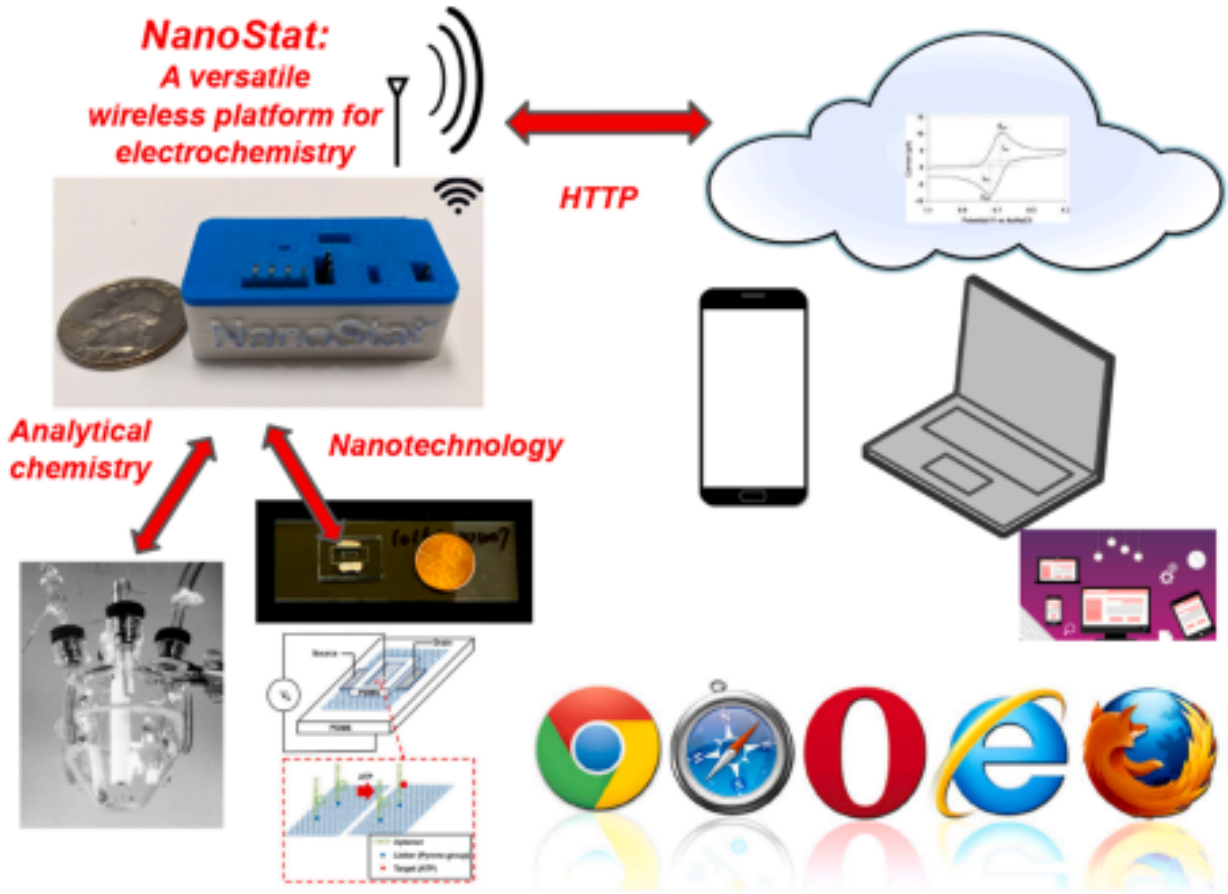

Figure 2-1. NanoStat: A versatile wireless platform for electrochemistry, from traditional analytical chemistry to advanced nanotechnology based sensors (e.g. Datta et al. [58]), using only a web browser for access to a broad suite of software defined analytical tools.

2.2 System design

In this section we describe the overall design. Both the hardware and software source code are available on as S.I. and on a GitHub repository as https://github.com/PeterJBurke/Nanostat.

2.2.1 Hardware architecture

The hardware architecture (Figure 2-2) is based on two core integrated circuits (ICs): The ESP32 (Espressif Systems) IC has integrated WiFi, 520 KiB SRAM, 8 bit DAC, 12 bit ADC, and dual core 32 bit processors operating at 240 MHz. We use the SOC version (ESP32-PICO-D4) which has integrated crystal oscillator and 4 MByte of integrated SPI flash memory. Note that this is the key enabling technology of this work, as it contains processing power and connectivity orders of magnitude improved over prior microcontroller based potentiostats. (See "Prior Art" discussion later in this paper).

The analog front end (AFE) is an Analog Devices LMP91000, which has an integrated analog potentiostat to enable bipolar (both sign) cell operation from a single sign power supply. A digital (I2C) bus between the LMP91000 and the ESP32 controls the internal gain settings

and other configurations of the potentiostat. Additional on board circuitry includes a chip for USB interface (which is not required if fully wireless operation is used), and a chip for battery power management to charge the battery from a USB connector, similar to a cell phone charger. An on board LED provides power status and a separate LED blinks every time a data point is taken. Figure 2-3 shows the circuit board rendered. The number of distinct components is 29; the total number of components is 42.

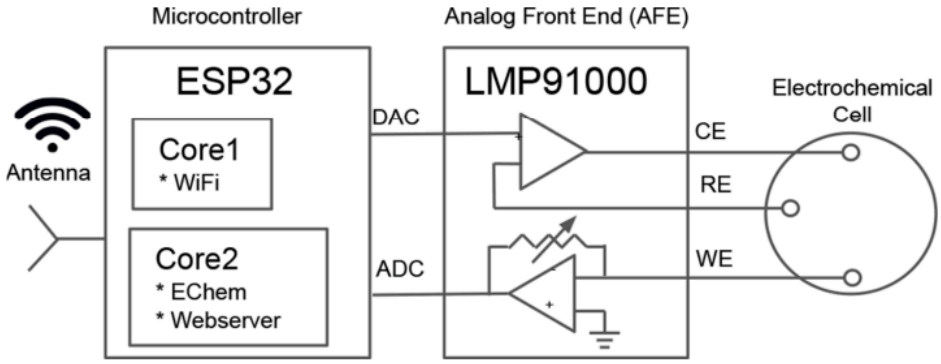

Figure 2-2. 2 chip architecture schematic. One of the chips provides memory, firmware, WiFi connectivity, and hosts the website and file system for the user interface and analysis. The other chip provides the analog front end (AFE).

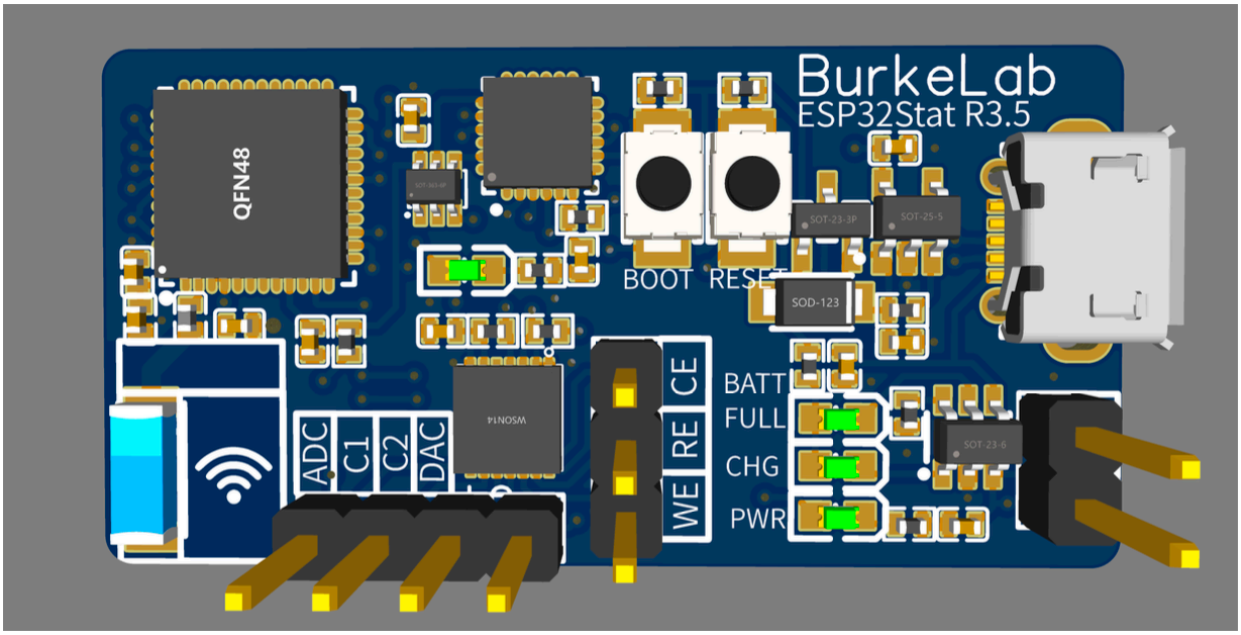

Figure 2-3. Circuit board rendering. Test ports are provided for access to the ADC, DAC, and C1/C2 which are either side of the TIA resistor. A USB connector is for the first firmware download and to charge the battery. LEDs indicate the battery charging status (charging or complete).

2.2.2 Hardware CAD

The CAD file is designed using a web based CAD program called EasyEDA (https://easyeda.com/editor). In addition to providing web functionality usable from anywhere in the world, it has an integrated library of parts that can be assembled by the

manufacturer, with real time information about stock status, something that is increasingly important in the modern chip shortage era. The CAD files, Gerber files, bill of materials, and pick and place instructions are provided in the online repository (https://github.com/PeterJBurke/Nanostat). These are sufficient for any user to have the board manufactured from their preferred vendor. In this project, the vendor JLCPCB (https://jlcpcb.com) was chosen due to their fast turnaround time (under 2 weeks from order to delivery), integrated supply chain with real time stock information for part availability, and low cost (under 25 dollars for a fully assembled board with all parts already soldered in place, including express international shipping). However, this project is suitable for any vendor, i.e. is vendor agnostic.

PC board: The PC board is FR4 with 0.5 oz. Cu traces, and is 4 layers (with ground plane and power plane the middle layers) to improve grounding, reduce V_{cc} bounce and improve shielding.

Case: Although not necessary for operation, the design for a 3d printed case is provided in the supplementary information files, both with and without battery.

Battery: A lithium polymer (LiPo) battery of arbitrary size (in x y and z dimensions) can be purchased for any application. For this system we recommend matching the x-y dimensions to the board size, and z can be 1 to several mm. For example, model 402,040 is 4 x 40 x 20 mm, costs only a few dollars and has 280 mAh of capacity, enough for over 6 h (Figure 2-4). Power through the USB is also possible using a larger battery (e.g. Voltaic Systems V25 6400 mAh USB Always On Battery), available for tens of dollars, with 6400 mAh capacity i.e. > 50 h of active running (Figure 2-5).

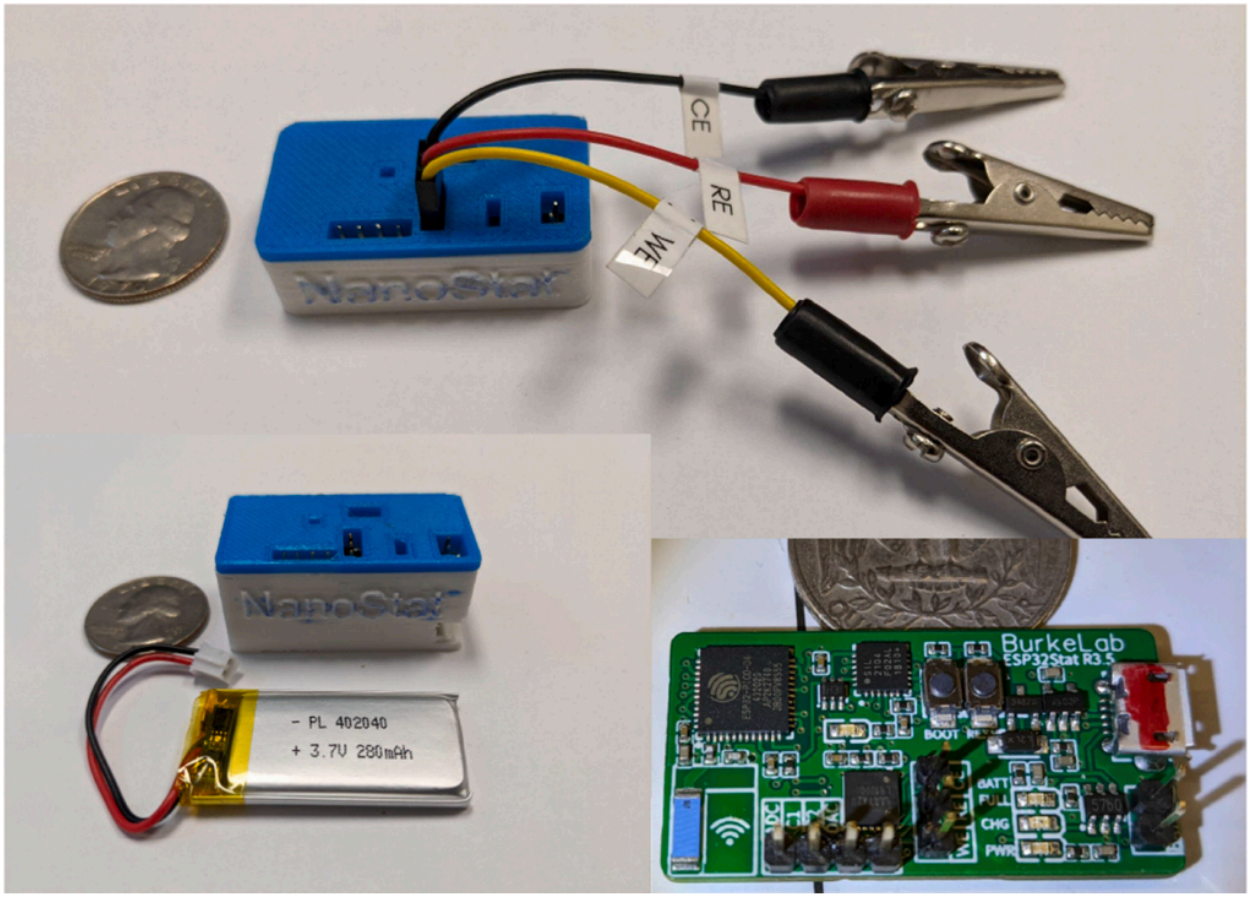

Figure 2-4. Photographs of the NanoStat. Alligator clips are shown but in principle any electrode connection technique can be used. (The circuit board connector is a standard 0.1" DuPont connector.) The bottom left inset shows the 3d printed case with the optional LiPo battery taken out of the case (4 × 40 × 20 mm, 280 mAh).

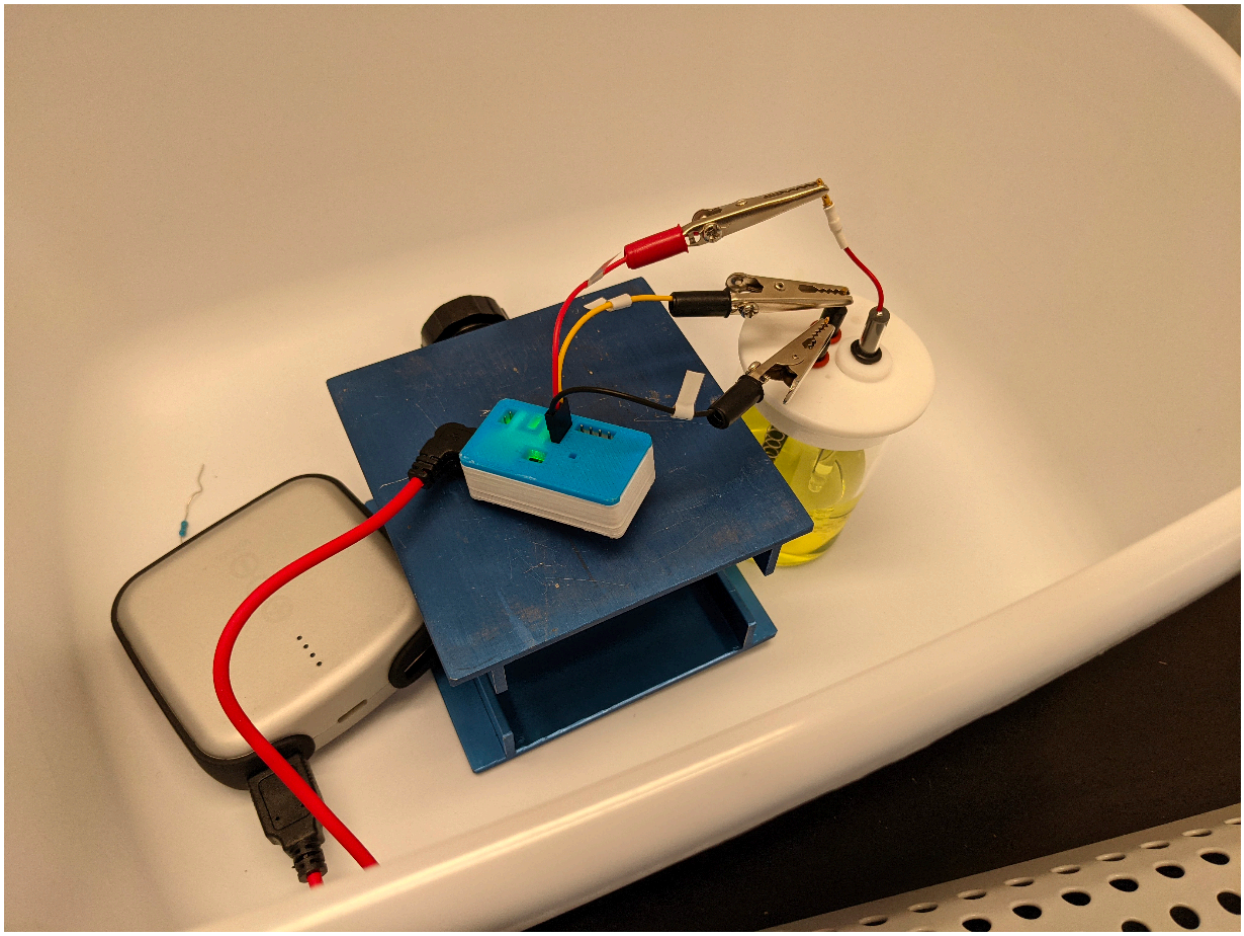

Figure 2-5. The NanoStat in action. An external USB connector battery , popular among cell phone users, (left) is used. The electrochemical cell is at right. The blue stand is for support only is is not required.

2.2.3 Software design

The software consists of the C++ code for running the microprocessor and the HTML5/JavaScript code for the web server/user interface (UI). Microsoft Visual Studio Code is used as the integrated development environment (IDE), with the PlatformIO add on, which is synced to the github repository (https://github.com/PeterJBurke/Nanostat) for easy development and web based deployment. The C++ code is about 4000 lines of code. The HTML5/JavaScript is about 1000 lines of code.

2.2.4 Firmware design

As usual in software development, we rely heavily on existing libraries integrated into this project. The following libraries were used: linneslab/LMP91000 version 1.0.0; me-no-dev/AsyncTCP version 1.1.1; ottowinter/ESPAsyncWebServer-esphome version 1.2.7; bblanchon/ArduinoJson version 6.17.3; links2004/WebSockets version 2.3.6; bbx10/DNSServer version 1.1.0. There is a well developed software library for the LMP91000, developed initially by github users icatcu (2014) and jorgenro1 (2015), and most recently in Hoilett et al. [59] In addition, there are several libraries for web hosting and file

transfer. Because the ESP32 runs FreeRTOS operating system under the hood, and because of its dual core CPU architecture, it is possible to have simultaneous WiFi connectivity and control of the potentiostat and electrochemistry. This has not previously been the case with any other wireless connected electrochemical system (see “Prior Art” section below).

The main issue with this architecture is the limited number of bits for the resolution, and the non-linearity of the ADC and DACs. For the limited number of bits, the AFE takes the analog “drive” signal and scales it by from 2 to 24 percent, so the effective bit resolution is much smaller at the cell. For 3.3 V power supply and 8 bits the resolution is 12 mV. But when divided down to 2 percent it is effectively 0.1 mV at the cell.

The non-linearity and offset of the ADCs is far from ideal (see SI). For this purpose, a calibration routine was developed. The user connects the RE/CE, floats the WE, and runs the calibration routine once. The firmware calculates the effect slope and offset, stores these in the on board flash memory, and calls on these in each subsequent run. (See SI for description of calibration technique).

2.2.5 Web design

HTML5, JavaScript, and CSS (Cascading Style Sheet) are used together with the Bootstrap framework and the Plottly graphing package for an intuitive, responsive, and mobile friendly user interface on both desktop and mobile browsers. The data is transferred over a WebSocket opened between the client and the server in binary form to the browser for display.

2.2.6 End-user perspective for electrochemistry

The following sweep types are supported in the present version: cyclic voltammetry, square wave voltammetry, chronoamperometry, and normal pulse voltammetry, current-voltage curves, “oscilloscope” mode with quantitative noise analysis (RMS, standard deviation), and a calibration mode. The user can enter various parameters for different types of sweeps, as well as simple IV curves, and noise tests (“oscilloscope mode”). The software displays “sweeping” on the browser and once the sweep is completed presents the data in a graphical format (Figure 2-6), which the user can change the scale on, zoom, etc. An ASCII text data file is auto-downloaded to the web browser’s disk at the end of each sweep.

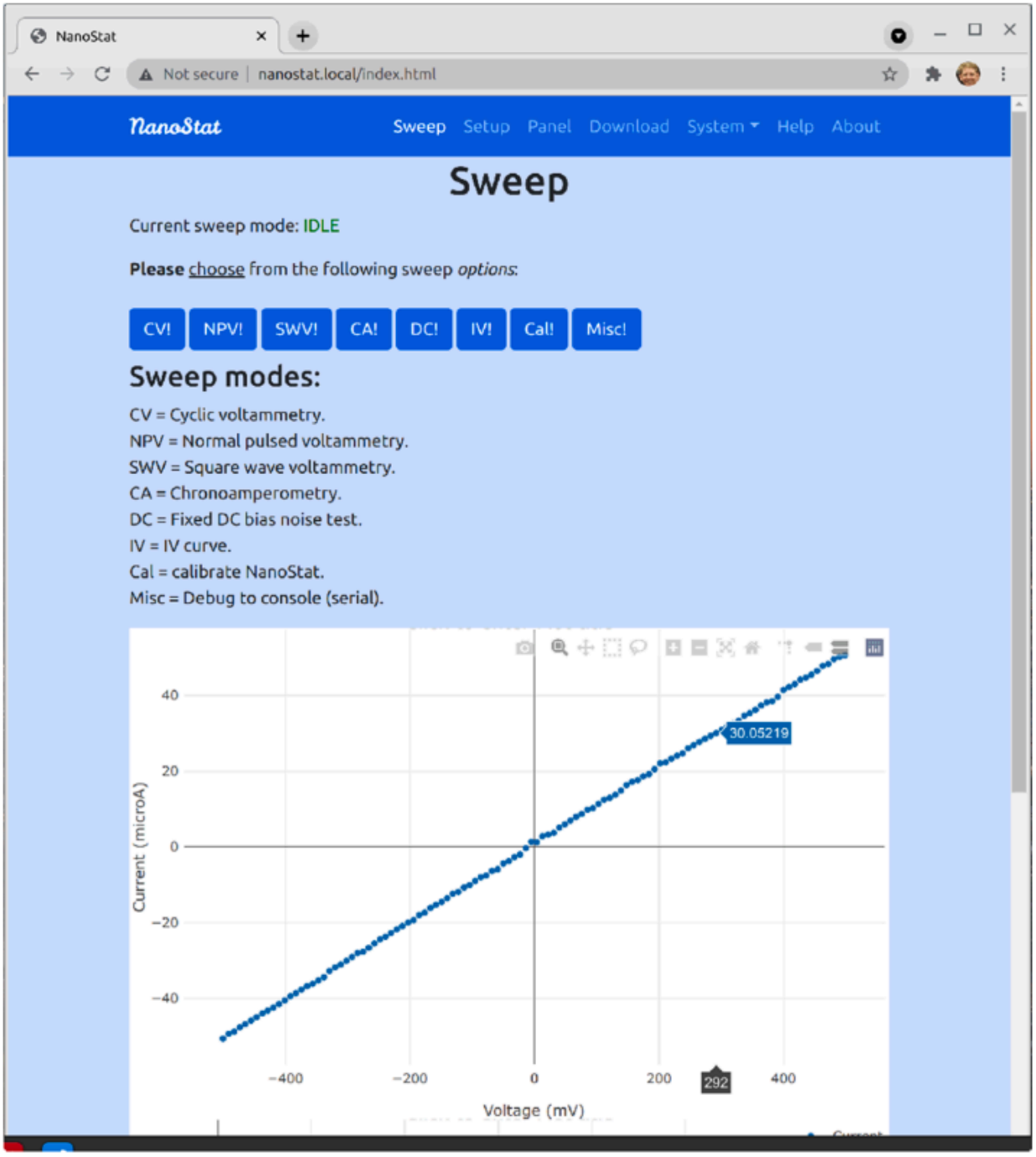

Figure 2-6. Graphical user interface (GUI) of one of the website pages. A test IV curve of a 10 kΩ resistor is shown immediately after measurement. The user can zoom, autoscale, read off each point, export the graph, and many other graphical options, as shown in the icons on top of the graph region.

2.2.7 System administration

If there is no WiFi connection, the device creates its own WiFi access point called "NanoStatAP". The user can connect to that access point and enter in the credentials of up to 3 WiFi SSIDs. The user can also perform over the air "OTA" firmware upgrades by uploading

the binary firmware, as well as list and delete files in the on board directory structure. Figure 2-7 shows the entire UI and menu tree/structure.

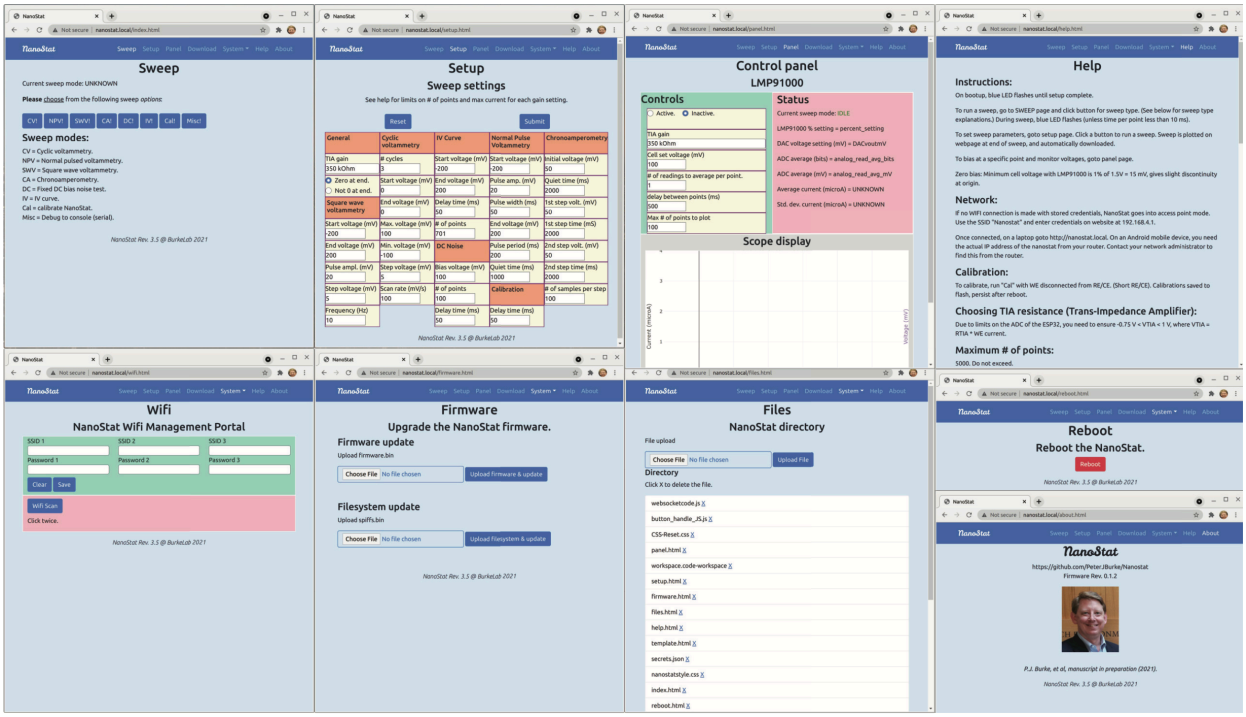

Figure 2-7. User interface in web browser. Note that no special software is needed to access and control the NanoStat. Only a web browser is needed; all the control and graphical plotting software is contained in the JavaScript and HTML5 code which are intimately synchronized with the on board firmware to control and record the analog signals and report them back to the website over WiFi using WebSocket technology.

2.2.8 Test chemicals

In order to compare the performance of the NanoStat to industry standard, we performed electrochemistry experiments using a Ag/AgCl (3M KCl) Reference Electrode (BASi MF-2056), a platinum wire auxiliary electrode (BASi MW-1033), and a 3.0 mm diameter gold working electrode (BASi MF-2114) in a standard 100 mL Standard glass electrochemical cell (BASi MF-1051). The redox active species used was 5 mM potassium ferricyanide in 100 mM KCl at room temperature. The same cell was measured in the same session with a high end Gamry potentiostat (Reference 600) for comparison.

2.3 Results and Discussion

2.3.1 Analytical electrochemistry

Figure 2-8 shows the results of the Gamry and NanoStat to measure cyclic voltammetry, square wave voltammetry, chronoamperometry, and normal pulse voltammetry. The parameters are the default parameters shown in the "Setup" page of Figure 2-7. The results agree extremely well, demonstrating this work is consistent with the most high end analytical chemistry instrumentation available on the market today.

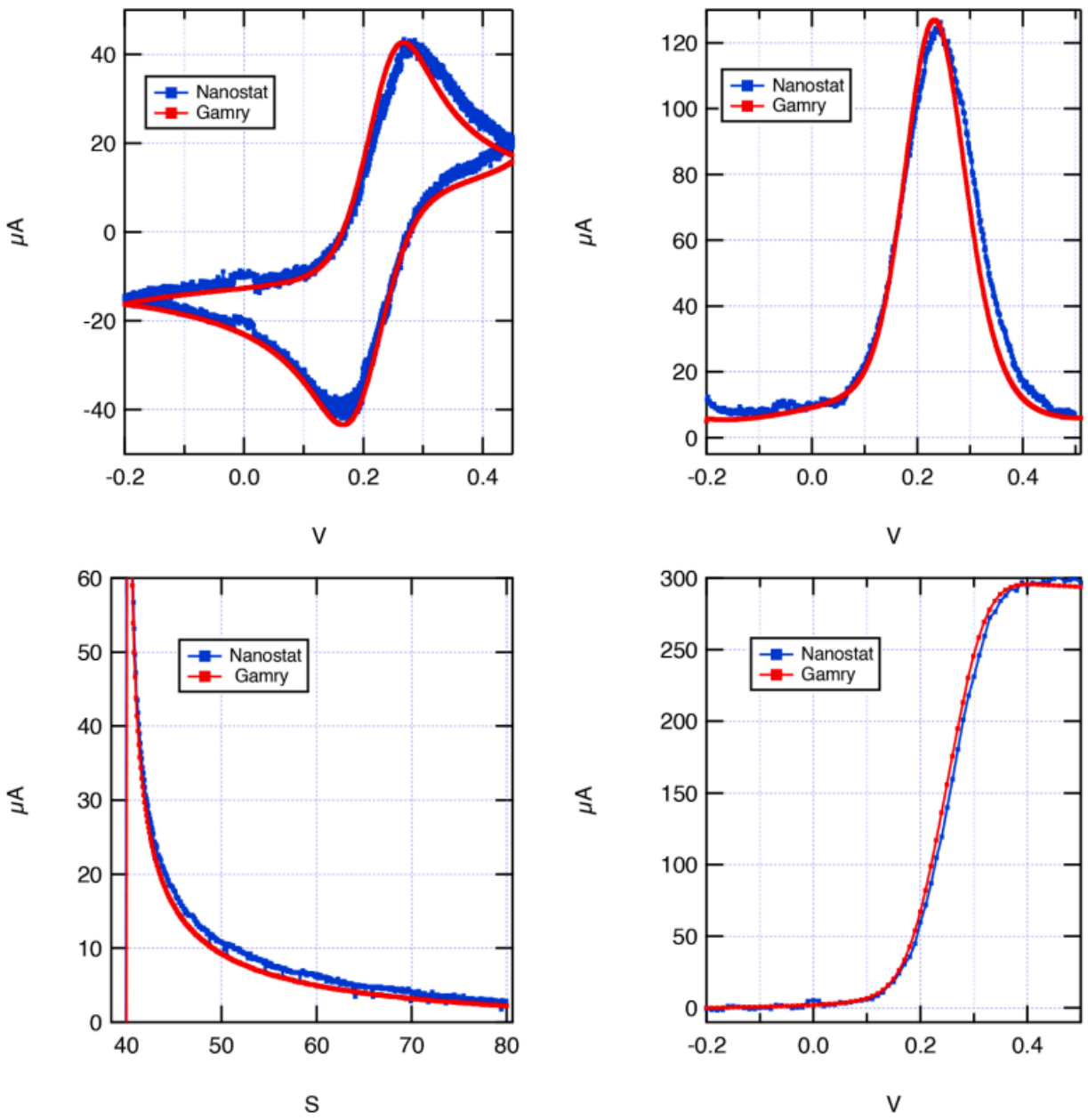

Figure 2-8. Cyclic voltammetry, square wave voltammetry, chronoamperometry, and normal pulse voltammetry measured with the NanoStat (blue) and a high end Gamry commercial potentiostat (red).

2.3.2 Noise

Given the simplicity of the system, the close proximity of digital, RF, and analog circuits on the board (and on the IC itself), and the lack of any on board analog or digital filtering, the noise performance is astounding. When operated with a battery, the system noise is determined by the bit resolution of the ADC. We explain.

For the trial data in Figure 2-8, the Gamry is using extensive on board analog and digital filtering, whereas the simple NanoStat measures only one ADC reading per data point with

no filtering. Each data measurement takes 160 μs. In the firmware, it is possible to average more readings if the rate is sufficiently slow.

In order to quantitatively test the noise, we use the “dc bias” sweep mode. In the “dc bias” sweep mode, the firmware sets the dc bias voltage to a user selectable value, then reads ADC with various number of readings per point 1, 5, 10, 50, 100, 500, 1000, at a user specified delay between points. In Figure 2-9, we plot the data points with and without the battery for a 100 kΩ test resistor biased at 100 mV. One data point is taken every 10 ms. With the PC USB power, there is clearly 60 Hz noise (red trace). With the battery power, this 60 Hz noise is gone. For no averaging (1 ADC reading per point, beginning), the error is about 1 bit in the current. This corresponds to 2 nA, since the ADC is 12 bits (full scale voltage = 3.3 V), and the TIA resistor is set to its most sensitive value the LMP91000 offers: 350 kΩ. Occasional spikes in the ADC reading are seen of a few bits, a known flaw of the ESP32 with unclear origin. The later data (with 1000 ADC readings per point, corresponding to 160 ms per reading) shows noise much lower then the single bit level. Thus, with no signal averaging, the noise is limited by the bit resolution of the ADC, under battery use, with no 60 Hz noise. With USB power from a PC, the 60 Hz noise is much was much worse and needed to be filtered out digitally to get to the bit resolution of the ADC. This shows that a battery powered, wireless potentiostat (without any USB connections to a PC) is a wise choice for low noise operation.

Due to limits on the ADC of the ESP32, one needs to ensure - 0.75 V < VTIA < 1 V, where VTIA = RTIA * WE current. For WE currents of 10 s of microamps, we typically therefore use 35 kΩ as the TIA resistance, which gives a noise of about 50 nA, as can be seen in Figure 2-8. The “oscilloscope” panel allows the user to plot the readings in real time on the web browswer for a given bias voltage and number of points to read. We confirmed that 50 nA is the RMS current noise with no averaging using a 35 kΩ TIA amplifier and a 10 kΩ test resistor.

For applications that need more than 12 bits of resolution on the WE current, other approaches with a separate ADC IC would be needed (see below, “Prior Art” section). For applications that need better than 2 nA of current sensitivity, it is possible with the NanoStat for a user to select an external TIA resistor and connect it to the PC board labeled C1/C2, for additional current sensitivity. This option is supported in the firmware; the user just needs to select “external resistor” in the dropdown menu of TIA gain on the “setup” page (Figure 2-7).

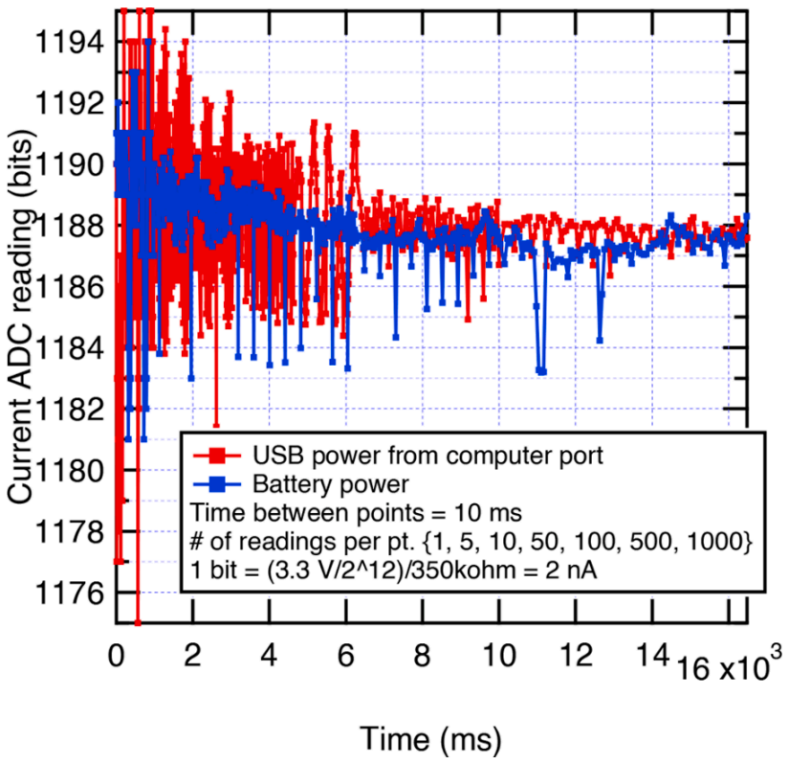

Figure 2-9. Current vs. time ADC reading (output of LMP91000 TIA) with 100 kΩ test resistor biased at 100 mV. One data point is taken every 10 ms. The data point is the ADC reading with various number of readings per point 1, 5, 10, 50, 100, 500, 1000. The 60 Hz noise is clearly visible in the red trace. With battery power only, the noise is limited by the bit resolution of the ADCs.

2.3.3 Prior Art

Whitesides has laid out the criteria for an analytical electrochemical system to be considered open source. [60] His criteria for open source are clear and reasonable: "Description of a truly open-source potentiostat should include all details required to replicate the system...." including circuit design, component list, board layout file, and software (microcontroller firmware and PC/tablet/smartphone control software). Many academic papers only partially meet this, meaning a lab new to the field or even an experienced lab cannot reproduce prior academic work due to lack of published details. In the old days of chemistry, if a reviewer was to accept a paper, it was required by the editor that the reviewer reproduce the results in his own lab. While this may no longer be economical, certainly publishing the details of the experimental process should be. [61]

As far as we can tell, the concept of a DIY, general purpose, open source potentiostat was pioneered by Kevin Plaxco's group at UCSB about 10 years ago [62] (the "CheapStat"). There, an open source (hardware and software) handheld potentiostat was described. The user is provided gerber files for a PC board to be manufactured, a list of components, and the user would solder the components (cost ~$80 in low volume) by hand to the PCB. The firmware and PC software for the USB control was provided. The AFE was a custom op amp and the microcontroller an Atmel XMEGA, an 8 bit microcontroller with 12 bit ADCs/DACs, 8 KB RAM and up to 128 kB flash. Voltage resolution was sub mV and current resolution sub nA.

Whitesides' group at Harvard followed on with a cell phone connected (via audio cable) potentiostat in 2014 [60] of cost (parts only) ~$25 in large volume (> 1000 pieces). There, they used an Atmega328 (Atmel) 8 bit microcontroller (popularized as an Arduino) with a wired interface to a cell phone through the audio jack, an external 16 bit ADCs/DACs, and an analog 4 pole low pass filter (LPF). Current resolution was 1 nA. The parts list was provided but the software and PC board Gerber files/CAD files were not provided, so it was not open source.

A high performance open source project with USB connection to a PC was published as "DStat" [63] in 2017. There, an ATXMEGA256A3U was used (an 8 bit microcontroller with 8 KB RAM and up to 128 kB flash), with custom AFE and 16 bit DAC IC and a 24 bit ADC IC. The AFE design was excellent: pA level currents could be measured. The user is provided the firmware, PC software, Gerber files for PCB manufacture, and a list of components to order. The user solders some components by hand and others with a flow solder technique after ordering the parts.

Dobbelaere [64] created a larger voltage version (up to 8 V) with PIC16F1459 (an 8 bit microcontroller), 22 bit IC for ADC/DAC, custom AFE, intended for battery research. All the details of the project (including the schematic, PCB design, last of components, microcontroller firmware, and host computer software) are made available to the user.

Whitesides' group in 2018 [65] published the first wireless (Bluetooth) open source potentiostat, which simply replaced the Atmega328 with the "RFDuino", and still used a custom AFE with separate 16 bit ADC and DAC ICs. RFDuino had an integrated BLE and Core0 Arm 32 bit processor. RFDuino, first marketed in 2013, is obsolete and almost impossible to source, and the company was acquired in 2016. A list of components to purchase as well as the PCB manufacturing files is provided (in addition to the firmware software and smartphone software), so the user can order the boards, parts, and manually solder the final system.

In 2018 Lopin [66] made a potentiostat with a SOC. It was not wireless. It used internal integrated op amps with higher noise and offset than discreet, but was still fully functional at the microamp level. It used on chip 12 bit ADCs/DACs.

In 2019, Jenkins et al developed the open source project "ABE-Stat". [67] This project provided both WiFi and Bluetooth wireless connectivity, as well as extended the analytical chemistry sweep methods to include electrochemical impedance spectroscopy (EIS), a valuable tool for capacitive rather than Faradaic current measurments. [68] A custom AFE was designed, and 24 bit ADC and 16 bit DAC ICs were used, as well as an IC for network analysis for EIS. Although a relatively powerful WiFi enabled microcontroller was part of the system (ESP8266), and external Bluetooth IC was used for communications with a custom Android app. As prior open source projects, a list of components to purchase as well as the PCB manufacturing files is provided (in addition to the firmware software and smartphone software), so the user can order the boards, parts, and manually solder the final system.

In 2020 Glasscott et al published the SweepStat. [69] The system used an Arduino Teensy with 16 bit integrated ADC and 12 bit integrated DAC, and a custom AFE. The interface to the PC is with USB and Labview software environment is used for the control. As prior open source

projects, a list of components to purchase as well as the PCB manufacturing files is provided (in addition to the firmware software and smartphone software), so the user can order the boards, parts, and manually solder the final system.

An AFE LMP91000 chip on an evaluation board (LMP91000EVM) and a BeagleBone microcontroller on a separate board were used to demonstrate a low-cost miniaturized potentiostat in 2014 by Bhansali. [70] Later, Hoilett [59] created a potentiostat

mm with an integrated AFE (LMP91000) run by an ARM based microcontroller (SAMD21, 256KB flash memory, 10 bit DAC, 12 bit ADC). It is open source, although not wireless. Their software and hardware are hosted on github and detailed assembly and operation instructions are provided. The parts and Gerber files are provided. Their recommendation is to have PCBWay manufacture and solder the components, which the user buys from DigiKey and ships to PCBWay. PCBWay allows Digikey sourced parts, they will source them for you and solder them in place. They also offer 2 side SMT, and connectors.

Mercer [71] developed a potentiostat with an ESP32 development board, used external 16 bit ADCs, and a custom op-amp AFE design. The entire system was demonstrated in a breadboard setting, not integrated onto a single PCB, and demonstrated the concept to use a microcontroller with integrated WiFi for potentiostat work. An electronically controlled (with servo) pump was also used.

An Ardruino board was used to control a custom home made AFE daughter board using discrete components and op-amps in ref. [72]

An open-source multi-channel potentiostat based on a Raspberry Pi with additional boards for each channel was demonstrated in ref. [73]

Additional related work that is not open source is given in refs. [74–80]

In addition to requiring high value skills (soldering tiny components) and being extremely inefficient, even for small numbers of boards, hand soldering has a significant limitation in the size of the board that can be made. Pick and place reflow soldering machines enable sub-mm accuracy in placement of parts whose size that far exceeds the ability of even the most trained human hand. Even compared to a technician manually soldering parts at minimum wage they also are more economical these days. And of course the reliability is much higher.

Many of the above projects require manual soldering, a custom AFE design with multiple AFE op amp chips and resistors, separate ADC and DAC chips, and typically separate wireless chips, if at all. In addition the memory and processing ability of almost all the microcontrollers used so far is not able to provide on board analysis, nor on board file systems or website hosting capabilities. Finally they are mostly manually soldered and require at least three institutions to make : 1) the parts source 2) The PCB manufacturer 3) the soldering (also many times manual, a severe disadvantage described above). We use an integrated provider that does all of 1–3 in house, as well as provides the (free) web based CAD with integrated supply chain real time stock information, with low cost and under 2 week turnaround time. Finally our work has a battery power and USB power to charge the battery, which many of the above open source projects do not have. Finally, none of the above

host a website on the potentiostat system and require the user to install custom software on a pc or smartphone.

2.3.4 Security

This version of the software uses HTTP, not HTTPs. For local area networks behind a firewall this is sufficient. However, for traffic over the public internet, it would be important to switch to enctryped traffic with the HTTPs protocol, and to enable a secure user login system.

2.3.5 Future miniaturization

We estimate the size of the circuit board and the number of components can be reduced by roughly a factor of two. First of all, the USB to UART interface was useful for developing the code (firmware, HTML5/JavaScript) for this project. However, now that we have demonstrated over the air (OTA) WiFi firmware update capability, the USB PC interface is superfluous and a simple UART interface (with off-chip FTDI to USB conversion) would save board space and components. Furthermore, the boot switches to put the microcontroller into firmware flash mode were found to be unnecessary with the IDE used in this work. These two changes could be easily implemented in future revisions of the board without any change in the software or functionality.

2.3.6 Power management

The ESP32 supports a sleep mode, and wake on LAN mode. These could be implemented to preserve power when the NanoStat was not actively taking measurements.

2.3.7 On board analysis

Due to the dual core 32 bit processors and generous onboard RAM, it is possible to incorporate just about any kind of signal processing and analysis a future user could design onto the microcontroller itself. In contrast to prior open source potentiostats (see below "Prior Art" section), therefore, this project is therefore very scalable to advanced signal processing and on board analysis.

2.3.8 Device performance (resolution, shielding)

Here we touch on how device performance (resolution, shielding) can be improved for future design. The ADC and DAC bit resolution are set by the microcontroller, so improvement here could use a separate ADC with more bits. The shielding could be improved by providing replacing the plastic 3d printed case with a metal case (Faraday cage), however the case design would need to allow WiFi antenna access to fields outside the cage.

2.3.9 Towards and open-source suite of electrochemistry software

Each of the above projects listed in prior art has custom software, but it all basically performs the same core function for control/acquisition (run a sweep of voltage vs. time, measure current vs time). The UI is also similar. Therefore, many these papers are "reinventing the wheel" to a large extent. For this reason, we propose a hardware abstracted, unifying suite of software we call "OpenEChem". With a common, unifying set of software, developers of advanced electrochemistry and sensing hardware can focus on the more challenging aspects

of the field, such as (for example) electrode functionalization, miniaturization, and application specific demonstrations.

Interestingly, the use of open source is also growing in the drone community. For example, we pioneered [81] and open source web based 4G connected drone technology using a cloud server to handle routing and encryption, and that is now adopted by the French drone company Anafi in the first 4G connected commercial drone in July, 2021. The drone community has also recently started adopting the ESP32 microcontroller and the advantages of the above manufacturing capability to have an open source, long range, cheap lightweight radio control link for drones (https://github.com/openLRSng) with hundreds of miles of range for receivers costing under ten dollars and weighing less than 1 g with on board antenna.

2.4 Conclusion

We presented an open-source, fully wireless potentiostat (the "NanoStat") for applications in electrochemistry, sensing, biomedical diagnostics, and nanotechnology, based on only 2 integrated circuit chips. This was demonstrated to have the same functionality as modern desktop-based potentiostats. While this particular project can be used by any lab or user on a very small budget, enabling numerous applications and use cases, it lays the groundwork for a more ambitious, web-based, open-source software suite as the kernel of a general purpose, hardware-abstracted electrochemistry software suite, which we propose as "OpenEChem".

Chapter 3. SUPER-RESOLUTION IMAGING OF VOLTAGES IN THE INTERIOR OF INDIVIDUAL, VITAL MITOCHONDRIA

3.1 Introduction

Analysis of mitochondrial structure and function is increasingly being recognized as central to understanding human health and disease. [3–6,11,82] Yet mitochondria within tissue cells can have markedly different structures and functions. Hence, there is a critical need to be able to characterize the structure and function of the individual isolated mitochondrion. One of the most important mitochondrial functions is the generation of cellular ATP by oxidative phosphorylation (OXPHOS). OXPHOS consists of the electron transport chain (ETC) plus the ATP synthase. The four multisubunit enzyme complexes of the mitochondrial inner membrane ETC (complexes I–IV) oxidize hydrogen derived from carbohydrates and fats with oxygen to generate H_2O. Starting with NADH for complex I or succinate for complex II, the electrons are transferred to coenzyme Q, then complex III, through cytochrome c to complex IV, and then on to oxygen. As the electrons transverse complex I, III, and IV, protons derived from H_2O (H+ + OH−) are transported out of the mitochondrial matrix to create an electrochemical gradient that is negative and alkali in the matrix and positive and acidic on the opposite side of the inner membrane. Thus, the electrochemical gradient ΔP consists of a membrane potential (ΔΨm), also called voltage, and a pH gradient (ΔμH+) with the pH gradient typically less significant: $\Delta P = \Delta\Psi m + \Delta\mu H+$. The mitochondria maintain a membrane electrochemical potential of about 150 mV. [7] This electrochemical gradient (ΔP) is a source of potential energy for multiple mitochondrial functions, the most important being the driving of the ATP synthase (complex V) to condense ADP + Pi to generate ATP.

Respiration of isolated mitochondria is commonly studied by the sequential addition of substrates and specific respiratory complex inhibitors. NADH-linked substrates such as pyruvate and glutamate feed electrons through complex I while succinate feeds electrons into complex II. The addition of these substrates results in electron transport, increased ΔP, and oxygen consumption known as state II respiration. The addition of ADP activates complex V to deplete ΔP and increase the rate of oxygen consumption known as state III respiration. Depletion of the ADP returns the respiration to the pre-ADP state known as state IV respiration. The addition of a compound such as carbonyl cyanide m-chlorophenylhydrazon (CCCP) depletes the electrochemical gradient resulting in maximal "uncoupled" respiration. The different steps of OXPHOS can be blocked using specific OXPHOS complex inhibitors including rotenone for complex I, antimycin A for complex III, and oligomycin for complex V.

The mitochondrial inner membrane is highly in-folded into double membrane structures known as cristae. These cristae are closed at the intersection with the intermembrane space between the inner and outer mitochondrial membrane to create closed cristae lumens. [39] The ETC pumps the protons into the cristae lumens on which the ATP synthases are bound. [83,84] Cleavage of Optic atrophy-1 (OPA1), which is located at the site where the cristae lumen is closed, releases the protons and disrupts the coupling between the ETC and ATP synthase. [39] The mitochondrial system is important for multiple other mitochondrial functions including mitochondrial membrane dynamics, thermogenesis, Ca2+ homeostasis, redox signaling, and apoptosis. [85,86]

Mitochondria ultrastructure has been extensively characterized with transmission electron microscopy (TEM) and CryoTEM in fixed cells. [87–92] However, only by imaging functional, intact mitochondria can one ascertain information about the electrophysiology of the organelle. Because the cristae are about 100 nm wide, they cannot be studied with diffraction-limited microscopy. Recently, this limitation is being addressed using super-resolution microscopy.

Super-resolution optical microscopy of fixed cells has been deployed extensively to study cristae structure and membrane protein distributions along the membrane. [93] But to understand the physiology of individual mitochondria, super-resolution of functional, intact mitochondria is required. Recent studies have employed super-resolution microscopy on mitochondria in live cells. [94–97] To put this work into proper context, all but one of the previous works has been on structure, not function (i.e., voltage). Although they are intimately linked, function is much more important (and difficult to measure) because, after all, life is function, not structure. Only one of these papers studied mitochondrial electrophysiology (function) using a membrane sensitive lipophilic cationic dye, and they completely misinterpreted the relationship between the dye fluorescence and membrane voltage, and did not perform the battery of metabolic manipulations possible with isolated mitochondria, as they used whole cells. A lipophilic cationic dye diffuses freely from one side of a membrane to the other, since the hydrophobic side groups give it good solubility in the interior of the lipid bilayer. No channel or energy consumption or redemption is required to allow passage of the dye. At low concentrations, the charge does not affect the membrane voltage, and the dye accumulates on one side or the other because thermodynamics says the probability of a particle being in a given state is proportional to e^−(energy/kT) of that state. Therefore, the ratio of dye concentrations is given by the Nernst equation, discussed in more detail below. However, many previous studies incorrectly assumed all the dye was free, neglecting the membrane binding of the dye, which has long been known to be the most significant component of the total dye fluorescence. [98] For example, our studies in 2010 [99,100] on isolated mitochondria using tetraphenyl phosphonium lipophilic cation (TPP+), detected electronically (rather than optically as in this study), used a calibration routine to convert to membrane potential that assumed (based on work by Kamo [101] others) that the total amount of TPP+ on the matrix side was approximately 90% bound to the inner membrane, and 10% free. Other groups later [102] used the same procedure, which lumped the membrane binding into an "activity coefficient" that combined free and membrane bound dye since they could not (until now) be resolved at that time. We [37] and others (e.g., [103]) that previously used diffraction-limited microscopy to image voltage dye concentration (Tetramethylrhodamine, Ethyl Ester, TMRE) were not able to resolve the cristae and therefore did not have any images showing membrane localization.

To characterize differences in the physiology of individual mitochondria from cells, we report here procedures for characterizing the mitochondrial structure and function of isolated, functional mitochondria using super-resolution microscopy. This revealed that we can use super-resolution quantification of mitochondrial membrane potential using lipophilic cationic dye fluorescence to characterize the respiratory function of individual isolated, functional mitochondria in a way not possible in whole cells, potentially permitting elucidation of differences between individual mitochondria. Finally, by careful analysis of

structure dyes and voltage dyes (lipophilic cations), we demonstrate that most of the fluorescent signal seen from voltage dyes is due to membrane bound dyes, and develop a model for the membrane potential dependence of the fluorescence contrast for the case of super-resolution imaging, and how it relates to membrane potential. This quantitative voltage-dependent membrane binding model explains why super-resolution images of lipophilic cationic dyes show strong intensity near the cristae and not in the matrix. This model enables quantitative imaging of super-resolution voltages inside functional, intact mitochondria with super-resolution.

Logical Structure of the Paper

This paper is organized into three major sections. In the first section, we develop and validate a quantitative model to demonstrate voltage imaging with super-resolution microscopy. In the second major section, we apply this to mitochondria in different metabolic states. In the third section, we discuss the need for biophysical models of mitochondrial function based on the Poisson statistics that results from the # of hydrogen ions in the cristae.

In the first section, we demonstrate that vital, isolated mitochondria voltages and ultrastructure can be imaged with super-resolution microscopy. Next, we demonstrate that the voltage dye is not free in the mitochondrial matrix but rather bound to the membranes, albeit in a voltage dependent manner. This finding contradicts prior, incorrect interpretations in some of the literature assuming that the dye is free and unbound, and requires a model to interpret the voltage imaging since the old model is wrong. Next, we develop and apply a model originally developed for diffraction limited micrsocopy (where the entire organelle appeared as one voxel, and the imaging technology could not localize the voltage dye within the organelle), and use this to quantitatively interpret and explain the voltage images we obtained. This model completely and consistently takes into account membrane binding. Next, in order to test our proposed model to more conditions, we use the model to make predictions about what would be observed in the absence of a membrane potential (e.g., created by CCCP) and to predict the fluorescence intensity inside the matrix of the small amount of free (unbound) voltage dye. These are unusual conditions which researchers usually do not investigate in detail. Sure enough, our measurements in these unusual conditions completely confirm the predictions of our voltage dependent membrane binding model. With this comprehensive, quantitative, experimentally validated model, we have provided the foundation for all future studies on the voltage distribution in mitochondria measured with super-resolution microscopy.

In our studies, we used all 3 modern methods of super-resolution microscopy: Airy, STED, and Lattice SIM (Structured Illumination Microscopy). While it is possible in some methods to observe clearly the outline of internal structure of mitochondria such as individual cristae, with voltage imaging, the resolution (of order 90 nm) is only able to observe cristae if they are separated, but cannot observe individual cristae in cristae dense mitochondria. We discuss this quantitatively in this section and demonstrate how the density of cristae, their voltage distribution, and the response to pharmacological manipulation of different metabolic states can be observed, even if individual cristae are not resolved.

The second major part of this paper aims to apply this model to mitochondria in different metabolic states, something not possible in whole cells. This demonstrates super-resolution voltage imaging in mitochondria in different metabolic states. These findings both reproduce all of the classical biochemistry metabolic studies of mitochondria, as well as demonstrate changes in the spatial distribution of the voltages as a function of metabolic state.

In the third section, based on our observed experimental data in the first two sections, we model the proton distribution inside the cristae semiquantitatively based on the membrane potential, capacitance, and pH. We demonstrate that bulk models of pH need to be replaced by refined models of electrophysiology at the nanoscale in mitochondria.

3.2 Materials and Methods

3.2.1 Cell Culture and Fluorescent Dye Staining

The MB231 cells and HeLa cells used in this research were purchased from ATCC. The HEK293 cells and HK2 cells were gifts from a collaborator. All the cells were cultured for 2–3 days in 75 cm2 tissue flasks at 37 °C and 5% CO_2 before being ready for experimentation. Dyes (10 nM TMRE or 100 nM MitoTracker DeepRed (MTDR) and 100 nM MitoTracker Green (MTG) or 100 nM 10-N-nonyl acridine orange (NAO) or 3 µL/ml PicoGreen; Santa Cruz Biotechnology) were added to the cell culture media and incubated 1 h prior the cell retrieval.

3.2.2 Mitochondrial Isolation

After retrieval, the cells were transferred into a falcon tube with 1 mL of ice-cold RBS buffer (5 mM KCl, 1 mM $MgCl_2$, 20 mM HEPES (pH 7.0)) added, and the tube was then incubated on ice for 10 min. After incubation, the solution was transferred into a glass homogenizer, and we performed 20 strong strokes separately using a loose and tight stroker. After the douncing procedure, 1 mL of homogenization buffer (450 mM Mannitol, 150 mM Sucrose, 1 mM EGTA, 40 mM HEPES, 1% (w/v) fatty-acid free BSA, 2% protease inhibitor) was added to the solution. Next, we centrifuged the homogenate at 1000g for 5 min at 4 °C to remove large-scale debris. The supernatant was recentrifuged at 12000g for 20 min at 4 °C to get purified isolated mitochondria. The pellet was collected and resuspended in 37 °C KCl buffer (140 mM KCl, 2 mM MgCl2, 10 mM NaCl, 0.5 mM EGTA, 0.5 mM KH2PO4, 2 mM HEPES) (pH 7.2).

3.2.3 Live Isolated Mitochondria Imaging

The collected isolated mitochondria were resuspended in 37 °C KCl buffer and plated in CELLview 4-compartment glass-bottom tissue culture dishes (Greiner Bio-One, 627870), PS, 35/10 mm. A 1500g, 8 min centrifugation step was applied prior to isolated mitochondria imaging to spin down the isolated mitochondria to the bottom of the dish. To improve the attachment of isolated mitochondria, the dishes were coated with Poly-l-lysine (0.1 mg/mL) for 10 min. Later, we removed the solvent and put the cartridge in a fume hood for 20 min to dry up before use. Prior to image analysis, raw .czi files were automatically processed into deconvoluted Airyscan images using the Zen software.

3.2.4 Protocols for Visualization of Mitochondria Structure Using Airyscan and STED Microscopy

For Airyscan: We used a Zeiss LSM900 (w/incubation chamber, set to 37 °C) with Airyscan with an alpha Plan-Apochromat 63×/1.4 Oil DIC M27 objective. We adjusted the laser power between approximately 0.3% to 2%, and the master gain between 750 and 900. We started continuous scanning at maximum speed at a zoom factor of 1, in order to obtain a relatively strong signal-to-noise ratio for imaging. Later, we brought the field of mitochondria of interest into view and stopped scanning. We selected a mitochondrion of interest and used the crop function to zoom in approximately 6.0× to 10.0× until getting clear images of cristae structures. The pixel dwell time was set between 0.85 and 1.04 μs, respectively to avoid overtime exposure of mitochondria to the laser. Note that to get clear enough isolated mitochondria images, we set the frame time to no longer than 400 ms to avoid blurring due to the movement of mitochondria. NAO and MTG were used for structural imaging (labeling the lipid bilayer), and TMRE was used for voltage imaging, as explained in the main text.

For STED: We used an Abberior Stedycon (w/incubation chamber, set to 37 °C), gracefully on loan for a demonstration from Abberior. After obtaining a relatively strong signal-to-noise ratio at a zoom factor of 1, we brought a single mitochondrion into view and stopped scanning. We used the crop function to zoom in on the image to the desired size. We used the autoadjust function to find the best pixel size and pixel dwell time for the observation. The best pixel size and pixel dwell time in our experiment were 25 nm and 10 μs, respectively. MTDR was used for structural imaging (labeling the lipid bilayer), and TMRE was used for voltage imaging, as explained in the main text.

3.2.5 Respiration State Experiment

Isolated mitochondria from HeLa cells were incubated in warm KCL buffer (140 mM KCl, 2 mM MgCl2, 10 mM NaCl, 0.5 mM EGTA, 0.5 mM KH2PO4, 2 mM HEPES) with a temperature control setting to 37 °C once isolated from HeLa cells (State 1). The concentration of isolated mitochondria was measured by using the Bradford assay. The time-step for each image was 5 s to avoid photobleaching. The 2.5 mM Succinate was used as the substrate to trigger electron transfer (State 2) and 250 μM ADP was added later to initiate the ADP-stimulated respiration (State 3).

3.2.6 Image Analysis

Processed Airyscan images were analyzed using ImageJ (Fiji) software. For all images performed in this draft, we only adjust the brightness and contrast to demonstrate relevant changes in structure. Images acquired with STED microscopy were deconvoluted using Huygens deconvolution software. Additional image analysis is described in detail in SI section 7.

3.3 Results and Discussion

3.3.1 Vital isolated mitochondria cristae structures and super-resolution electrical voltages can be resolved by super-resolution microscopy

The ultrastructure of the organelle can be imaged using membrane binding dyes such as Nonyl Acridine Orange (NAO), mitotracker green (MTG), mitotracker red (MTR), mitotracker deep red (MTDR), etc. In this work, we utilize these dyes to image the location of the membrane cristae within the limits of the resolution of the imaging system. (Although these dyes show some dependence on membrane potential, [104] we only use Tetramethylrhodamine, Ethyl Ester (TMRE) for voltage imaging, as it is more studied, and better understood.) This is shown in Figure 3-1, where we have used super-resolution microscopy (Airyscan) with NAO to image the ultrastructure of a single mitochondrion isolated from a human cell line (Methods).

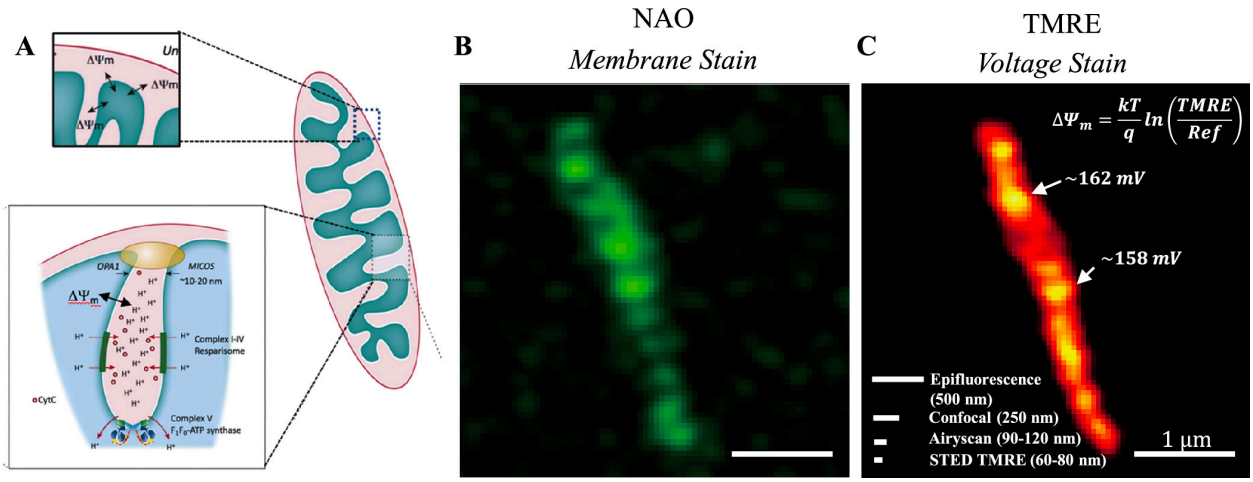

Figure 3-1. Model and images of isolated mitochondria. (a) Model of mitochondrial membrane voltage. [84] *(b) Isolated mitochondria stained with membrane fluorescent dye, NAO (c) Isolated mitochondria stained with voltage-dependent dye, TMRE. A simple application of the Nernst equation. Scale bars show the resolution of various imaging technologies for the TMRE dye. Reprinted from Trends Cancer, 3 (12), Burke, P. J. Mitochondria, Bioenergetics and Apoptosis in Cancer, Pages 857–870. Copyright (2017). with permission from Elsevier.*

In order to quantitatively assay membrane potential, a lipophilic cationic dye is traditionally used. As the dye has lipophilic moieties, it is soluble in the hydrophobic interior of the lipid bilayer membrane, and can readily diffuse from one side to the other. Since it is charged, its location inside vs outside the mitochondria is dependent on the membrane potential ΔΨm. Motivated by the apparent success of this approach in previous literature, [7,105,106] we seek to attain additional information about the spatial dependence of ΔΨm within the organelle. In Figure 3-1C, we show the fluorescence intensity of the lipophilic cationic dye TMRE in an isolated mitochondrion. The cristae harboring the ETC transported protons are clearly giving rise to a nonuniform distribution of TMRE, and hence a very nonuniform voltage ΔΨm, along the organelle. Also shown in Figure 3-1C are scale bars indicating the spatial resolution of various imaging technologies. Thus, using the Airyscan microscope, we have succeeded in imaging the membrane potential of vital, isolated mitochondria.

How does one interpret these images in terms of the actual membrane potential/voltage and the TMRE dye? If one neglects binding to the membrane itself (discussed below), the difference in densities across the membrane would be governed by the Nernst equation:

$$ni/no=e^{(-q\Delta\Psi m/kBT)}$$

where $\Delta\Psi m$ is the membrane voltage, and ni, no are the lipophilic cationic dye concentrations inside and outside the mitochondria (respectively), indirectly measured via the fluorescence intensity. A simplified application of the Nernst equation, using the background fluorescence (no), indicates varying voltages ($\Delta\Psi m$) along the mitochondria, near where the cristae are, indicating "high" voltages near the cristae. In addition, large dark regions seem to indicate low voltages in the mitochondrial matrix.

However, this interpretation (presented in, e.g., refs [94,107]) is not correct, as it ignores membrane bound TMRE. For example in ref [94], it assumes free (unbound, diffusible) TMRE in "compartments" of mitochondria was being resolved, and neglected binding to the membrane, which has long been known to be a significant factor. [98] This is understandable because (1) many references (even recent ones [94,107]) present the false picture that most of the TMRE are free on both sides of the membrane and neglect membrane binding, and (2) to date (until the advent of super-resolution microscopy), imaging the membrane bound TMRE has not been possible.

3.3.2 Most of the voltage sensitive cationic lipophilic dye TMRE is membrane bound, not free

Our Airyscan images reveal that the TMRE fluorescence correlates with the distribution of the mitochondrial cristae, as detected by the cardiolipin binding dye NAO. This is confirmed by plotting a line scan of the intensity along the length of individual vital mitochondria showing the overlap between the TMRE and NAO fluorescence levels (Figure 3-2B and Figure 3-2C). We observe this in both whole cells (reproducing ref [94], which found the same without explanation), as well as isolated mitochondria. Given that the mitochondrial inner membrane thickness is 4 nm and in tightly coupled mitochondria the in-folded membranes are tightly juxtaposed with a separation between 20 and 100 nm, we can estimate that a cristae finger would have a width of approximately 30 to 110 nm which is within the spatial resolution of the Airyscan microscope of 90–120 nm. Hence, this places the positively charged lipophilic dye in close proximity to the positive electromagnetic field of the cristae, an anomaly observed but not explained in a previous Airyscan study of mitochondria within the living cell. [94]

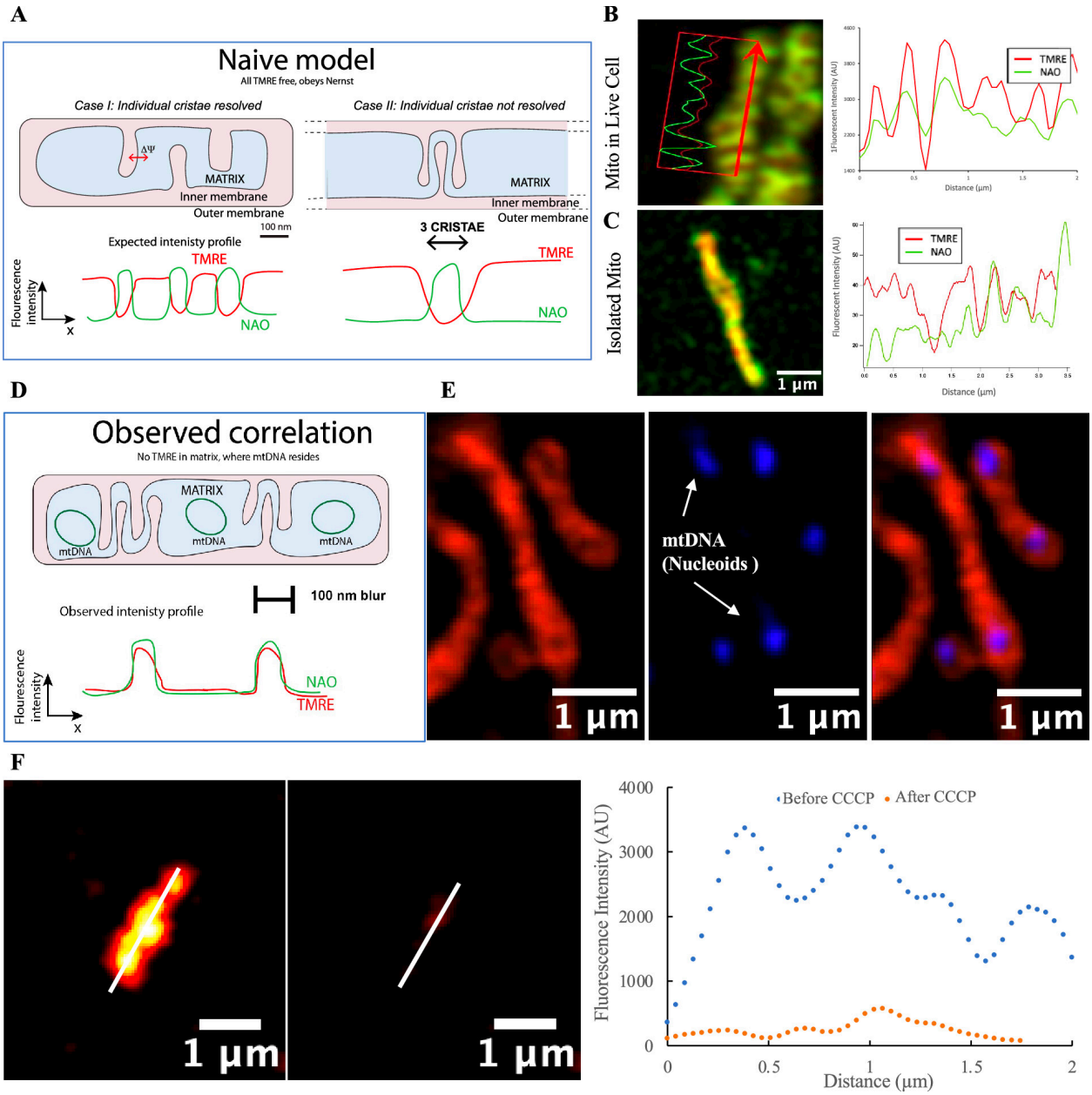

Figure 3-2. Correlation of TMRE and NAO. (A) Naïve model of TMRE uptake, neglecting membrane binding. If TMRE only exists as free molecules in the matrix, responding to the membrane potential ΔΨm according to the Nernst equation (eq 1), then the TMRE intensity should be anticorrelated with the membrane dye NAO, in contradiction to what we observed. Line profile of (B) mitochondria in a HeLa cell and (C) isolated mitochondria, stained with TMRE and NAO. The voltage sensitive cationic dye TMRE is localized at the cristae membrane, as demonstrated by the correlation between the TMRE and NAO intensity peaks, in contradiction to the naïve model for free TMRE. (D, E) Summary of experimental observations of TMRE localization in mitochondria. mtDNA was shown to be in the dark regions through PicoGreen staining in a separate experiment. (F) Line profile of isolated mitochondria TMRE image before and after treating with 10 μM CCCP.

To further confirm that the TMRE is not evenly distributed within the mitochondrial matrix, we stained the isolated mitochondria with PicoGreen which stains mitochondrial nucleoids green. Mitochondrial nucleoids are located in the mitochondrial matrix (Figure 3-2D), and the staining of isolated mitochondria with TMRE and PicoGreen confirmed that the TMRE

fluorescence does not correlate with the position of the mtDNA nucleoids and thus does not occupy the mitochondrial matrix (Figure 3-2E).

The explanation for this observation is that the TMRE is bound to the membrane, something which has been known with indirect studies for a long time. [98] Here, voltage-dependent membrane bound lipophilic cationic dyes are being imaged in vital, isolated, intact, functional mitochondria, clearly and directly confirming via super-resolution microscopy that most of the TMRE are bound to the membrane, something that was only possible to determine via indirect methods previously.

3.3.3 Binding of the TMRE Dye to the Membrane Model

In order to properly interpret the images of the TMRE intensity related to the membrane potential, it is critical to include the bound TMRE in consideration. To do this, we use a model proposed by Rottenberg in 1984, [108] and shown in Figure 3-3A. Rottenberg [108] proposed this in the context of mitochondria, but this model has not been used to interpret super-resolution images until this work: "The accumulation of these cations by mitochondria is described by an uptake and binding to the matrix face of the inner membrane in addition to the binding to the cytosolic face of the inner membrane." Rottenberg used radiolabeled lipophilic cations (triphenylmethylphosphonium (TMTP+), tetraphenylarsonium (TPA+), and tetraphenylphosphonium (TPP+)) to determine the concentration in the buffer, and therefore no imaging was used. Kamo and Demura [101] used this model and detected TPP+ in the buffer with electrochemical sensors; again no imaging was used: "The membrane potential-dependent binding was analyzed with a model: the membrane is split into two halves, outer and inner half, and the amounts of bound probes in each region are governed by the concentration in the contiguous solution." Follow on work by Scaduto [98] used TMRE and imaging, but not super-resolution imaging. We used diffraction-limited imaging also in mitochondria contained in nanofluidic chambers. [37] In this work, we extend the use of this model to interpret voltage images using super-resolution imaging in functional, intact, isolated mitochondria and live cells.

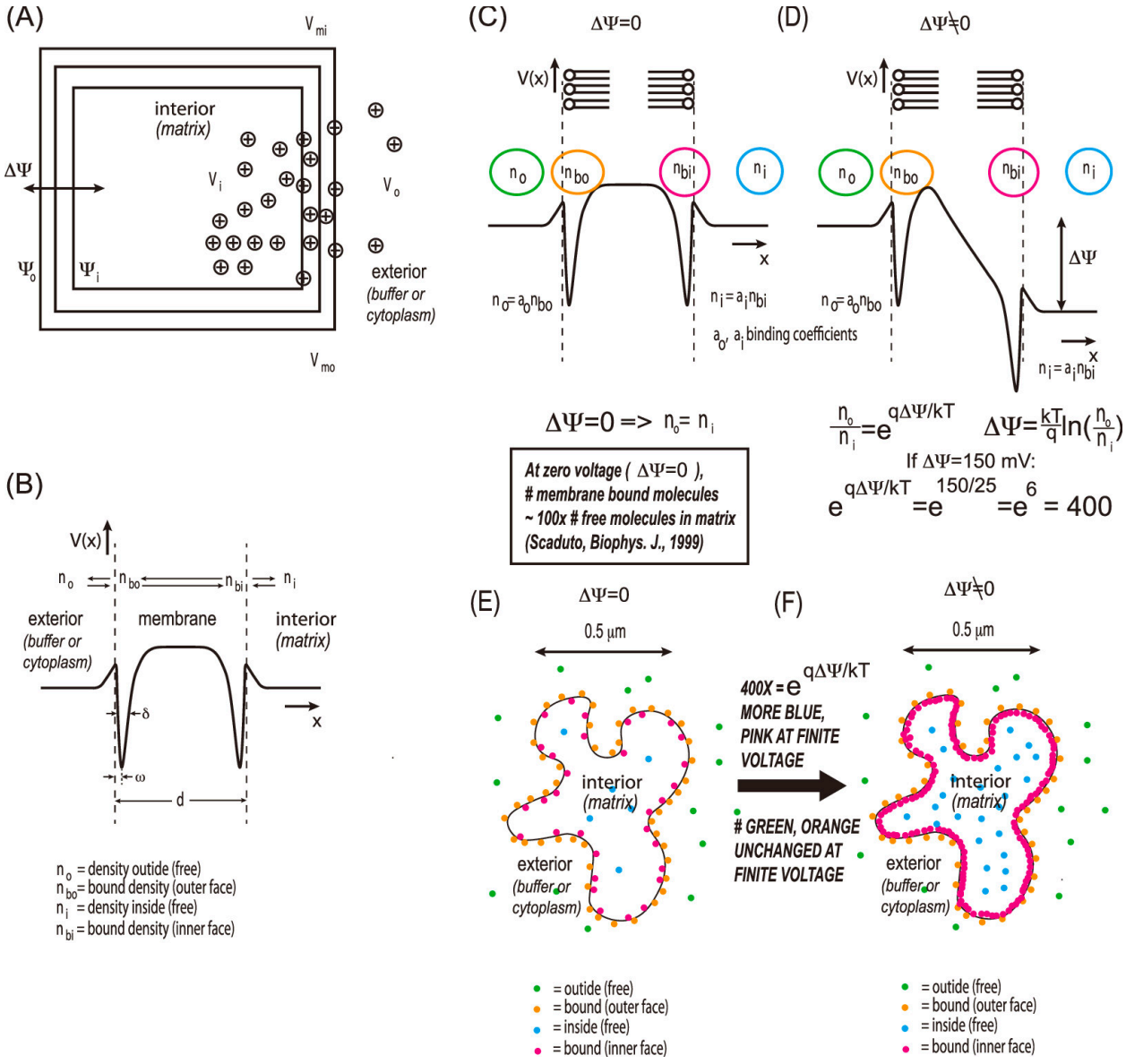

Figure 3-3. Uptake model for TMRE staining of mitochondria for voltage imaging. (A) Four-compartment model, showing membrane binding on both sides as well as the inside and outside. (B) Potential profile. (C, D) Zero and finite voltage potential profile of the binding of TMRE. The green and blue circles show the free TMRE on the outside (buffer side) and inside (matrix side) of the mitochondria. The orange and red circles show the bound TMRE on the outside and inside of the mitochondria, respectively. (E, F) Zero and finite voltage localization of the TMRE, showing the difference in # of TMRE molecules in the different regions. At finite voltage, the most intense fluorescence would be expected from the TMRE molecules indicated by the pink dots, localized at the matrix side of the membrane. The other TMRE molecules (free in the matrix, free in the buffer, bound to the buffer side) would be much dimmer and possibly not even observed within the practical dynamic range limits of the fluorescence detection system used. At zero voltage, the overall intensity (averaged over the organelle) would be much lower, but the intensity distribution would still be expected to be highest near the membrane.

In this model, TMRE is bound on the matrix and buffer (cytosol) side of the inner membrane. The amount of bound TMRE on the matrix side is proportional to the free concentration on the matrix side. The amount of bound TMRE on the buffer (cytosol) side is proportional to the free TMRE concentration on the buffer (cytosol) side. At zero membrane potential, the

inner and outer free concentrations are equal. At nonzero membrane potential, the inner to outer free concentration obeys the Nernst equation; i.e., there is a higher inner concentration. Therefore, there is also a higher amount of TMRE bound on the inner membrane. The amount of TMRE bound on the outer membrane stays the same. It has been known since 1999 [98] that the amount of bound TMRE in the mitochondrial inner membrane is about 100× larger than the amount of free TMRE in the matrix (by mole #), regardless of the potential. Since super-resolution imaging can resolve the cristae, i.e. internal membrane structure, it is mostly the TMRE bound on the inner membrane that is imaged during fluorescence, as it is larger by mole # than the free TMRE in the matrix, and as it is more concentrated (on the surface vs diffuse) in space.

The biophysical basis of this model is shown in Figure 3-3. In this model, TMRE ions experience an effective potential energy profile (for zero voltage) shown in Figure 3-3B (from Rottenberg [108]). The shape of this curve results from the competition between the lipophilic side groups encouraging insertion into the membrane, and the charge encouraging repulsion from the membrane. [108] Since both effects do not have the same spatial profile, this results in two minima in the potential, one at each side of the membrane, and thus two binding sites. The depth and width of the binding sites will determine the concentration of lipophilic cations in the membrane vs the free concentration: The concentration of free (unbound) ions in solution is proportional to the concentration of bound ions on the surface of the membrane. These constants of proportionality (defined as ao and ai in Figure 3-3) must typically be measured empirically (see Supporting Information (SI) section 3).

In Figure 3-4C,D this biophysical model is redrawn under zero and finite membrane potential, showing the TMRE densities bound to each side of the membrane, and free on each side of the membrane, and defining the binding coefficients (also referred to as activities in literature). We prefer the term binding coefficients instead of "activities" sometimes used in the literature, because it explicitly clearly states the physical meaning in this context. Until this work, it was not possible to visualize the location of the TMRE dye molecules in the membrane compartments in mitochondria. However, various indirect techniques have been demonstrated to quantify the membrane binding in this model (see SI section 3). Although Figure 3-4C,D is implicitly what has been used to interpret membrane potential assays on mitochondria in the literature, [99–102] it has never been explicitly presented as we have done in Figure 3-3C,D. The reason is that, until the advent of super-resolution microscopy, it was not possible to image the bound and free TMRE components independently.

Using known rate constants/activity coefficients (see SI section 3), we show in Figure 3-4E,F schematically how the TMRE molecules would be distributed in space at zero and finite membrane potential in a hypothetical mitochondrial inner membrane. Under finite potential, the purple population (TMRE bound to the inner membrane) will create the most fluorescence intensity. The free TMRE in the matrix (blue population) will be relatively dim. This is exactly what we observe experimentally (Figure 3-2). In sum because the # of TMRE molecules bound to the matrix side of the membrane is ~100× larger than the number of free TMRE molecules inside the matrix, and because the membrane bound TMRE molecules are more concentrated on the surface of the membrane, it is the membrane bound TMRE on the inner membrane that "glows" in fluorescence images. This explains why, in our images,

the cristae regions glow with TMRE but the matrix regions seem dark. A detailed accounting of the binding constants is presented in SI section 3.

Application of this model makes two additional predictions that we can test quantitatively: (1) The matrix region should not be completely dark, and (2) the membranes should still be labeled with TMRE even when the membrane potential is completely collapsed. We discuss these next.

3.3.4 TMRE stains the membrane even after the voltage is collapsed

When we collapsed the voltage using CCCP, the total intensity of TMRE averaged over the entire organelle seemingly dropped to zero (Figure 3-4C and Figure 3-2F). However, on closer investigation, we found that it did not completely drop (Figure 3-2G). In the arbitrary units used, quantitatively it dropped to 200 when it was 5000 under energized mitochondria. Using super-resolution microscopy, we could look closer at the distribution of the dye after the collapse of the membrane potential. This is shown in Figure 3-2F. Although the overall intensity is lower, the shape is still similar. The line profile confirms the cristae are still labeled with (bound) TMRE, albeit at a much lower intensity. Thus, prior studies which showed the TMRE collapse are consistent with this work. In addition, this confirms the application of the model we proposed above. These effects are reproducible in different cell lines (see SI section 11).

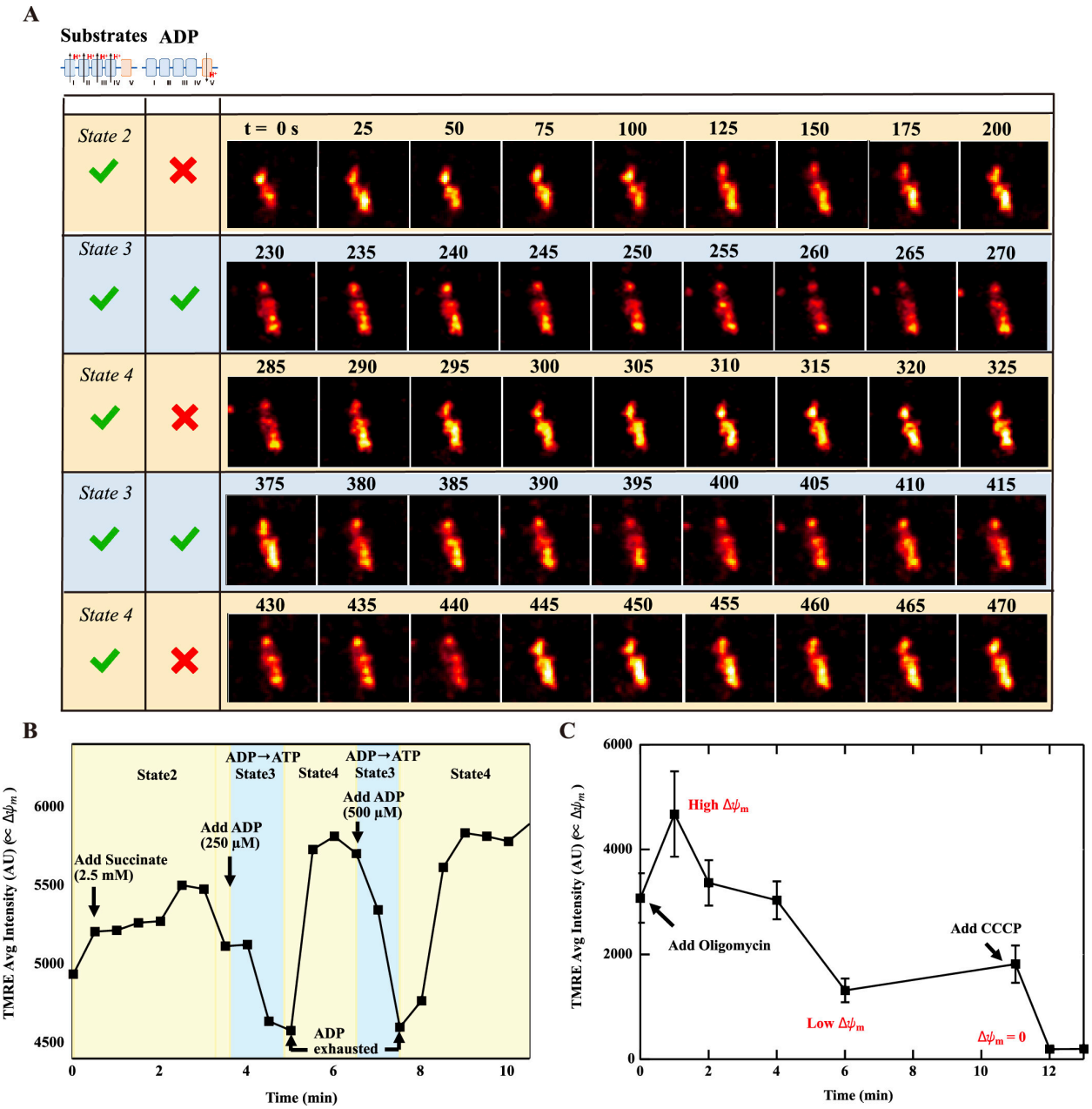

Figure 3-4. Isolated mitochondria TMRE signal in different respiratory states. (A) Mitochondrial structure in different respiratory states. The numbers on top of the figure represent the time in seconds. The pixel size of the image was 0.048 µm, which is limited by the inherent limits of the microscope. (B) Averaged TMRE changes of single mitochondrion during respiratory state transitions. (C) Averaged TMRE changes of single mitochondrion treated with Oligomycin and CCCP. Starting with 178 µg/mL isolated mitochondria, quantified by the Bradford assay, we stained the mitochondria with 10 nM TMRE and collected images using time-steps of 5 s to avoid photobleaching. The succinate (2.5 mM) was added at the 10th second, and ADP was added at the 240th second and again at the 380th second, giving a final concentration of 250 µM and 500 µM, respectively.

3.3.5 There is some TMRE fluorescence in the matrix

According to the model, the free concentration of TMRE (inside the matrix), though small, should be observed in both cases whether the membrane potential ΔΨm = 0 or not. This fits

our observation in Figure 3-2F. The TMRE intensity in the matrix, in arbitrary units used, was nonzero even after CCCP collapsed the voltage.

3.3.6 Postfacto Justification To Use Nernst Equation in TMRE Imaging Studies

At zero voltage, the bound TMRE is split roughly 50/50 on the inside/outside binding site. At finite voltage, the TMRE bound to the outside stays the same, but the TMRE bound to the inside is larger by a factor of e∧(−qΔΨm /kBT). For a typical membrane voltage of 150 mV, this is a factor of 400. Therefore, at finite voltage, the intensity of fluorescence is dominated by the TMRE bound to the matrix side of the membrane. In this way, the Nernst equation can be used as a semiquantitative measure of the local voltage of the membrane. Furthermore, it can even be used to determine the local voltage. Only when the voltage gets low compared to kT does this approximation break down. This postfacto justifies the use of the Nernst equation to image the membrane voltage in super-resolution microscopy studies of live cells and mitochondria, and studies where only the total uptake of TMRE is measured, which was the case for all studies until our super-resolution study. This means future researchers can use the Nernst equation in super-resolution studies of mitochondrial membrane potential with this justification, but the interpretation should include rather than ignore the membrane binding, quantitatively modeled in this paper in the context of super-resolution microscopy.

3.3.7 Bulk models may break down in the cristae: There is only one (calculated) H+ ion in the cristae solution at known pH values, but electric fields are extremely intense

We now discuss the distribution of various charged species near a single cristae finger (Figure 3-5). Note that this is for discussion purposes only and does not detract from the main result of the paper that TMRE is localized on the matrix side of the mitochondrial inner membrane when there is a sustained membrane potential. In this discussion, we seek to put into perspective the electric fields, pH, and ionic species of the mitochondria as a whole organelle, from a systems perspective, and to indicate schematically what the TMRE fluorescence images represent physically.

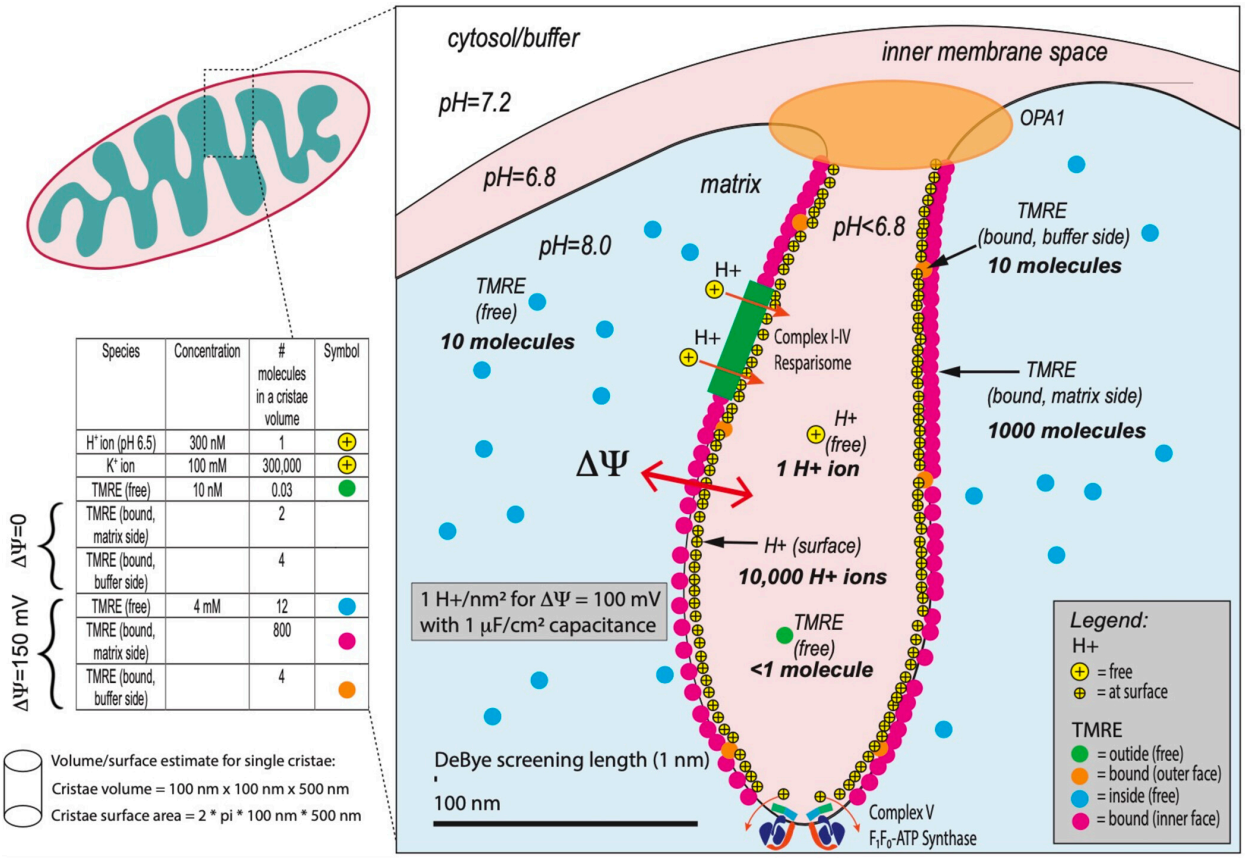

Figure 3-5. Schematic diagram of several different species and their distribution within a single cristae finger. Not shown are the OH- species on the membrane needed to maintain charge neutrality.

We first discuss TMRE distribution. As discussed above, at the TMRE concentration used, the TMRE charge density is small compared to the other ionic species. Therefore, the TMRE does not significantly change any electric fields; rather it only acts as a probe of those fields and responds to them. Approximating a single cristae finger as a cylinder of diameter 100 nm and length 500 nm for volume and surface area estimates, and using known binding constants discussed in detail above and in the Supporting Information, based on a membrane potential of 150 mV, we find there will be ~1,000 bound TMRE molecules at the surface on the matrix side of a single cristae finger (red dots). These give the dominant observed fluorescent signal in super-resolution images. The TMRE is positively charged, so there will be ~1000 negative charges on the other side of the membrane (cytosol/buffer side), presumably OH^- species (not shown). The remaining TMRE is small in number and difficult to observe in super-resolution images: In the matrix, there will be ~10 free TMRE molecules in the field of view (blue dots). Inside the finger, there will be less than one free TMRE molecule (green dot) and less than ~10 bound TMRE molecules (orange dots) on the cytosol/buffer side of the membrane.

We turn next to the unbound hydrogen H^+ and OH^- species. We assume the pH = 7.2 in the cytosol/buffer. Because protons are pumped out of the matrix, the matrix must be at a higher pH than the cytosol/buffer. While the exact matrix pH is difficult to measure, it is generally

accepted to be between 7.4 and 8 (corresponding to a delta pH across the mitochondrial membrane of somewhere between 0.2 and 0.8 pH [39,109–113]). The intermembrane space (IMS) has a lower pH than the cytosol. Although not exactly known, these are indicated as 7.2, 6.8, and 8.0 in the cytosol (buffer), intermembrane space (IMS), and matrix, respectively, in the figure. We and others [39] have shown that protons are concentrated in the cristae fingers since the OPA1 and MICOS complexes block proton transport through the tight cristae junctions. Since the source of the protons is dominantly inside the cristae fingers where the components of the ETC are localized, [84] the effective pH inside the finger would be lower than the IMS, i.e. lower than 6.8. In order to estimate the # of protons inside a single finger, we estimate the volume as a cylinder of diameter 100 nm and length 500 nm. Based on this, if the pH inside the finger is 6.5, there will be statistically about one H+ ion in one cristae. Since the application of the concept of pH assumes a statistical distribution of a large number of OH– and H+ ions, its application to a volume with less than one H+ ion indicates that a new model is needed.

We now turn to bound hydrogen H+ and OH– species. Since there is a membrane potential of around 150 mV across the membrane, by Gauss's law of electrostatics, there must be a sheet of positive charge on the inside of the cytosol/buffer side of the membrane (pink area), and a corresponding sheet of negative charge on the matrix side of the membrane (blue area). Based on an estimated bilayer capacitance per unit area of 1 μF/cm2, the amount of charge can be estimated as one electron equivalent of charge per nm2, positive on the cytosol/buffer side of the membrane, negative on the matrix side of the membrane. We postulate that the molecular identity of positive charges on the cytosol/buffer side are H+ ions, since these are the ions that are actively and continuously being pumped by the ETC to maintain the membrane potential. Approximating the total surface area of a single cristae finger's membrane as a cylinder of diameter 100 nm and length 500 nm, the number of estimated charges per cristae finder is 10,000 (shown as yellow circles with a plus sign). Similarly, there would be 10,000 OH– charges on the matrix side of the membrane (not shown).

The electric fields inside the cristae are intense. This huge imbalance between one free H+ ion and 105 on the surface must affect the electrostatics inside the cristae to create immense electric fields. This would also have a huge potential to impact the protein complexes in the ETC. Clearly, a new model, not based on bulk, continuum distributions of charge and pH, which takes into account the immense electric fields and their impact on the ETC performance under different metabolic conditions is needed. The recognition of the few # of protons in a mitochondrion was also recently pointed out by Silverstein. [114] Development of theories and experiments in this "stochastic" limit has begun in test systems. [115,116] It has been shown that the classical definition of pH in very small volumes needs to be revised when applied to fluorescent probes of pH in mitochondria. [117] Our super-resolution studies represent a significant step in experimentally dissecting the super-resolution electrophysiology of this organelle.

It is not unreasonable to speculate that, even given the Debye screening length of a few nanometers, at least in some regions of the cristae, the effective pH is not 6 or 7 but much more acidic, [118,119] even approaching pH 1. One might even speculate even further that these

strong fields affect the spin polarization and may even give rise to quantum effects in the microscopic environmental chemistry or even the macroscopic phenotype. Hints of this have already been reported in the literature. [120] While in their infancy, super-resolution studies such as these, combined with quantum probes of mitochondrial function, [121] may enable powerful methods of probing the connection between energy and life.

3.4 Conclusion

High spatial resolution cristae electrophysiology during different metabolic states can be studied with isolated mitochondria using super-resolution microscopy. Based on the correct interpretation of Rottenberg's 1984 membrane binding model, [108] we can now quantitatively study mitochondria super-resolution electrophysiology and ultrastructure in different metabolic states. Motivated by the original observation by Hackenbrock [90,91] that mitochondrial morphology changes in response to metabolic status (measured via TEM), we aimed to determine if the electrical voltage distribution also changed. We imaged the membrane potential (via super-resolution imaging of the TMRE fluorescence intensity) of intact, functional isolated mitochondria under different respiratory states, using pharmacological manipulation of the electron transport chain. Figure 3-4A shows the time-lapse super-resolution images of mitochondria in different respiratory states. In this study, we fed electrons into the ETC through complex II using succinate as the substrate to initiate state II respiration. We then added ADP to initiate state III respiration which on completion of ADP phosphorylation resulted in state IV respiration. [7] This demonstrates real-time, live imaging of the voltage changes in mitochondria with the ultrastructure clearly resolved, as the mitochondria are put into different metabolic states.

Using this method, we demonstrate that the TMRE fluorescence intensity (indicative of local membrane potential $\Delta\Psi m$) is bright in both metabolic states, getting brighter in state IV (defined as the presence of substrates but without ADP hence without ATP synthesis), and getting dimmer when ADP is present (due to the synthesis of ATP consuming some of the energy stored in the membrane potential). Furthermore, we show clearly that the dark regions remain dark in both metabolic states. This clearly indicates that the primary binding site of the fluorophore is at the cristae, when it comes to electrical voltages, regardless of the metabolic state.

Figure 3-4B shows the average TMRE fluorescence intensity over the entire organelle (defined as a region-of-interest (ROI) as discussed in the Methods section and SI section 7) as a function of time, under different buffer chemistries designed to manipulate the ETC and, thus, the mitochondria membrane potential. The implicit assumption is that the TMRE average so determined can be used as ni in the Nernst eq 1 to determine the $\Delta\Psi m$ average.

Consistent with the expectations from standard respiration studies, [7] including our studies with external TPP+ electrodes which corroborated the findings, [99,100] succinate addition increased TMRE fluorescence indicating the rise in mitochondrial membrane potential (Figure 3-4C). Addition of ADP caused a decline in TMRE fluorescence indicative of the utilization of the membrane potential by the ATP synthase to convert ADP to ATP, and when the phosphorylation of ADP was complete and the ATP synthesis stopped, the TMRE

fluorescence increased due to the recovery of the membrane potential via state IV respiration. A second addition of ADP repeated the state III to state IV progression.

Additionally, to confirm prior results still apply in our measurements, we showed that oligomycin causes the TMRE fluorescence to increase (indicating that the average membrane potential increased): Inhibition of the ATP synthase with oligomycin drives the mitochondrial electrochemical gradient to its maximum resulting in maximum TMRE uptake and fluorescence. Prolonged oligomycin exposure caused the membrane potential to decline, a phenomenon commonly observed, perhaps due to the activation of the mitochondrial permeability transition pore (mtPTP). Furthermore, we showed that, with the addition of CCCP, the average TMRE fluorescence drops close to zero: Treatment with the mitochondrial uncoupling agent CCCP collapses the inner membrane electrochemical gradient resulting in the release of the mitochondrial TMRE and minimal mitochondrial fluorescence. Hence, with intact, functional mitochondria, the uptake and release of TMRE follow the expectations of changes in the mitochondrial membrane potential during OXPHOS function. This is reproducible over all 4 cell lines studied (see SI section 12). Additionally, mitochondrial heterogeneity as well as spatial and temporal fluctuations can be further analyzed (see SI section 16).

Chapter 4. PHOTOBLEACHING AND PHOTOTOXICITY OF MITOCHONDRIA IN LIVE CELL FLUORESCENT SUPER-RESOLUTION MICROSCOPY

4.1 Introduction

Mitochondria are highly dynamic organelles, whose size, connectivity, and ultrastructure are controlled through balanced and dynamic cycles of fission, fusion, and cristae modifications. Analysis of mitochondrial structure and function is increasingly being recognized as central to understanding human health and disease [3–6,11,82]. Yet, mitochondria within tissue cells can have markedly different structures and functions.

In healthy cells, mitochondria form a tubular morphology (mitos being Greek for "thread"). Starting from the very first studies of the morphology of isolated mitochondria [90,91], researchers have consistently observed that the morphology of the vital isolated mitochondria is spherical, either by using optical or electron microscopy. This includes our own work [37,38]. Since mitochondria fission/fusion has important physiological and clinical consequences [122–124], the morphology of mitochondria under stress and toxic stimulus is an important topic in metabolism and cell biology, linked to a myriad of clinical pathologies.

Recent advances in live cell super-resolution microscopy have enabled imaging of mitochondrial ultrastructure [95–97,125–137]. However, the enhanced resolution achieved in super-resolution microscopes often comes at the expense of high-intensity illumination [131], which can result in photobleaching and phototoxicity effects [93,94,96,97,129,130,132,133,138–141]. These effects have the potential to negatively impact cell viability and compromise the integrity of the collected data. A single set of standards for assessing the potential of phototoxicity cannot currently be proposed due to the involvement of multiple factors, such as illumination wavelength, intensity, duration, illumination regime, and sample characteristics [132,140,142]. Observing the degree of photobleaching is commonly used to evaluate photodamage [143,144], but phototoxicity and photobleaching are distinct processes, with phototoxicity potentially occurring even before a noticeable decrease in imaging quality. More effective measures of mitochondrial phototoxicity could include reduced metabolic activity, compromised membrane integrity, DNA fragmentation, elevated reactive oxygen species (ROS), or initiation of apoptosis [134,135,145,146]. Efforts to reduce photobleaching and phototoxicity in super-resolution microscopy [96,136,147] include controlling light exposure [137,143,144], using photostabilizing buffer [148], or developing more stable fluorescent dyes [128,133].

Mitochondrial "sphericity" is one parameter of mitochondrial damage which has been associated with aging, apoptosis, and chemical insults [149–155]. Progressive sphericity has been observed using a variety of imaging systems including stimulated emission depletion (STED) microscopy and structured illumination microscopy (SIM), in association with photobleaching and phototoxicity. Minamikawa et al. [139] found that Chloromethyl-X-rosamine (MitoTracker Red) was associated with potent phototoxicity at light doses of > 2 J/cm^2 using confocal microscopy, in association with a rapid decrease of the mitochondrial membrane potential and a globular swelling of mitochondria. Wang et al. [133] developed a photostable fluorescent marker for STED microscopy, MitoPB Yellow, which had a high resistance to photobleaching and permitted monitoring of mitochondrial ultrastructural

over an extended period of the mitochondria associated with experienced swelling and the loss of cristae, attributed to photodamage induced by the intense STED laser. Yang et al. [129] utilized the Hessian-SIM microscopy to show that extensive illumination induced rapid swelling of mitochondria, deformation and abruption of inner-membrane cristae, and round, hollow mitochondria. Liu et al. [128] developed a photostable fluorescent dye, PKMO, which drastically reduced the photobleaching and phototoxicity effects compared to other fluorescent dyes that lead to visible swelling and a drop in mitochondrial membrane potential. In summary, mitochondria, by empirical super-resolution microscopy data, tend to show loss of membrane potential and morphological changes from tubular to spherical as general responses to phototoxicity.

All of these new dyes as well as existing dyes such as but not limited to additional Mitotrackers (ThermoFisher) beyond the one we use here (Mitotracker Green, MTG), MitoBrilliant (Tocris), MitoView (Biotium), and PKMito (Spirochrome/cytoskeleton) point to the need for a solid understanding of the effects of photobleaching and phototoxicity on interpretation of imaging data. As many of the new dyes cited above are in the research and not commercially available yet, it is up to the authors of those research dye papers, as well as any future dye papers, to carefully use the techniques and methods we present in this paper on their own, or by seeding the dyes to other beta tester groups. This includes measuring the initial brightness, photobleaching rate, and phototoxicity. Such third-party evaluation would add considerable value to the entire mitochondrial community, which would further underline the importance of our methodology. Such a comprehensive study would be the ultimate goal of the initial work presented in this manuscript.

In order to begin this journey, we have decided to study the most broadly used, easiest-to-obtain dyes, that are compatible with all microscopes, from those in budget labs with only epi-fluorescence microscopy, to intermediate equipped confocal microscopy, to the well-funded labs with expensive advanced state of the art superresolution microscopes, such as STED, SIM, Airy, etc [156,157]. Therefore, this paper will have broad applicability to all mitochondria imaging studies.

The dyes MTG and NAO are the most commonly used structure dyes in the field of mitochondrial imaging. TMRE/TMRM is the most commonly used voltage dye, and in fact the only voltage dye in modern use. Many recent refs in the last 12 months show that these dyes continue to be the workhorse, mainstay, and defacto industry standard dyes in use to measure mitochondrial function and structure in standard and super-resolution microscopy [158–164]. While some data is available on the toxicity and bleaching of these dyes [98,165], no comprehensive set of data has yet been presented. In this work, we present our carefully designed experimental data on the subject of the two related phenomena of photobleaching and phototoxicity. While the mechanisms of both of these are not well understood, our data provide a very important basis set on which to build models of mechanisms, and, practically, a guide for researchers in the field. In the end, we speculate on some mechanisms that may be responsible for the phenomena we observe.

Specifically, the fluorescent dye, NAO, is a widely used mitochondrial marker that binds to cardiolipin, a polyunsaturated acidic phospholipid localized in the mitochondrial inner

membrane, providing clear images of cristae ultrastructure. However, NAO was reported to have cytotoxic effects when incubated at high concentrations [165] of an unknown mechanism. Victor et al. [166] proposed that NAO promotes strong membrane adhesion via van der Waals interactions between anti-parallel H-dimers of NAO molecules from the opposing bilayers, which led to the membrane remodeling of the mitochondria cristae. Using the Airyscan super-resolution microscope, we find that NAO exhibits a phototoxic effect causing rapid loss of fluorescence and membrane potential, which was separate from the cytotoxicity due to high concentration incubation. Employing TMRE as a voltage tracker and NAO or MTG as structure trackers, we found that both NAO and MTG could effectively act as fluorophores for imaging the mitochondrial membrane, but that NAO caused significant phototoxicity and loss of mitochondrial membrane potential.

4.2 Materials and Methods

4.2.1 Cell Culture and Fluorescent Dye Staining

The HEK293 cells and HeLa cells used in this research were purchased from ATCC. All the cells were cultured for 2−3 days in 75 cm2 tissue flasks at 37 °C and 5 % CO2 before being ready for experimentation. Dyes (10 nM TMRE and 100 nM MitoTracker Green (MTG) or 100 nM 10-N-nonyl acridine orange (NAO); Santa Cruz Biotechnology) were added to the cell culture media and incubated 1 h prior the cell retrieval.

4.2.2 Live Cell Fluorescent Microscopy of Mitochondrial Dynamics

The cells were seeded in CELLview 4-compartment glass-bottom tissue culture dishes (Greiner Bio-Ones, 627870), PS, 35/10 mm, 24 hours prior to imaging. The live cell experiments were performed in the Zeiss LSM900 microscope with an incubation chamber (set to 37 °C). Imaging of cells were performed using Airyscan an alpha Plan-Apochromat 63×/1.4 Oil DIC M27 objective. The laser powers were adjusted between approximately 0.3% to 2%, and the master gain between 750 and 900. We started continuous scanning at maximum speed at a zoom factor of 1, in order to obtain a relatively strong signal-to-noise ratio for imaging. Later, we brought the field of mitochondria of interest into view and stopped scanning. The pixel dwell time was set between 0.85 and 1.04 μs, respectively to avoid overtime exposure of mitochondria to the laser. NAO and MTG were used for structural imaging (labeling the lipid bilayer), and TMRE was used for voltage imaging, as explained in the main text.

4.2.3 Image Processing and Mitochondrial Quantification

Image processing and quantification were completed using Zeiss Zen 3.5 software, ImageJ, Igor Pro, OpenCV, and Python. Images were deconvoluted using the Airyscan Super-resolution processing function with the optimal auto-filter setting. Following deconvolution, a Gaussian blur filter was used to denoise the image, and a top hat morphological transformation was performed to subtract non-mitochondria objects using ImageJ. Using Python and OpenCV, we performed K-Means clustering to separate the fluorescent intensities in the image into 2 groups: mitochondria and non-mitochondria. Finally, a particle

analysis was done on the mitochondria group to measure the perimeter and circularity of mitochondria using ImageJ. Statistical analysis and plots were generated using Igor Pro.

4.3 Results and Discussion

4.3.1 Photobleaching vs. phototoxicity

In an ideal world, the effects of photobleaching and phototoxicity would be unrelated, and could each be independently studied. Photobleaching could be studied via observation of the decay of fluorescence intensity vs. time. Phototoxicity, in this paper, is assayed via two metrics: 1) Change in mitochondrial morphology, from tubular to spherical, and 2) Change in mitochondria membrane potential, which would be (ideally) independently measured and observed.

A priori, several challenges exist already with such a research program/paradigm. First, and most obvious, phototoxicity and photobleaching may and typically do occur simultaneously. This complicates the interpretation and determination of cause/effect, if there is any relationship between the two. Second, with voltage dye TMRE (as well as other variations of fluorescence lipophilic cations such as rhodamine123 and JC1 [167]), the loss of mitochondrial membrane potential causes loss of fluorescence intensity by definition of how it is employed with the Nernst equation. (For an up-to-date in-depth discussion of the voltage contrast mechanism, the reader is referred to our recent paper on the topic [168]). Therefore, a priori, one cannot distinguish between a voltage drop caused by phototoxicity leading to reduced fluorescence intensity and reduced fluorescence intensity caused by photobleaching. A third complication comes from the fact that virtually all dyes show some voltage-dependent binding, and are not purely structural labels. A more nuanced and subtle approach is necessary to decouple the two effects.

To address these complications, the are several possible avenues to explore. For TMRE one option is to study TMRE photobleaching independently, and then based on that data/experience, if TMRE intensity reduces faster than expected based on the photobleaching data, it must be due to reduced membrane potential. In fact, we find that to be the case in several of the experiments discussed below. Then, the voltage reduction due to phototoxicity can be independently determined from the photobleaching. Another option is to use morphology as the metric for phototoxicity, which can be measured even in the presence of photobleaching.

For the voltage dependence of structure dyes, one option is to quantify this. If the dye intensity changes more than the voltage dependence alone would predict, then it is due to photobleaching.

A postiori, we find that the use of two dyes NAO and TMRE at the same time causes phototoxicity (determined by morphology change and membrane potential drop) that is not caused by the individual dyes. This is explained in detail below.

4.3.2 NAO vs, MTG photobleaching

In our first series of experiments, we set out to determine the relative photobleaching of structure dyes NAO vs MTG, independent of phototoxicity. Therefore we concentrate on the relative fluorescence intensity and ignore structural changes due to phototoxicity. Both dyes are known to localize in the mitochondria. NAO is known to have some dependence on mitochondrial membrane potential [104,169,170]. Quantitatively, it changes the fluorescence intensity of the organelle by about 50% upon complete depolarization of vital mitochondria. Therefore, any additional change in fluorescence intensity beyond this can be attributed to photobleaching.

The spectrum of NAO and MTG is similar, both being pumped at 488 nm with emission at around 520 nm. We observe that NAO manifests significantly faster photobleaching than MitoTracker Green (MTG). Figure 4-1 shows a comparison of HeLa cells stained with MTG and NAO before and after 300 frames of exposure to 488 nm laser illumination. Note, all experiments in this manuscript are taken at a frame rate of 1 frame per second, and we use time in seconds in the x-axis to better present the changes in fluorescence and morphology over time. Each image had 572 pixels horizontal and vertical, with a dwell time of 3.54 μs per pixel, and the laser power set to 0.5 %. 100 % laser power is estimated at 1 mW [171]. In this test, the fluorescence intensity of mitochondria stained with MTG dye decreased by ~ 60 % during the experiment (The mean fluorescence intensity over all mitochondria within the entire cell) and the morphology of mitochondria retained the tubular structure before and after the illumination. On the other hand, the fluorescence intensity of mitochondria stained with NAO dye decreased by ~ 80 % in the first 50 frames and by ~ 90 % after 300 frames.

The loss of NAO intensity may be partially due to mitochondrial membrane potential change upon illumination (phototoxicity). However, the overall drop is over 90% (The mean fluorescence intensity dropped from 10312 AU to 213 AU). Therefore, at least part of the drop can be attributed to photobleaching. The photobleaching component of NAO is significantly faster than MTG. The 1/e lifetime value is 214 seconds for MTG and 14 seconds for NAO.

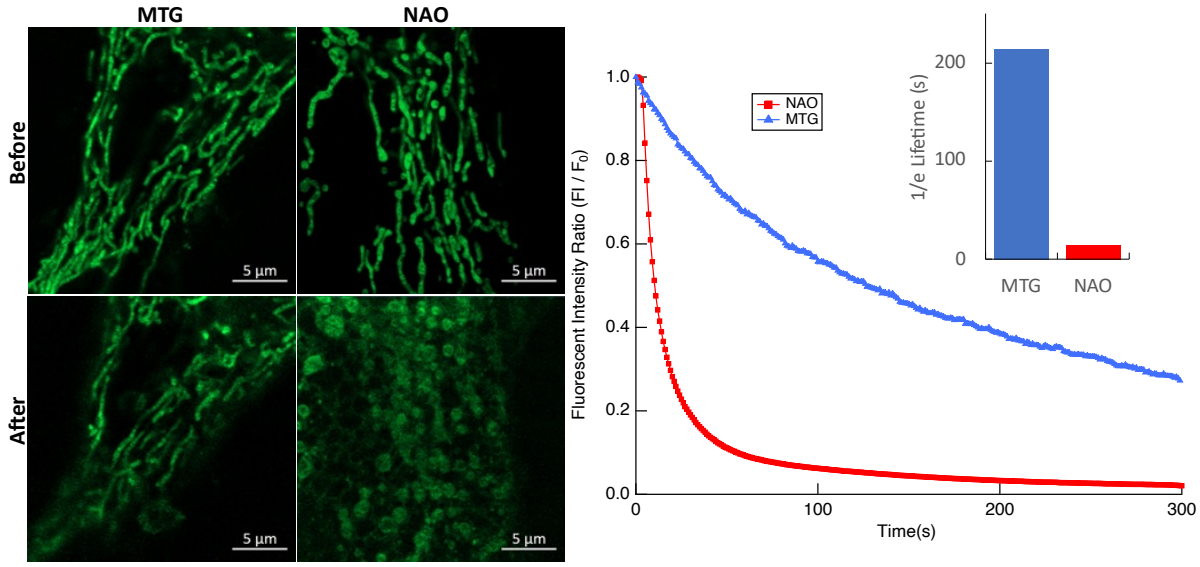

Figure 4-1. Assessing photobleaching in time-lapse imaging with NAO and MTG. (A) Image of mitochondria stained with NAO and MTG before and after exposure to 488 nm illumination for 300 seconds. (B) NAO and MTG fluorescence intensities versus frames. N ≥ 3 independent experiments. (Intensity: 0.5 %; Pixel time: 3.54 µs; Time frame: 1 s)

4.3.3 NAO vs. MTG phototoxicity measured by morphology

Another phenomenon to access mitochondrial phototoxicity is the transformation of mitochondria from tubular to spherical shape. This is a non-reversible transformation different from mitochondria fission and fusion. Figure 4-2 demonstrates time-lapse phototoxicity-induced ultrastructural changes of mitochondria in live cells, including changes to the outer morphology as well as the cristae structure. The mitochondria in HeLa cells were stained with 100 nM NAO and exposed to illumination with an excitation wavelength of 488 nm every 5 s for 60 frames. The filming time for each frame was 94 ms and we observed the mitochondria start to shrink into a spherical shape and the cristae tended to stack toward two edges of the mitochondrion leaving a hollow space in the middle. The same result was also observed when imaging mitochondria in HeLa cells stained with 50 nM MTDR by using the stimulated emission depletion (STED) microscope.

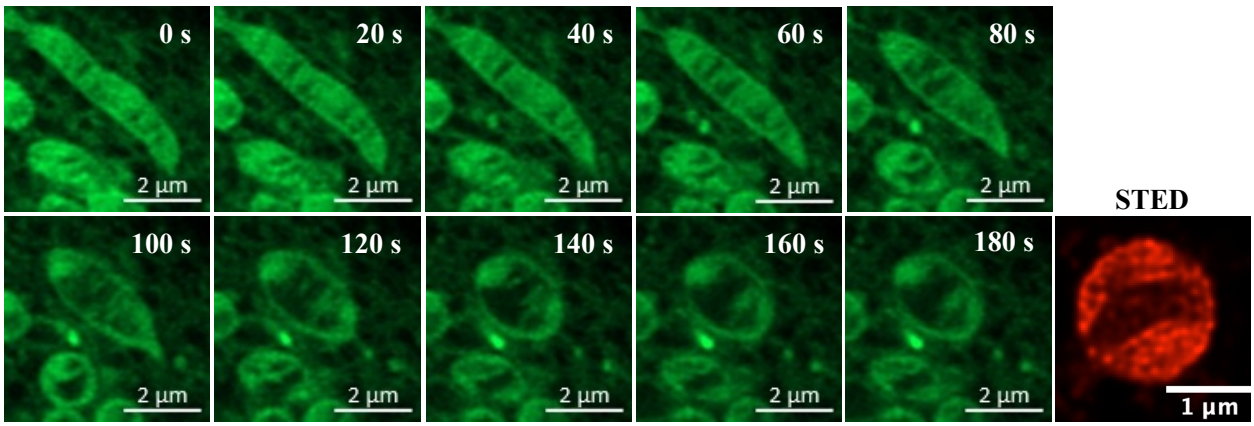

Figure 4-2. Phototoxicity causes mitochondria ultrastructure to be destroyed. (Green) Time-lapse images of mitochondria stained with 100 nM NAO in HeLa cells using Zeiss Airyscan. (Red) Image with STED after sufficient time to cause mitochondria to become spherical shows similar morphology. N ≥ 3 independent experiments. (HeLa cell)

Quantification of morphological changes was achieved following a detailed protocol that incorporated analysis software as described in Methods. This protocol assessed individual mitochondrial features in single cells (Figure 4-9). To determine sphericity, we calculated the 2d circularity (as a stand-in for 3d sphericity) by the ratio of the perimeter to surface area. A perfectly spherical mitochondria will have a perimeter/area ratio of 2 pi r/ (pi r^2). We define circularity as circularity = 4π (area/perimeter^2), a circularity value of 1.0 indicates a perfect circle. As the value approaches 0.0, it indicates an increasingly elongated polygon (tubular). This dimensionless parameter was calculated using imaging processing software. An unsupervised K-means algorithm was used to determine the intensity threshold value of each image to accurately distinguish true mitochondria pixels from background fluorescence. Image thresholding and a binarization protocol allowed us to standardize and automate the selection of mitochondrial objects. The computer-identified mitochondria objects were manually inspected and compared to the original images before further morphology analysis using ImageJ.

During the timeframe of the above photobleach experiment (Figure 4-1, 300 seconds), no morphology change was observed in the MTG case, indicating a lack of phototoxicity. In contrast, NAO illumination resulted in mitochondrial morphology changing from tubular to spherical, indicative of phototoxicity. NAO-stained mitochondria underwent a morphological change with the average circularity (a measure of phototoxicity) increasing from 0.4 to 0.7 within 100 seconds of illumination (Figure 4-3). On the other hand, MTG-stained mitochondria maintained their tubular morphology through the illumination, with 0.2 to 0.4 for circularity. This indicates NAO is significantly more phototoxic than MTG.

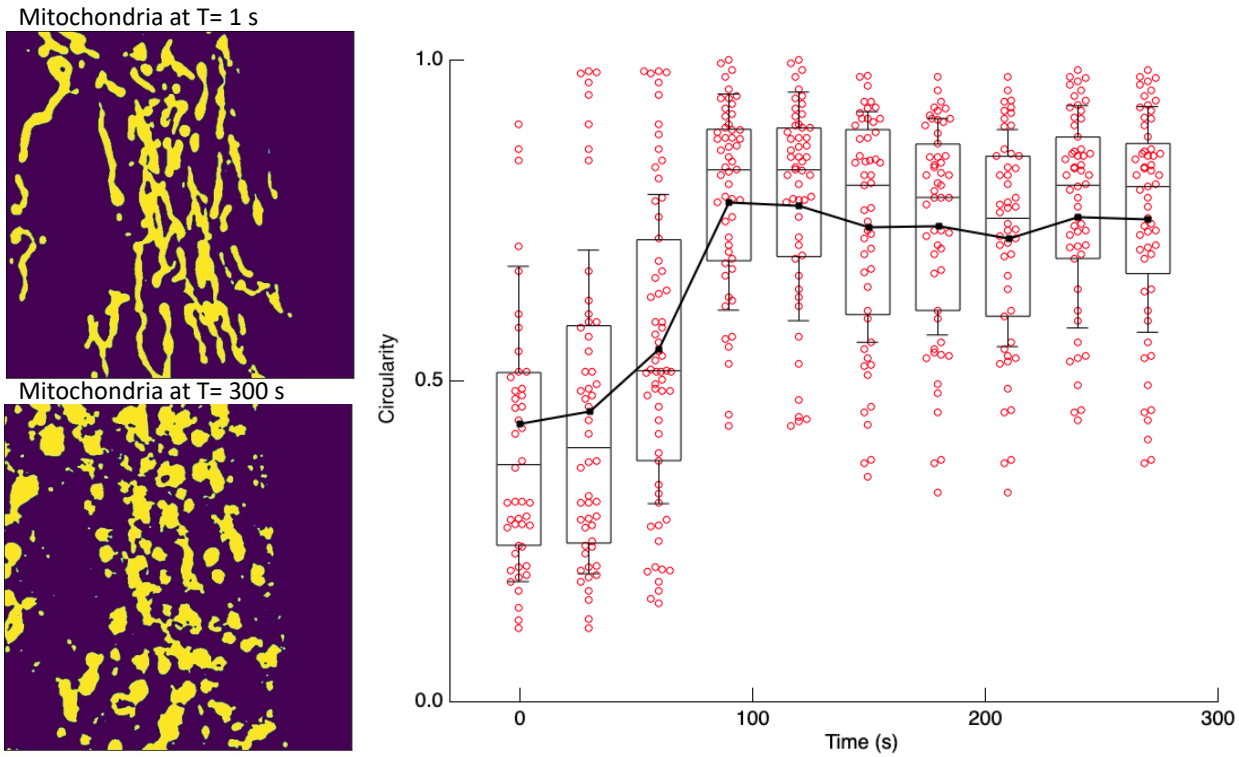

Figure 4-3. Mitochondria segmentation and structure analysis. The binarization mask is used for single mitochondria analysis. The statistical analysis shows the change of circularity of mitochondria in cells through the time-lapse experiment. The mitochondria in the HeLa cell were stained with 100 nM NAO (Intensity: 0.5 %; Pixel time: 3.54 µs; Time frame: 1 s).

4.3.4 NAO vs. MTG phototoxicity measured by membrane potential

In a second set of experiments, we aimed to assess phototoxicity through loss of membrane potential. We used TMRE to assess the membrane potential, a fluorescence dye that has a large dependence on membrane potential (changing over an order of magnitude on depolarization with FCCP, see e.g. Fig 4c in Ref [168]).

We observed that prolonged exposure of NAO-stained mitochondria to 488 nm illumination reduced or even dissipated the mitochondrial membrane potential. Figure 4-4A shows a time-lapse experiment of mitochondria stained with NAO and TMRE exposed to 488 nm and 561 nm illuminations. The 488 nm was used to excite NAO while 561 nm was used to excite TMRE. Both NAO and TMRE fluorescence disappeared after a couple of images were taken, which was different from our experience in multiple cell lines (HeLa, HEK293, and L6) stained with MTG and TMRE (Figure 4-10). To further verify the cause of the membrane potential loss, we stained the mitochondria in live HeLa cells with NAO and TMRE dyes and exposed them to (a) 488 nm and 561nm illuminations, and (b) only 561 nm illumination. Figure 4-4B showed that for the group exposed to 488 nm and 561 nm illumination, both the NAO and TMRE fluorescence intensity dissipated over 90 % within the first 10 seconds. By contrast, when HeLa cells were interrogated with only the 561 nm illumination, the photobleaching effect was reduced, with TMRE fluorescence lasting for over 30 seconds before dropping to 50 %. Hence, we deduced that the rapid loss of NAO fluorescence and

membrane potential can be attributed to the exposure of NAO to 488 nm illumination. This is a surprise and the mechanism is currently unknown.

The reduction in TMRE intensity alone when pumped at 561 nm may be due to either photobleaching or phototoxicity of TMRE. In this experiment alone, the two effects cannot be disentangled. This effect is also observed using other cell lines (Figure 4-11). On the other hand, the rapid reduction in TMRE intensity upon an additional 488 nm illumination (used to pump the NAO) can be attributed to the phototoxicity of the NAO. This effect is not present when 488 and 561 nm are used simultaneously in the absence of NAO.

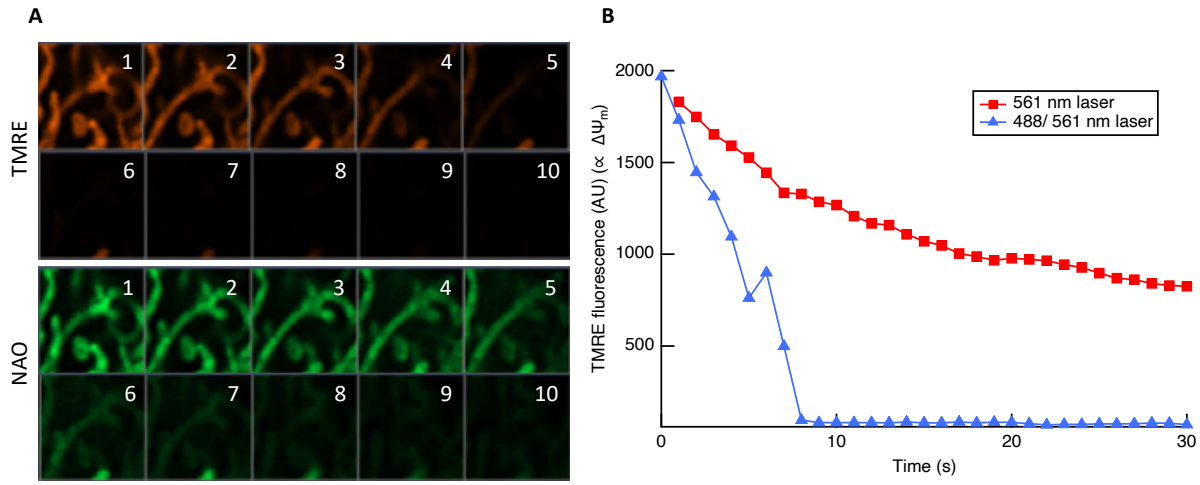

Figure 4-4. Assessing NAO phototoxicity in loss of mitochondria membrane potential. (A) Time-lapse images of mitochondria in HeLa cells stained with 10 nM TMRE and 100 nM NAO, and exposure to 488 nm and 561 nm illuminations (Intensity: 0.5 %; Pixel time: 1.43 µs; Time frame: 1 s). (B) TMRE fluorescence intensity of mitochondria exposure to 561 nm only illuminations versus time.

4.3.5 Investigating the mechanism of NAO phototoxicity: Comparison to high concentration experiments

A high concentration of NAO is known to trigger cytotoxicity even without excitation [165]. Under higher concentrations (>1 µM) than those used here, NAO inhibits cellular respiration and eventually triggers the morphological changes in mitochondria. Various mechanisms for this have been proposed. Victor et al. [166] proposed strong membrane-membrane adhesion would disrupt mitochondrial ultrastructure promoted by NAO under high concentration. This adhesion is proposed to be facilitated through van der Waals interactions between anti-parallel H-dimers of NAO molecules located in opposing bilayers. Consequently, this process is proposed to cause remodeling of the mitochondria cristae membranes. In their reported data, mouse embryonic fibroblasts (MEF) cells stained with high concentration (5 µM) of NAO demonstrated a shift in the emission range from λ_{em} = 525 nm to 640 nm (green-to-red shift), as evidence of NAO H-dimer formation. On the other hand, cells stained with low concentration (5 nM) of NAO did not. In order to verify whether the observed rapid loss of fluorescence, loss of membrane potential, and morphological deformation that we observed above are the result of a high concentration cytotoxic effect observed by [166], we repeated our above experiments with an even lower concentration of NAO (10 nM vs 100 nM) and found

identical results, indicating that the phototoxicity we observed was not due to high concentration effects. Figure 4-5 shows that even under 10 nM of NAO incubation, the mitochondria also experienced a rapid loss of fluorescence, loss of membrane potential, and morphological deformation. As above, these effects were also triggered by 488 nm laser excitation, which we did not observe when excited the mitochondria with 561 nm laser excitation only.

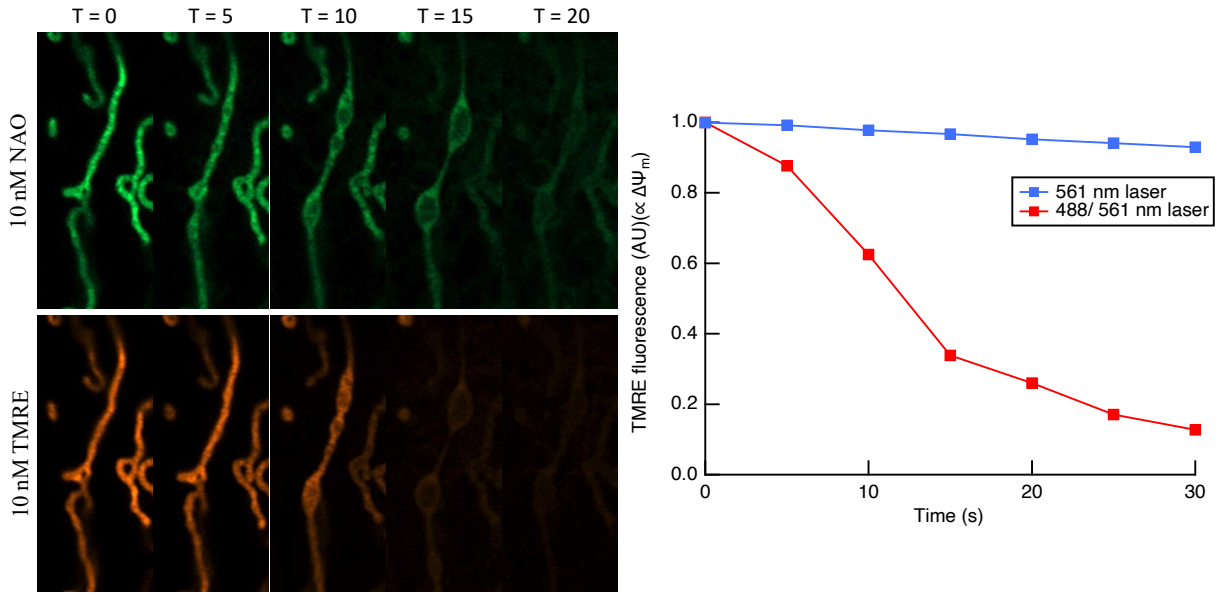

Figure 4-5. Mitochondria stained with 10 nM NAO and 10 nM TMRE also experienced a rapid loss of fluorescence, loss of membrane potential, and morphological deformation when excited with 488/561 nm lasers. When excited with a 561 nm laser only, we did not observe the fast drop in TMRE intensity.

In order to confirm at our concentrations that NAO H-dimer was not occurring, we examined the occurrence of green-to-red emission shift. In Figure 4-6, we used a 488 nm laser to excite mitochondria stained with NAO at concentrations of 10 nM, 100 nM, and 5 μM NAO. The emission ranges were set at 500-550 nm, 550-600 nm, 600-650 nm, and 650-700 nm. At concentrations of 10 nM and 100 nM, we observed the maximum emission in the expected 500-550 nm range, with unobservable emission in the 600-650 nm range associated with NAO H-dimers. However, at a concentration of 5 μM, a noticeable increase in emission intensity was observed in the 600-650 nm range. These results indicate that at the concentrations we used above, the dimerization-related mechanism is not responsible for the observed phototoxicity.

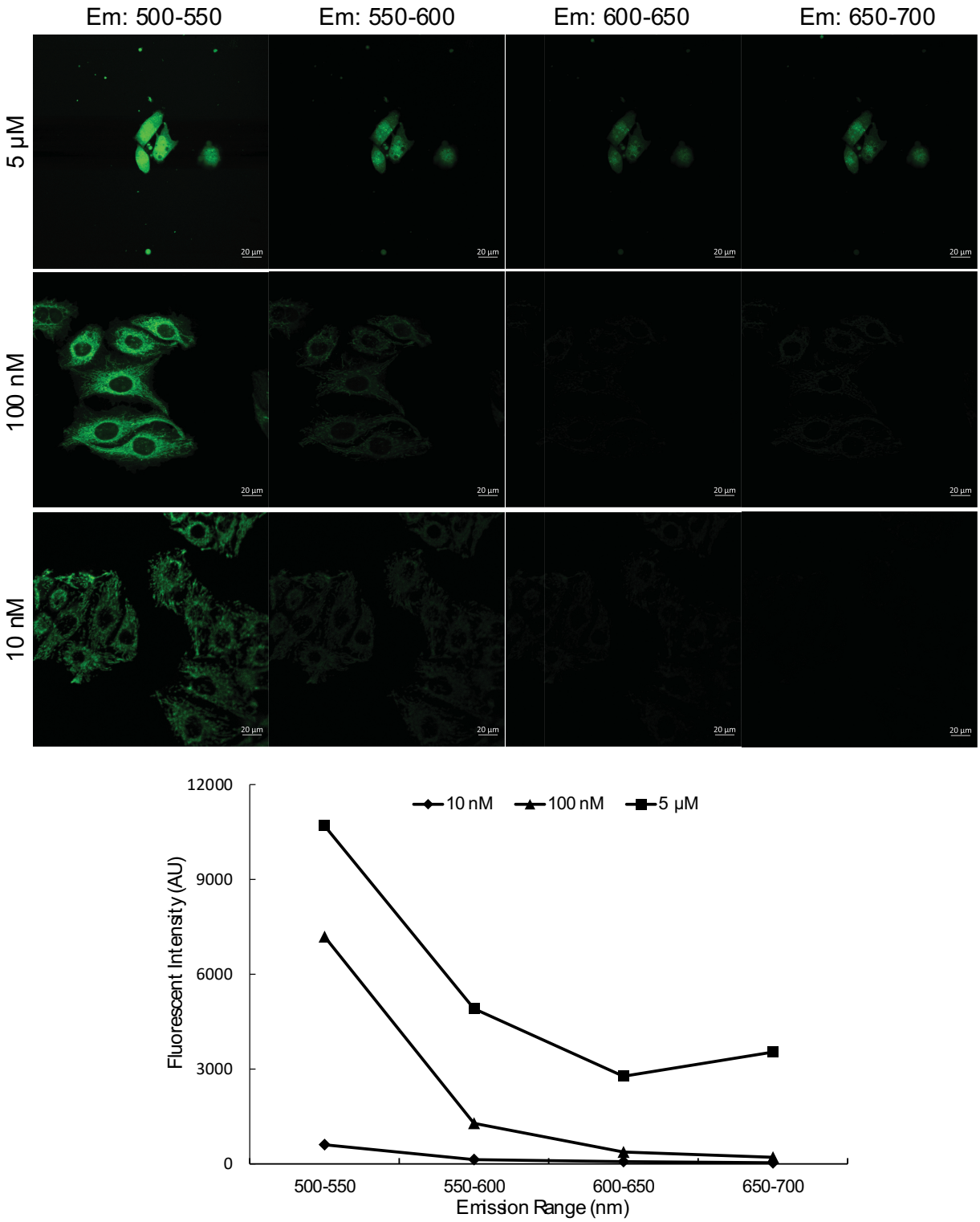

Figure 4-6. 5 µM, 100 nM, and 10 nM NAO excited with 488 nm laser and measure emissions in 500-550 nm, 550-600 nm, 600-650 nm, 650-700 nm emission ranges.

4.3.6 Investigating the mechanism of NAO phototoxicity: Verifying that toxicity is photo-induced

We also tested whether long-term incubation would trigger NAO cytotoxic effect at 100 nM concentration. We stained HEK293 cells with NAO and TMRE for 24 hours instead of the normal 15 minutes. On subsequent imaging, we found that the mitochondria were intact and the membrane potential sustained (Figure 4-7). Furthermore, once we excited the cells with a 488 nm laser, the rapid loss of fluorescence and the loss of mitochondrial membrane potential occurred. To further confirm that the phototoxicity of NAO required illumination, we used the laser scanning microscope to excite only a partial region of the cell and then imaged a wider region of the cell immediately. The red square in Figure 4-8 was exposed to 488 nm illumination, and only the mitochondria inside the excited area demonstrated photobleaching, swelling, and membrane potential depolarization. Therefore, we conclude that 100 nM of NAO is lower than the concentration threshold to cause cytotoxic effects to mitochondria and the observed rapid loss of membrane potential and morphological deformation are phototoxic effects induced by NAO and 488 nm laser excitation.

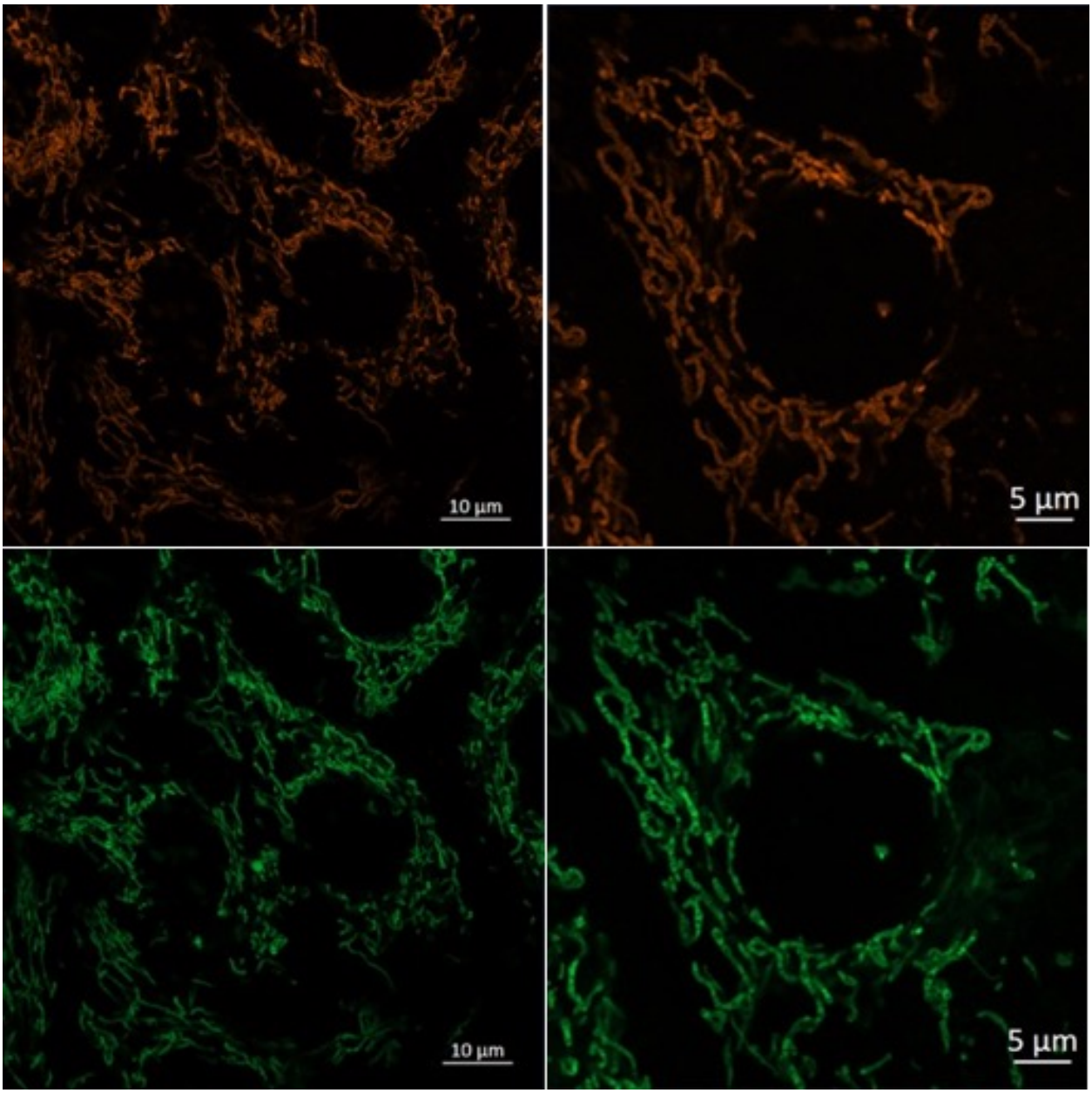

Figure 4-7. Assessing cytotoxic effect through prolonged incubation time of NAO dyes in HEK293 cells. The HEK293 cells were stained with 100 nM NAO and 10 nM TMRE for 24 hours before imaging. The mitochondria retained their tubular shapes and membrane potential. N = 3 independent experiments.

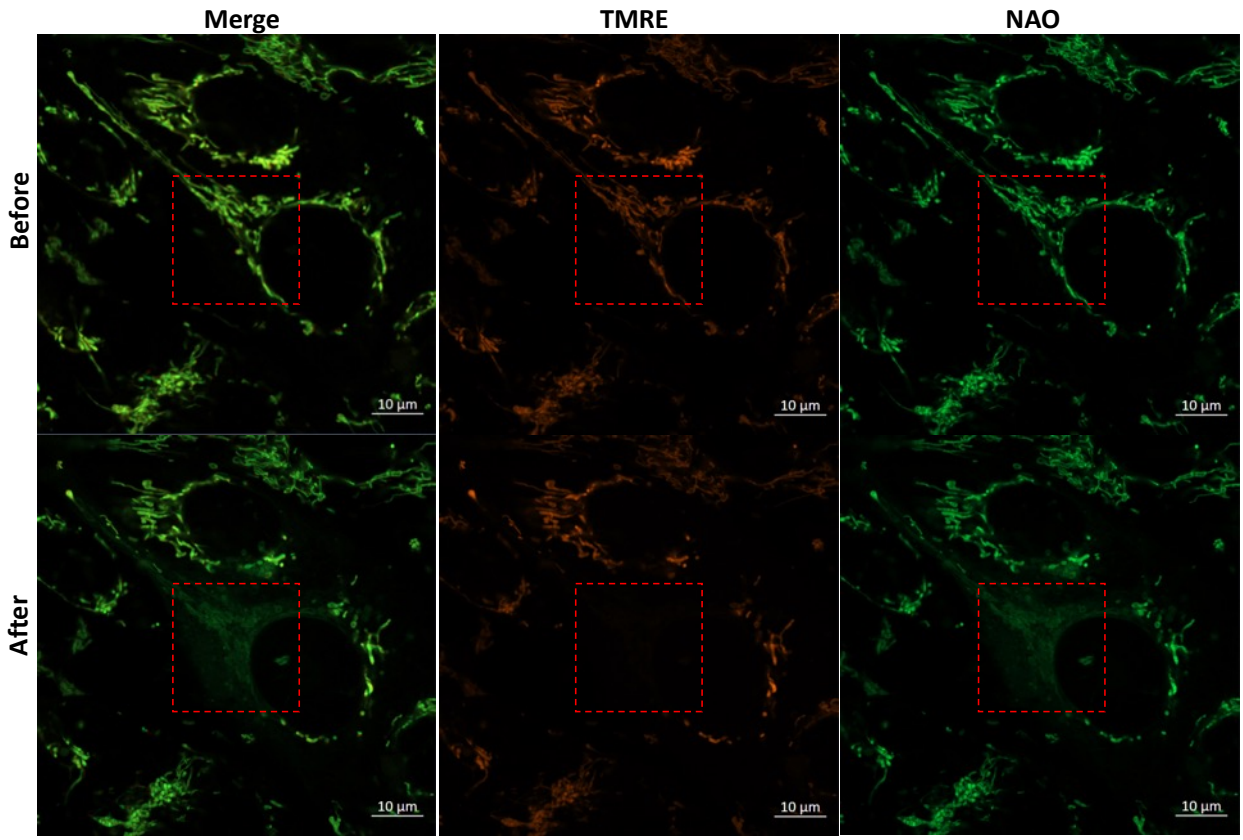

Figure 4-8. Phototoxicity was restricted in the illuminated region of the cell. Live cell mitochondria stained with NAO only showed structural swelling and lost mitochondrial membrane potential in the region exposed to the 488 nm illumination. N ≥ 3 independent experiments.

4.3.7 Mitochondria morphology analysis workflow

Figure 4-9 demonstrates the workflow for mitochondrial morphology analysis used in this manuscript. The raw images were deconvoluted using the Airyscan super-resolution processing function with optimal auto-filter setting. Following deconvolution, a Gaussian blur filter was used to denoise the image, and a top hat morphological transformation was performed to subtract non-mitochondria objects using ImageJ. Recognition of mitochondria was determined by thresholding the image based on the intensity profile of each image. An unsupervised K-means algorithm was used to determine the intensity threshold value to accurately distinguish true mitochondria pixels from background fluorescence. The threshold segmentation process is mainly extracting foreground based on gray value information, which is especially useful for the segmentation of images with a strong contrast between foreground objects (mitochondria) and background. In the time-lapse experiments, the photobleaching effect will result in worse recognition of mitochondria due to the dim fluorescence. Therefore, the mitochondria objects were manually inspected and compared to the original images before further morphology analysis using ImageJ.

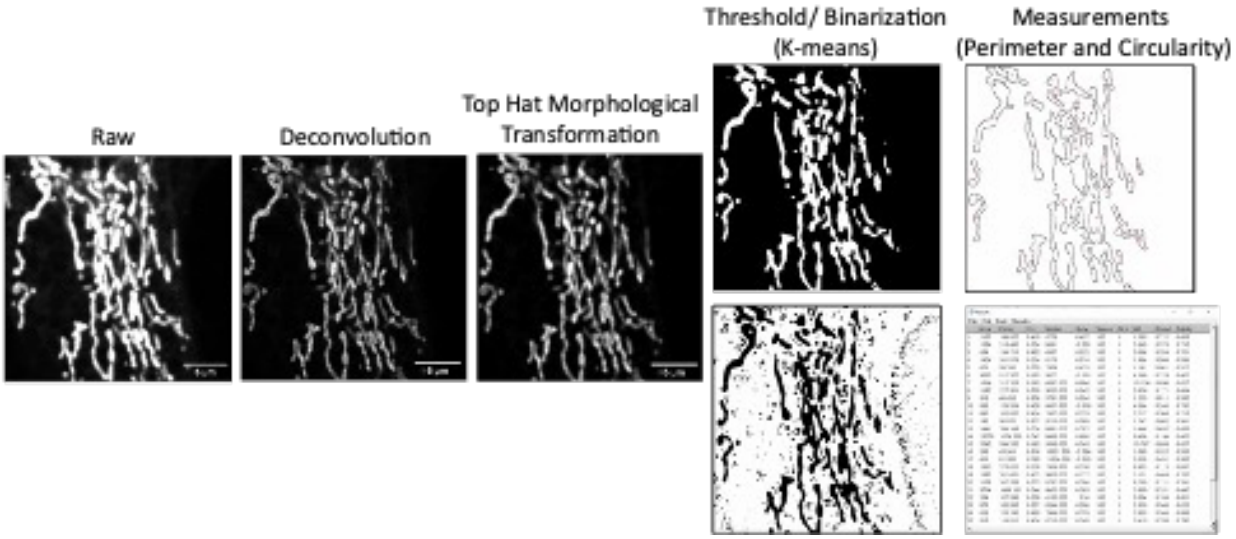

Figure 4-9. Quantification design for tracking mitochondrial morphology using NAO. The raw image was deconvoluted to get ultrafine structure information of mitochondria cristae. The top-hat morphological transformation subtracted out small, noisy, non-mitochondria objects. The unsupervised K-Means clustering algorithm separated the fluorescent intensity into two groups: mitochondria and non-mitochondria. The calculation of mitochondria perimeter and circularity were done by particle analysis application built-in ImageJ.

4.3.8 488/ 561nm laser excitation to NAO and MTG dyes comparison

Here we compare the differences of cells stained with 1. NAO and TMRE or 2. MTG and TMRE exposed to 488 nm and 561 nm lasers under the same illumination conditions.

Figure 4-10 shows the image results of mitochondria in HeLa, HEK293, and L6 cells stained with NAO and TMRE or MTG and TMRE, and excited by 488 nm and 561 nm laser under identical illumination and filter settings (0.5 % laser intensity and 3.54 μs dwell time per pixel) in time-lapse experiments. Cells stained with MTG showed a relatively higher resistance to photobleaching compared to those stained with NAO. Figure 4-11 shows the comparison of HeLa cells stained with TMRE and NAO or MTG excited by 488 nm and 561 nm laser under identical illumination and filter settings (0.5 % laser intensity and 3.54 μs dwell time per pixel) in time-lapse experiments. For HeLa cells stained with NAO and TMRE, both NAO and TMRE fluorescence disappeared (decreased by over 90 %) after 10 images were taken. On the other hand, HeLa cells stained with TMRE and MTG remained over 50 % intensities of both fluorescences after 30 images were taken. The calculation of fluorescence intensity in each HeLa cells group using the whole image is shown in Figure 4-10. An auto-threshold procedure (Otsu method) is first applied to segment out mitochondria from the background. Later, we averaged the whole values of the mitochondria pixels to get the averaged fluorescence intensity at each time point.

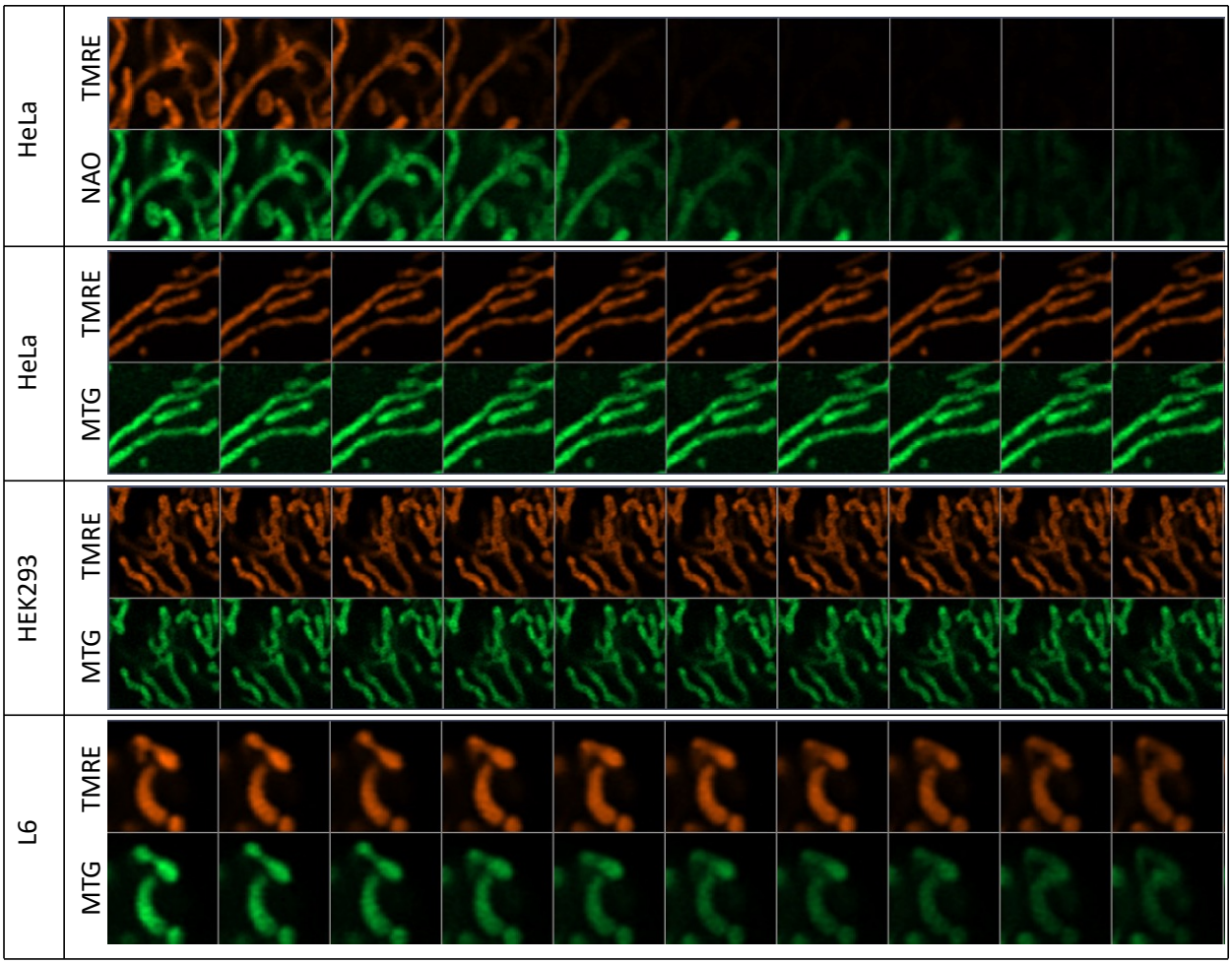

Figure 4-10. Time-lapse images of mitochondria in HeLa, HEK293, and L6 cells stained with NAO and TMRE or MTG and TMRE, and excited by 488 nm and 561 nm laser in time-lapse experiments (Identical illumination and filter settings).

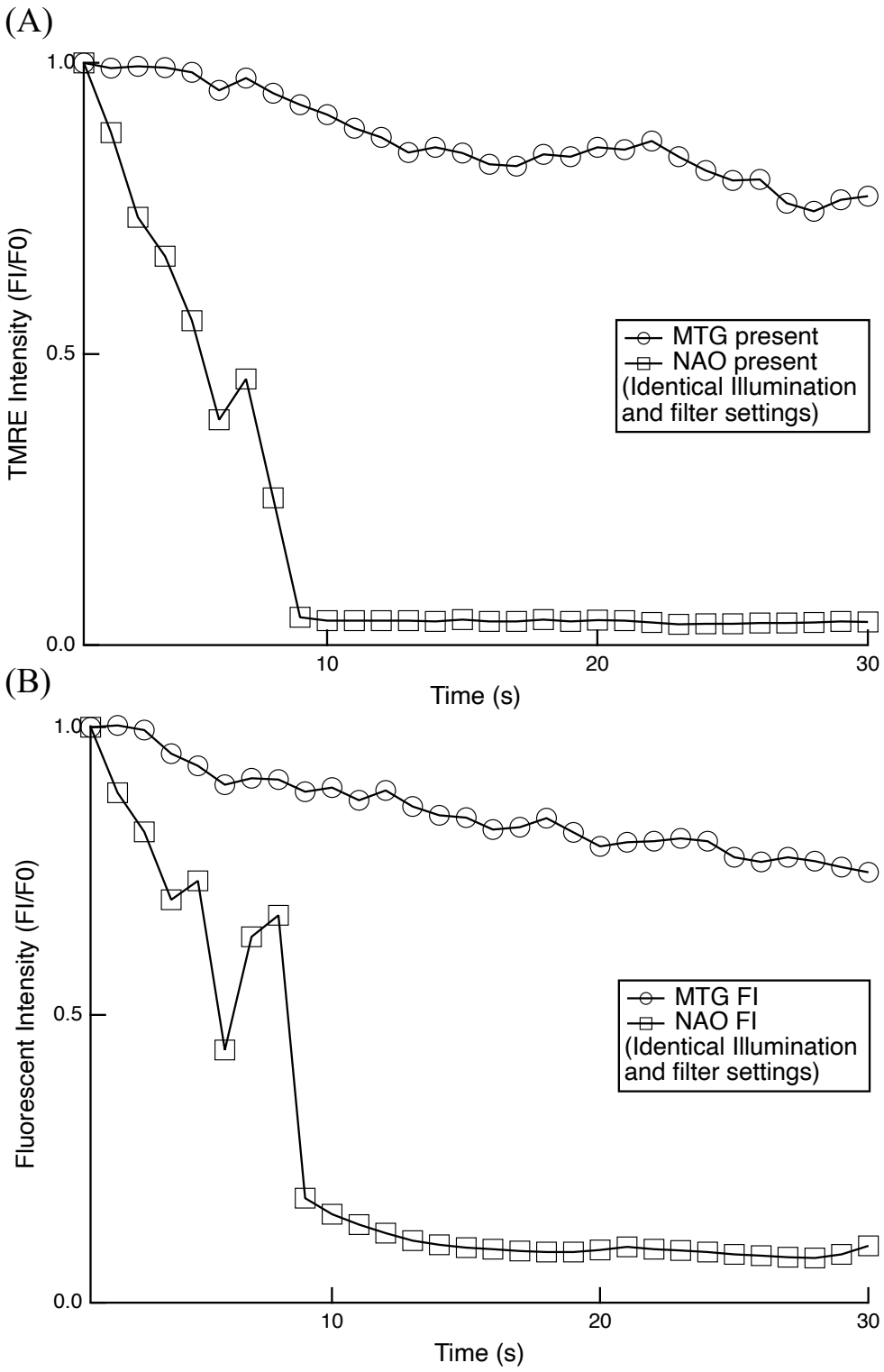

Figure 4-11. Results of HeLa cells stained with TMRE and NAO or MTG, and excited by 488nm and 561nm laser for time-lapse imaging (Identical illumination and filter settings). (A) The percentage drop of TMRE fluorescence intensity versus time when NAO or MTG is present. (B) The percentage drop of MTG or NAO fluorescence intensity versus time.

4.3.9 Statistic table for experiments

For all figures in the main text, we present the following tables of how many times that experiment was performed, and under what conditions. This demonstrates in detail the reproducibility of all the key findings of this paper. In particular, this clearly establishes that we are indeed seeing a common phenomenon, and not just an exception.

Conclusion for Figure 4-1: "NAO performed a rapid loss of fluorescence compared to MTG"

Conclusion for Figure 4-2and Figure 4-3: "NAO phototoxicity causes mitochondria ultrastructure to be destroyed and morphological changes from tubular shape to spherical shape."

Conclusion for Figure 4-4: "NAO phototoxicity is due to the exposure to 488 nm illumination, verified by loss of mitochondrial membrane potential."

Conclusion for Figure 4-6 and Figure 4-7: "Long-term incubation of NAO dye does not cause potential cytotoxicity and the phototoxic effect is restricted to the illuminated region of the cells."

In Table 4-1, we list all time-lapse experiments of cells stained with NAO and TMRE dyes and exposed to 488 nm and/or 561 nm illuminations. In a total of 15 experiments, 10 of the 15 times (66.7%) we observed mitochondria swell after exposed to the illuminations. 14 of the 15 times (93%, the only one time was imaged without TMRE channel, no data for membrane potential) we observed a rapid loss of membrane potential after exposed to the illuminations. The rows in grey are cells exposed to 561 nm illumination only. 4 of the 4 times (100%) the mitochondria demonstrate neither morphological changes nor loss of mitochondrial membrane potential, which verified the NAO phototoxicity is due to the exposure to 488 nm illumination.

In Table 4-2, we list all time-lapse experiments of cells stained with MTG and TMRE dyes and exposed to 488 nm and/or 561 nm illuminations. In total 5 experiments, 5 of the 5 times (100%) we did not observe mitochondria swell after being exposed to the illuminations. The rapid loss of membrane potential was also not observed after exposed to the illuminations.

In Table 4-3, we list all experiments with long-term staining of cells with NAO and TMRE dyes. In total 3 experiments, 3 of the 3 times we observed neither the swelling of mitochondria nor the loss of membrane potential after 24 hours of incubation.

Record for time-lapse imaging with NAO+TMREdye											
Date	Cell used (Passage #)	Lables	Staining condition	Laser settings	Objective	Detection [nm]	Pixel time [us]	Pixel size [nm]	FOV [um]	Mitochondria swelling?	Rapid lost of membrane potential?
100121(001~003)	HeLa (P9)	TMRE NAO	10 nM; 15 min; DMEM 100 nM; 15 min; DMEM	λex561nm (0.3%) λex488nm (0.3%)	63x	561-700 488-560	5.31	42	398x398	Y	Y
100521(003,009)	HeLa (P10)	TMRE NAO	10 nM; 15 min; DMEM 100 nM; 15 min; DMEM	λex561nm (0.1%) λex488nm (0.1%)	63x	561-700 488-560	10.94	43	362x362	Y	Y
100921(009~011)	HeLa (P10)	TMRE NAO	10 nM; 15 min; DMEM 100 nM; 15 min; DMEM	λex561nm (0.2%) λex488nm (0.1%)	63x	561-700 488-560	3.55	43	12.68x12.68	Y	Y
101121(007~009)	HeLa (P11)	TMRE NAO	10 nM; 15 min; DMEM 100 nM; 15 min; DMEM	λex561nm (0.2%) λex488nm (0.2%)	63x	561-700 488-560	1.33	42	16.90x16.90	Y	Y
101321(004)	HeLa (P11)	TMRE NAO	10 nM; 15 min; DMEM 100 nM; 15 min; DMEM	λex561nm (0.3%) λex488nm (1.0%)	63x	561-700 488-560	17.79	43	10.14x10.14	Y	Y
101721(038)	HeLa (P13)	TMRE NAO	10 nM; 15 min; DMEM 100 nM; 15 min; DMEM	λex561nm (0.1%) λex488nm (0.05%)	63x	561-700 488-560	4.45	43	10.14x10.14	Y	Y
120821(012~014)	HeLa (P11)	TMRE NAO	10 nM; 15 min; DMEM 100 nM; 15 min; DMEM	λex561nm (0.3%)	63x	561-700	3.76	49	8.97x8.97	N	N
120921(003 004)	HeLa (P12)	TMRE NAO	10 nM; 15 min; DMEM 100 nM; 15 min; DMEM	λex561nm (0.5%)	63x	561-700	2.04	49	25.35x25.35	N	N
122121	HeLa (P14)	TMRE NAO	10 nM; 15 min; DMEM 100 nM; 15 min; DMEM	λex561nm (0.3%)	63x	561-700	3.76	49	8.97x8.97	N	N
021222(013~015)	HeLa (P5)	TMRE NAO	10 nM; 15 min; DMEM 100 nM; 15 min; DMEM	λex561nm (0.5%) λex488nm (0.3%)	63x	561-700 488-560	0.85	43	16.90x16.90	N	Y
050422(004)	HeLa (P10)	TMRE NAO	10 nM; 15 min; DMEM 100 nM; 15 min; DMEM	λex561nm (0.5%) λex488nm (0.5%)	63x	561-700 488-560	1.43	42	4.06x4.06	N	Y
050422(006)	HeLa (P10)	TMRE NAO	10 nM; 15 min; DMEM 100 nM; 15 min; DMEM	λex561nm (0.5%)	63x	561-700	1.65	49	3.9x3.9	N	N
050422(206)	L6 (P8)	TMRE NAO	10 nM; 15 min; DMEM 100 nM; 15 min; DMEM	λex561nm (0.5%) λex488nm (2.0%)	63x	561-700 488-560	1.79	42	4.06x4.06	N	Y
050422(211)	L6 (P8)	TMRE NAO	10 nM; 15 min; DMEM 100 nM; 15 min; DMEM	λex561nm (0.5%) λex488nm (2.0%)	63x	561-700 488-560	1.79	42	4.06x4.06	Y	Y
030823(104~106)	HeLa (P8)	TMRE NAO	10 nM; 15 min; DMEM 100 nM; 15 min; DMEM	λex561nm (1.0%) λex488nm (1.0%)	63x	561-700 488-560	1.15	43	77.01x78.01	N	Y
031723(108~110)	HeLa (P8)	TMRE NAO	10 nM; 15 min; DMEM 100 nM; 15 min; DMEM	λex561nm (1.0%) λex488nm (1.0%)	63x	561-700 488-560	0.98	43	15.88x15.88	N	Y
040523(108~110)	HeLa (P8)	TMRE NAO	10 nM; 15 min; DMEM 100 nM; 15 min; DMEM	λex561nm (1.0%) λex488nm (1.0%)	63x	561-700 488-560	0.98	43	15.88x15.88	N	Y
041123(310~312)	HEK293 (P10)	TMRE NAO	10 nM; 15 min; DMEM 100 nM; 15 min; DMEM	λex561nm (0.3%) λex488nm (0.3%)	63x	561-700 488-560	0.88	43	21.09x21.09	Y	Y

Table 4-1. Record and statistic table for experiments having cells stained with NAO and TMRE, and exposed to 488 nm and/or 561 nm illuminations.

Record for time-lapse imaging with MTG+TMRE dye excited by 488 nm and 561 nm illuminations											
Date	Cell used (Passage #)	Lables	Staining condition	Laser settings	Objective	Detection [nm]	Pixel time [us]	Pixel size [nm]	FOV [um]	Mitochondria swelling?	Rapid lost of membrane potential?
121021001	HeLa (P11)	TMRE MTG	10 nM; 15 min; DMEM 100 nM; 15 min; DMEM	λex561nm (0.5%) λex488nm (0.5%)	63x	561-700 488-560	3.54	43	25.35x25.35	N	N
121021004	HeLa (P11)	TMRE MTG	10 nM; 15 min; DMEM 100 nM; 15 min; DMEM	λex561nm (0.5%) λex488nm (1.0%)	63x	561-700 488-560	3.54	43	25.35x25.35	N	N
121321009	HeLa (P12)	TMRE MTG	10 nM; 15 min; DMEM 100 nM; 15 min; DMEM	λex561nm (0.1%) λex488nm (0.1%)	63x	561-700 488-560	3.55	43	11.66x11.66	N	N
121721018	HeLa (P8)	TMRE MTG	10 nM; 15 min; DMEM 100 nM; 15 min; DMEM	λex561nm (0.5%) λex488nm (0.1%)	63x	561-700 488-560	3.55	43	11.66x11.66	N	N
051022(009)	HeLa (P11)	TMRE MTG	10 nM; 15 min; DMEM 100 nM; 15 min; DMEM	λex561nm (1.0%) λex488nm (1.0%)	63x	561-700 488-560	2.63	41	4.34x4.34	N	N

Table 4-2. Record and statistic table for experiments having cells stained with MTG and TMRE, and exposed to 488 nm and/or 561 nm illuminations.

Record for 24-hours incubation with NAO+TMRE dye											
Date	Cell used (Passage #)	Lables	Staining condition	Laser settings	Objective	Detection [nm]	Pixel time [us]	Pixel size [nm]	FOV [um]	Mitochondria swelling?	Rapid lost of membrane potential?
042523(004)	HEK293 (P13)	TMRE NAO	10 nM; 15 min; DMEM 100 nM; 15 min; DMEM	λex561nm (1.0%) λex488nm (1.0%)	63x	561-700 488-560	1.15	74	245.73x245.73	N	N
042523(013)	HEK293 (P13)	TMRE NAO	10 nM; 15 min; DMEM 100 nM; 15 min; DMEM	λex561nm (1.0%) λex488nm (1.0%)	63x	561-700 488-560	1.15	43	78.01x78.01	N	N
042523(040)	HEK293 (P13)	TMRE NAO	10 nM; 15 min; DMEM 100 nM; 15 min; DMEM	λex561nm (1.0%) λex488nm (1.0%)	63x	561-700 488-560	0.93	43	48.19x48.19	N	N

Table 4-3. Record and statistic table for experiments of cells having long-term staining with NAO and TMRE.

4.4 Conclusion

We have identified two useful parameters for evaluating the phototoxicity associated with the photobleaching of mitochondrially-targeted fluorescent dyes: conversion of tubular mitochondrial to spherical ones, and the loss of the mitochondrial membrane potential when the cell is co-stained with TMRE. Using these parameters, we have found that NAO-stained mitochondria illuminated at 488 nm undergo rapid loss of membrane potential and conversion from elongated to spherical mitochondria, while this is not the case when the cells are stained with MTG and illuminated at 488 nm. We also conclude that this effect is not related to concentration-induced cytotoxicity by NAO. It is currently unclear why NAO plus 488 nm illumination is so toxic but one possibility is that some derived product ruptures the mitochondrial inner membrane since TMRE fluorescence is lost with the same kinetics as the loss of the mitochondrial morphological integrity. In HeLa, HEK293, and L6 cells, NAO lost over 80 % of its fluorescence while MTG lost only 30% of its fluorescence in the first 50 seconds of illumination with the same settings. NAO-stained mitochondria underwent a morphological change with the average circularity (a measure of phototoxicity) increasing from 0.4 to 0.7 within 100 seconds of illumination. NAO-stained mitochondria lost their membrane potential rapidly after being exposed to 488 nm illumination (used to pump NAO), but this phenomenon was not observed when using 561 nm illumination (used to pump TMRE). Prolonged incubation with NAO demonstrated little or no toxicity to mitochondria, indicating that phototoxicity is the dominant toxicity mechanism of NAO.

Chapter 5. FUTURE RESEARCH DIRECTIONS

In this thesis, we demonstrate the viability of quantitatively studying mitochondria electrophysiology and ultrastructure in different metabolic states using super-resolution microscopy. Future research could follow our methodology and expand to the following topics:

5.1 Simultaneous measurement of single mitochondria oxygen consumption and membrane potential change.

Combining super-resolution microscopy and fluorescent lipophilic cation dyes provides a semi-quantitative analysis of membrane potential in different respiratory states. However, the interpretation could be misleading if: 1) the cations do not all fluorescence when binding to the membrane, and 2) the mitochondria are during state transitions and without other parameters to indicate the stages. To overcome this problem, one can consider measuring the oxygen consumption and the lipophilic cation fluorescence simultaneously to quantitatively determine the portion of non-fluorescence cations on the membrane. By doing this, one would need to come up with a device design to properly analyze the oxygen consumption in the airtight chamber with single mitochondria inside. This could also be used to study the heterogeneity of mitochondria in different cell types or within the same cell.

5.2 Cristae remodeling during apoptosis

The release of cytochrome c (CytC) into the cytosol is one of the key events in apoptosis. During mitochondrial outer membrane permeabilization (MOMP), the outer membrane becomes permeable with pores allowing high-molecular-weight proteins such as CytC to spill into the cytosol. On closer inspection, the release of CytC following MOMP poses a conceptual problem, as the stores of CytC has shown over 15 years to predominately reside in the regions inside the cristae, and not the rest of the intermembrane space. Therefore, if MOMP allows the release of CytC, it must be free to pass through the cristae junctions. However, if this were true, the CytC would not be concentrated in the cristae. Therefore, for the CytC to be released (a precondition for apoptosis), one hypothesis is that cristae remodeling must occur to open the junctions. A couple of studies[172–176] have demonstrated cristae remodeling during apoptosis, however, some observes the cristae junction transforms into a tight and condensed conformation while others observes the junction to transform into a widen and orthodox size. Why is there such a discrepancy between results? One of the most important factors is that TEM studies provide only a snapshot of a dynamic process. Artifacts during the imaging process can't be corrected with one single filming. The second factor is that the fixation and freezing processes may attribute errors for TEM imaging[176], thus masking the effect to be imaged or significantly perturbing the frozen state from the in vivo, live state that is desired to be studied.

How exactly the cristae remodeling is triggered during apoptosis remains unknown. Recently, a more accepted model is that optic atrophy (OPA1) holding the cristae together and controlling the release of CytC. Humans have eight different isoforms of OPA1, including long and short forms (L-OPA1 and S-OPA1). These are present in nearly equimolar forms under basal conditions[177]. The L form can be cleaved to the S form by the mitochondrial zinc metalloprotease (OMA1) when the mitochondrial membrane potential is low[178]. Jiang[179] has

investigated several proteases that have been shown to cleave OPA1 under different stress conditions and found that OMA1 is critically important for apoptosis inducing by Bim or tBid expression, whereas knockdown of other mitochondrial proteases has little effect. OMA1 is normally degraded by proteolysis, but in low membrane potential situations, OMA1 is stabilized and survives long enough to cleave L-OPA1 to S-OPA1. Thus, OPA pools are determined by the bioenergetic parameter ΔΨm, the mitochondrial membrane potential. This provides an important clue that relates a metabolic parameter to a protein involved in the regulation of mitochondrial ultrastructure, but the detailed mechanism of this relationship is not clear yet. One potential guess is when MOMP occurs, part of CytC (~15%) between the inner membrane and outer membrane will be released first and causes a slightly decrease in membrane potential, which triggers the OMA1 activation and leads to OPA1 cleavage. Figure 5-1 shows the cartoon of the hypothesis of OPA1 cleavage.

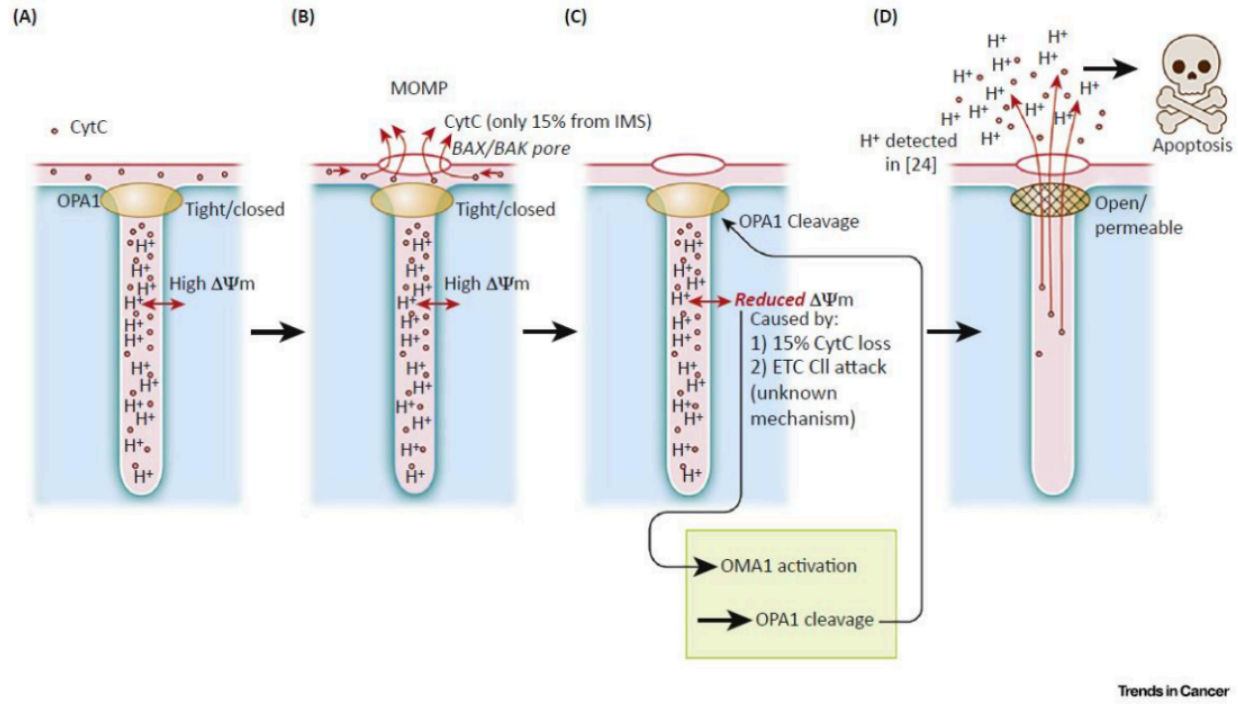

Figure 5-1. A cartoon only of MOMP and cristae remodeling/membrane depolarization.

Outstanding questions are:

1. What are the energy requirements of cristae membrane dynamics? [85,86]
2. How are cristae dynamics affected during apoptosis?
3. How do cristae dynamics affect the nanoscale organization of redox nanodomains and redox signaling?
4. What is the role of cristae architecture in mitochondrial bioenergetics? [86]

5.3 Monitoring pH value and local temperature inside cristae via quantum sensors

As discussed in Chapter 3, the electric fields inside the cristae are intense. The huge imbalance of protons free in the matrix and on the surface of the mitochondrial inner membrane must affect the electrostatics inside the cristae to create immense electric fields. This would also have a huge potential to impact the protein complexes in the ETC. A new model, not based on bulk, continuum distributions of charge and pH, which takes into account the immense electric fields and their impact on the ETC performance under different metabolic conditions is needed. Instead of integrating additional sensors, one could try introducing fluorescent nanodiamonds (FNDs) as a substitute method to monitor mitochondria metabolic activities. FNDs have outstanding photostability and biocompatibility which makes them a promising tool for bioimaging. Nanodiamonds used as sensors to study the pH and temperature change within cristae could be an interesting topic to understand the electrochemical changes under mitochondrial metabolism change and apoptosis.

REFERENCES

(1) Liao, P.; Bergamini, C.; Fato, R.; Pon, L. A.; Pallotti, F. Isolation of Mitochondria from Cells and Tissues. *Methods Cell Biol* **2020**, *155*, 3–31. https://doi.org/10.1016/bs.mcb.2019.10.002.

(2) Wallace, D. C.; Fan, W.; Procaccio, V. Mitochondrial Energetics and Therapeutics. *Annu Rev Pathol* **2010**, *5*, 297–348. https://doi.org/10.1146/annurev.pathol.4.110807.092314.

(3) Wallace, D. C. Mitochondrial DNA Mutations in Disease and Aging. *Environ Mol Mutagen* **2010**, *51* (5), 440–450. https://doi.org/10.1002/em.20586.

(4) Wallace, D. C. Mitochondrial Diseases in Man and Mouse. *Science* **1999**, *283* (5407), 1482–1488. https://doi.org/10.1126/science.283.5407.1482.

(5) Wallace, D. C. Bioenergetic Origins of Complexity and Disease. *Cold Spring Harb Symp Quant Biol* **2011**, *76* (0), 1–16. https://doi.org/10.1101/sqb.2011.76.010462.

(6) Wallace, D. C. Mitochondria and Cancer. *Nat Rev Cancer* **2012**, *12* (10), 685–698. https://doi.org/10.1038/nrc3365.

(7) Nicholls, D. G.; Ferguson, S. J. *Bioenergetics*, 4th ed.; Academic Press, San Diego, 2013.

(8) Gnaiger, E. *Mitochondrial Pathways and Respiratory Control. An Introduction to OXPHOS Analysis. Mitochondrial Physiology Network 17.18*; OROBOROS MiPNet Publications, Innsbruck, 2012.

(9) Wallace, D. C. A Mitochondrial Paradigm of Metabolic and Degenerative Diseases, Aging, and Cancer: A Dawn for Evolutionary Medicine. *Annu Rev Genet* **2005**, *39* (5), 359–407. https://doi.org/10.1146/annurev.genet.39.110304.095751.

(10) Hanahan, D.; Weinberg, R. A. Hallmarks of Cancer: The Next Generation. *Cell* **2011**, *144* (5), 646–674. https://doi.org/10.1016/j.cell.2011.02.013.

(11) Wallace, D. C. Bioenergetics, the Origins of Complexity, and the Ascent of Man. *Proceedings of the National Academy of Sciences* **2010**, *107* (supplement_2), 8947–8953. https://doi.org/10.1073/pnas.0914635107.

(12) Wallace, D. C.; Lott, M. T.; Procaccio, V. Mitochondrial Genes in Degenerative Diseases, Cancer and Aging. In *Emery and Rimoin's Principles and Practice of Medical Genetics*; Rimoin, D. L., Connor, J. M., Pyeritz, R. E., Korf, B. R., Eds.; Churchill Livingstone Elsevier: Philadelphia, PA, 2007; Vol. Volume 1, pp 194–298.

(13) King, A.; Selak, M. A.; Gottlieb, E. Succinate Dehydrogenase and Fumarate Hydratase: Linking Mitochondrial Dysfunction and Cancer. *Oncogene* **2006**, *25* (34), 4675–4682. https://doi.org/10.1038/sj.onc.1209594.

(14) Pasini, B.; McWhinney, S. R.; Bei, T.; Matyakhina, L.; Stergiopoulos, S.; Muchow, M.; Boikos, S. A.; Ferrando, B.; Pacak, K.; Assie, G.; Baudin, E.; Chompret, A.; Ellison, J. W.; Briere, J.-J.; Rustin, P.; Gimenez-Roqueplo, A.-P.; Eng, C.; Carney, J. A.; Stratakis, C. A. Clinical and Molecular Genetics of Patients with the Carney-Stratakis Syndrome and Germline Mutations of the Genes Coding for

the Succinate Dehydrogenase Subunits SDHB, SDHC, and SDHD. *Eur J Hum Genet* **2008**, *16* (1), 79–88. https://doi.org/10.1038/sj.ejhg.5201904.

(15) Bayley, J.-P.; Devilee, P. Warburg Tumours and the Mechanisms of Mitochondrial Tumour Suppressor Genes. Barking up the Right Tree? *Curr Opin Genet Dev* **2010**, *20* (3), 324–329. https://doi.org/10.1016/j.gde.2010.02.008.

(16) Bardella, C.; Pollard, P. J.; Tomlinson, I. SDH Mutations in Cancer. *Biochim Biophys Acta* **2011**, *1807* (11), 1432–1443. https://doi.org/10.1016/j.bbabio.2011.07.003.

(17) Vanharanta, S.; Buchta, M.; McWhinney, S. R.; Virta, S. K.; Peçzkowska, M.; Morrison, C. D.; Lehtonen, R.; Januszewicz, A.; Järvinen, H.; Juhola, M.; Mecklin, J.-P.; Pukkala, E.; Herva, R.; Kiuru, M.; Nupponen, N. N.; Aaltonen, L. A.; Neumann, H. P. H.; Eng, C. Early-Onset Renal Cell Carcinoma as a Novel Extraparaganglial Component of SDHB-Associated Heritable Paraganglioma. *Am J Hum Genet* **2004**, *74* (1), 153–159. https://doi.org/10.1086/381054.

(18) Gottlieb, E.; Tomlinson, I. P. M. Mitochondrial Tumour Suppressors: A Genetic and Biochemical Update. *Nat Rev Cancer* **2005**, *5* (11), 857–866. https://doi.org/10.1038/nrc1737.

(19) Frezza, C.; Pollard, P. J.; Gottlieb, E. Inborn and Acquired Metabolic Defects in Cancer. *J Mol Med (Berl)* **2011**, *89* (3), 213–220. https://doi.org/10.1007/s00109-011-0728-4.

(20) Frezza, C.; Gottlieb, E. Mitochondria in Cancer: Not Just Innocent Bystanders. *Semin Cancer Biol* **2009**, *19* (1), 4–11. https://doi.org/10.1016/j.semcancer.2008.11.008.

(21) Semenza, G. L. A Return to Cancer Metabolism. *J Mol Med (Berl)* **2011**, *89* (3), 203–204. https://doi.org/10.1007/s00109-011-0733-7.

(22) Brand, M. D.; Nicholls, D. G. Assessing Mitochondrial Dysfunction in Cells. *Biochemical Journal* **2011**, *435* (2), 297–312. https://doi.org/10.1042/BJ20110162.

(23) Trounce, I. A.; Kim, Y. L.; Jun, A. S.; Wallace, D. C. Assessment of Mitochondrial Oxidative Phosphorylation in Patient Muscle Biopsies, Lymphoblasts, and Transmitochondrial Cell Lines. *Methods Enzymol* **1996**, *264* (1992), 484–509. https://doi.org/10.1016/s0076-6879(96)64044-0.

(24) Trounce, I.; Neill, S.; Wallace, D. C. Cytoplasmic Transfer of the MtDNA Nt 8993 T-->G (ATP6) Point Mutation Associated with Leigh Syndrome into MtDNA-Less Cells Demonstrates Cosegregation with a Decrease in State III Respiration and ADP/O Ratio. *Proc Natl Acad Sci U S A* **1994**, *91* (18), 8334–8338. https://doi.org/10.1073/pnas.91.18.8334.

(25) Frezza, C.; Cipolat, S.; Scorrano, L. Organelle Isolation: Functional Mitochondria from Mouse Liver, Muscle and Cultured Fibroblasts. *Nat Protoc* **2007**, *2* (2), 287–295. https://doi.org/10.1038/nprot.2006.478.

(26) Gellerich, F. N.; Mayr, J. A.; Reuter, S.; Sperl, W.; Zierz, S. The Problem of Interlab Variation in Methods for Mitochondrial Disease Diagnosis: Enzymatic Measurement of Respiratory Chain Complexes. *Mitochondrion* **2004**, *4* (5–6), 427–439. https://doi.org/10.1016/j.mito.2004.07.007.

(27) Di Carlo, D.; Irimia, D.; Tompkins, R. G.; Toner, M. Continuous Inertial Focusing, Ordering, and Separation of Particles in Microchannels. *Proceedings of the National Academy of Sciences* **2007**, *104* (48), 18892–18897. https://doi.org/10.1073/pnas.0704958104.

(28) Di Carlo, D. Inertial Microfluidics. *Lab Chip* **2009**, *9* (21), 3038–3046. https://doi.org/10.1039/b912547g.

(29) Tesauro, C.; Ferrando, B.; Ma, X.; Jepsen, M. L.; Ivarsen, A. K. R.; Frøhlich, R.; Stevnsner, T.; Knudsen, B. R.; Ho, Y. P. Isolation of Functional Mitochondria by Inertial Microfluidics-a New Method to Sort Intracellular Organelles from a Small Scale Biological Sample. *RSC Adv* **2017**, *7* (38), 23735–23741. https://doi.org/10.1039/c7ra03384b.

(30) Choi, K.; Ryu, H.; Siddle, K. J.; Piantadosi, A.; Freimark, L.; Park, D. J.; Sabeti, P.; Han, J. Negative Selection by Spiral Inertial Microfluidics Improves Viral Recovery and Sequencing from Blood. *Anal Chem* **2018**, *90* (7), 4657–4662. https://doi.org/10.1021/acs.analchem.7b05200.

(31) Abdulla, A.; Liu, W.; Gholamipour-Shirazi, A.; Sun, J.; Ding, X. High-Throughput Isolation of Circulating Tumor Cells Using Cascaded Inertial Focusing Microfluidic Channel. *Anal Chem* **2018**, *90* (7), 4397–4405. https://doi.org/10.1021/acs.analchem.7b04210.

(32) Zhu, S.; Wu, D.; Han, Y.; Wang, C.; Xiang, N.; Ni, Z. Inertial Microfluidic Cube for Automatic and Fast Extraction of White Blood Cells from Whole Blood. *Lab Chip* **2020**, *20* (2), 244–252. https://doi.org/10.1039/c9lc00942f.

(33) Razavi Bazaz, S.; Rouhi, O.; Raoufi, M. A.; Ejeian, F.; Asadnia, M.; Jin, D.; Ebrahimi Warkiani, M. 3D Printing of Inertial Microfluidic Devices. *Sci Rep* **2020**, *10* (1), 1–14. https://doi.org/10.1038/s41598-020-62569-9.

(34) Zhang, T.; Hong, Z. Y.; Tang, S. Y.; Li, W.; Inglis, D. W.; Hosokawa, Y.; Yalikun, Y.; Li, M. Focusing of Sub-Micrometer Particles in Microfluidic Devices. *Lab Chip* **2020**, *20* (1), 35–53. https://doi.org/10.1039/c9lc00785g.

(35) Kalyan, S.; Torabi, C.; Khoo, H.; Sung, H. W.; Choi, S. E.; Wang, W.; Treutler, B.; Kim, D.; Hur, S. C. Inertial Microfluidics Enabling Clinical Research. *Micromachines (Basel)* **2021**, *12* (3), 1–43. https://doi.org/10.3390/mi12030257.

(36) Marc, P. J.; Sims, C. E.; Bachman, M.; Li, G. P.; Allbritton, N. L. Fast-Lysis Cell Traps for Chemical Cytometry. *Lab Chip* **2008**, *8* (5), 710–716. https://doi.org/10.1039/b719301g.

(37) Zand, K.; Pham, T.; Davila, A.; Wallace, D. C.; Burke, P. J. Nanofluidic Platform for Single Mitochondria Analysis Using Fluorescence Microscopy. *Anal Chem* **2013**, *85* (12), 6018–6025. https://doi.org/10.1021/ac4010088.

(38) Zand, K.; Pham, T. D. A.; Li, J.; Zhou, W.; Wallace, D. C.; Burke, P. J. Resistive Flow Sensing of Vital Mitochondria with Nanoelectrodes. *Mitochondrion* **2017**, *37*, 8–16. https://doi.org/10.1016/j.mito.2017.06.003.

(39) Pham, T. D.; Pham, P. Q.; Li, J.; Letai, A. G.; Wallace, D. C.; Burke, P. J. Cristae Remodeling Causes Acidification Detected by Integrated Graphene Sensor during Mitochondrial Outer Membrane Permeabilization. *Sci Rep* **2016**, *6* (1), 35907. https://doi.org/10.1038/srep35907.

(40) Pham, T.; Wallace, D.; Burke, P. Microchambers with Solid-State Phosphorescent Sensor for Measuring Single Mitochondrial Respiration. *Sensors* **2016**, *16* (7), 1065. https://doi.org/10.3390/s16071065.

(41) Friedman, A. a.; Letai, A.; Fisher, D. E.; Flaherty, K. T. Precision Medicine for Cancer with Next-Generation Functional Diagnostics. *Nat Rev Cancer* **2015**, *15* (12), 747–756. https://doi.org/10.1038/nrc4015.

(42) Letai, A.; Bhola, P.; Welm, A. L. Functional Precision Oncology: Testing Tumors with Drugs to Identify Vulnerabilities and Novel Combinations. *Cancer Cell* **2022**, *40* (1), 26–35. https://doi.org/10.1016/j.ccell.2021.12.004.

(43) Letai, A. Functional Precision Medicine: Putting Drugs on Patient Cancer Cells and Seeing What Happens. *Cancer Discov* **2022**, *12* (2), 290–292. https://doi.org/10.1158/2159-8290.CD-21-1498.

(44) Zhang, J.; Yan, S.; Yuan, D.; Alici, G.; Nguyen, N. T.; Ebrahimi Warkiani, M.; Li, W. Fundamentals and Applications of Inertial Microfluidics: A Review. *Lab Chip* **2016**, *16* (1), 10–34. https://doi.org/10.1039/c5lc01159k.

(45) Berger SA, Talbot L, Y. L. Flow in Curved Pipes. **1983**, 461–512. https://doi.org/10.1146/annurev.fl.15.010183.002333.

(46) Kuntaegowdanahalli, S. S.; Bhagat, A. A. S.; Kumar, G.; Papautsky, I. Inertial Microfluidics for Continuous Particle Separation in Spiral Microchannels. *Lab Chip* **2009**, *9* (20), 2973–2980. https://doi.org/10.1039/B908271A.

(47) Liu, N.; Petchakup, C.; Tay, H. M.; Li, K. H. H.; Hou, H. W. Spiral Inertial Microfluidics for Cell Separation and Biomedical Applications; 2019; pp 99–150. https://doi.org/10.1007/978-981-13-6229-3_5.

(48) Xu, X.; Huang, X.; Sun, J.; Wang, R.; Yao, J. Recent Progress of Inertial Microfluidic-Based Cell Separation. *Analyst* **2021**, *146*, 7070–7086. https://doi.org/10.1039/d1an01160j.

(49) Bhagat, A. A. S.; Kuntaegowdanahalli, S. S.; Papautsky, I. Continuous Particle Separation in Spiral Microchannels Using Dean Flows and Differential Migration. *Lab Chip* **2008**. https://doi.org/10.1039/b807107a.

(50) Yang, J.-Y.; Deng, W.; Chen, Y.; Fan, W.; Baldwin, K. M.; Jope, R. S.; Wallace, D. C.; Wang, P. H. Impaired Translocation and Activation of Mitochondrial Akt1 Mitigated Mitochondrial Oxidative Phosphorylation Complex V Activity in Diabetic Myocardium. *J Mol Cell Cardiol* **2013**, *59*, 167–175. https://doi.org/10.1016/j.yjmcc.2013.02.016.

(51) Sakamuri, S. S. V. P.; Sperling, J. A.; Sure, V. N.; Dholakia, M. H.; Peterson, N. R.; Rutkai, I.; Mahalingam, P. S.; Satou, R.; Katakam, P. V. G. Measurement of Respiratory Function in Isolated

Cardiac Mitochondria Using Seahorse XFe24 Analyzer: Applications for Aging Research. *Geroscience* **2018**, *40* (3), 347–356. https://doi.org/10.1007/s11357-018-0021-3.

(52) Hornig-Do, H.-T.; Günther, G.; Bust, M.; Lehnartz, P.; Bosio, A.; Wiesner, R. J. Isolation of Functional Pure Mitochondria by Superparamagnetic Microbeads. *Anal Biochem* **2009**, *389* (1), 1–5. https://doi.org/10.1016/j.ab.2009.02.040.

(53) Liao, P.; Boldogh, I. R.; Siegmund, S. E.; Freyberg, Z.; Pon, L. A. Isolation of Mitochondria from Saccharomyces Cerevisiae Using Magnetic Bead Affinity Purification. *PLoS One* **2018**, *13* (4), e0196632. https://doi.org/10.1371/journal.pone.0196632.

(54) Bayraktar, E. C.; Baudrier, L.; Özerdem, C.; Lewis, C. A.; Chan, S. H.; Kunchok, T.; Abu-Remaileh, M.; Cangelosi, A. L.; Sabatini, D. M.; Birsoy, K.; Chen, W. W. MITO-Tag Mice Enable Rapid Isolation and Multimodal Profiling of Mitochondria from Specific Cell Types in Vivo. *Proc Natl Acad Sci U S A* **2019**, *116* (1), 303–312. https://doi.org/10.1073/pnas.1816656115.

(55) Chen, W. W.; Freinkman, E.; Wang, T.; Birsoy, K.; Sabatini, D. M. Absolute Quantification of Matrix Metabolites Reveals the Dynamics of Mitochondrial Metabolism. *Cell* **2016**, *166* (5), 1324-1337.e11. https://doi.org/10.1016/j.cell.2016.07.040.

(56) Bard, A. J.; Faulkner, L. R. *Electrochemical Methods. Fundamental and Applications*, 2nd ed.; John Wiley and Sons, Inc.: New York, 2001. https://doi.org/10.1039/C4LC00091A.

(57) Yang, Y.; Gao, W. Wearable and Flexible Electronics for Continuous Molecular Monitoring. *Chem Soc Rev* **2019**, *48* (6), 1465–1491. https://doi.org/10.1039/c7cs00730b.

(58) Datta, D.; Meshik, X.; Mukherjee, S.; Sarkar, K.; Choi, M. S.; Mazouchi, M.; Farid, S.; Wang, Y. Y.; Burke, P. J.; Dutta, M.; Stroscio, M. A. Submillimolar Detection of Adenosine Monophosphate Using Graphene-Based Electrochemical Aptasensor. *IEEE Trans Nanotechnol* **2017**, *16* (2), 196–202. https://doi.org/10.1109/TNANO.2016.2647715.

(59) Hoilett, O. S.; Walker, J. F.; Balash, B. M.; Jaras, N. J.; Boppana, S.; Linnes, J. C. Kickstat: A Coin-Sized Potentiostat for High-Resolution Electrochemical Analysis. *Sensors (Switzerland)* **2020**, *20* (8), 1–12. https://doi.org/10.3390/s20082407.

(60) Nemiroski, A.; Christodouleas, D. C.; Hennek, J. W.; Kumar, A. A.; Maxwell, E. J.; Fernández-Abedul, M. T.; Whitesides, G. M. Universal Mobile Electrochemical Detector Designed for Use in Resource-Limited Applications. *Proc Natl Acad Sci U S A* **2014**, *111* (33), 11984–11989. https://doi.org/10.1073/pnas.1405679111.

(61) Dryden, M. D. M.; Fobel, R.; Fobel, C.; Wheeler, A. R. Upon the Shoulders of Giants: Open-Source Hardware and Software in Analytical Chemistry. *Anal Chem* **2017**, *89* (8), 4330–4338. https://doi.org/10.1021/acs.analchem.7b00485.

(62) Rowe, A. A.; Bonham, A. J.; White, R. J.; Zimmer, M. P.; Yadgar, R. J.; Hobza, T. M.; Honea, J. W.; Ben-Yaacov, I.; Plaxco, K. W. Cheapstat: An Open-Source, "Do-It-Yourself" Potentiostat for Analytical and Educational Applications. *PLoS One* **2011**, *6* (9). https://doi.org/10.1371/journal.pone.0023783.

(63) Dryden, M. D. M.; Wheeler, A. R. DStat: A Versatile, Open-Source Potentiostat for Electroanalysis and Integration. *PLoS One* **2015**, *10* (10). https://doi.org/10.1371/journal.pone.0140349.

(64) Dobbelaere, T.; Vereecken, P. M.; Detavernier, C. A USB-Controlled Potentiostat/Galvanostat for Thin-Film Battery Characterization. *HardwareX* **2017**, *2*, 34–49. https://doi.org/10.1016/j.ohx.2017.08.001.

(65) Ainla, A.; Mousavi, M. P. S.; Tsaloglou, M. N.; Redston, J.; Bell, J. G.; Fernández-Abedul, M. T.; Whitesides, G. M. Open-Source Potentiostat for Wireless Electrochemical Detection with Smartphones. *Anal Chem* **2018**, *90* (10), 6240–6246. https://doi.org/10.1021/acs.analchem.8b00850.

(66) Lopin, P.; Lopin, K. V. PSoC-Stat: A Single Chip Open Source Potentiostat Based on a Programmable System on a Chip. *PLoS One* **2018**, *13* (7), 1–21. https://doi.org/10.1371/journal.pone.0201353.

(67) Jenkins, D. M.; Lee, B. E.; Jun, S.; Reyes-De-Corcuera, J.; McLamore, E. S. ABE-Stat, a Fully Open-Source and Versatile Wireless Potentiostat Project Including Electrochemical Impedance Spectroscopy. *J Electrochem Soc* **2019**, *166* (9), B3056–B3065. https://doi.org/10.1149/2.0061909jes.

(68) Li, J.; Burke, P. J. Measurement of the Combined Quantum and Electrochemical Capacitance of a Carbon Nanotube. *Nat Commun* **2019**, *10* (1), 3598. https://doi.org/10.1038/s41467-019-11589-9.

(69) Glasscott, M. W.; Verber, M. D.; Hall, J. R.; Pendergast, A. D.; McKinney, C. J.; Dick, J. E. SweepStat: A Build-It-Yourself, Two-Electrode Potentiostat for Macroelectrode and Ultramicroelectrode Studies. *J Chem Educ* **2020**, *97* (1), 265–270. https://doi.org/10.1021/acs.jchemed.9b00893.

(70) Cruz, A. F. D.; Norena, N.; Kaushik, A.; Bhansali, S. A Low-Cost Miniaturized Potentiostat for Point-of-Care Diagnosis. *Biosens Bioelectron* **2014**, *62*, 249–254. https://doi.org/10.1016/j.bios.2014.06.053.

(71) Mercer, C.; Bennett, R.; Conghaile, P.; Rusling, J. F.; Leech, D. Glucose Biosensor Based on Open-Source Wireless Microfluidic Potentiostat. *Sens Actuators B Chem* **2019**, *290*, 616–624. https://doi.org/10.1016/j.snb.2019.02.031.

(72) Li, Y. C.; Melenbrink, E. L.; Cordonier, G. J.; Boggs, C.; Khan, A.; Isaac, M. K.; Nkhonjera, L. K.; Bahati, D.; Billinge, S. J.; Haile, S. M.; Kreuter, R. A.; Crable, R. M.; Mallouk, T. E. An Easily Fabricated Low-Cost Potentiostat Coupled with User-Friendly Software for Introducing Students to Electrochemical Reactions and Electroanalytical Techniques. *J Chem Educ* **2018**, *95* (9), 1658–1661. https://doi.org/10.1021/acs.jchemed.8b00340.

(73) Pansodtee, P.; Selberg, J.; Jia, M.; Jafari, M.; Dechiraju, H.; Thomsen, T.; Gomez, M.; Rolandi, M.; Teodorescu, M. The Multi-Channel Potentiostat: Development and Evaluation of a Scalable Mini-Potentiostat Array for Investigating Electrochemical Reaction Mechanisms. *PLoS One* **2021**, *16* (9 September), 1–14. https://doi.org/10.1371/journal.pone.0257167.

(74) Rose, D. P.; Ratterman, M. E.; Griffin, D. K.; Hou, L.; Kelley-Loughnane, N.; Naik, R. R.; Hagen, J. A.; Papautsky, I.; Heikenfeld, J. C. Adhesive RFID Sensor Patch for Monitoring of Sweat Electrolytes. *IEEE Trans Biomed Eng* **2015**, *62* (6), 1457–1465. https://doi.org/10.1109/TBME.2014.2369991.

(75) Kim, J.; Imani, S.; de Araujo, W. R.; Warchall, J.; Valdés-Ramírez, G.; Paixão, T. R. L. C.; Mercier, P. P.; Wang, J. Wearable Salivary Uric Acid Mouthguard Biosensor with Integrated Wireless Electronics. *Biosens Bioelectron* **2015**, *74*, 1061–1068. https://doi.org/10.1016/j.bios.2015.07.039.

(76) Giordano, G. F.; Vicentini, M. B. R.; Murer, R. C.; Augusto, F.; Ferrão, M. F.; Helfer, G. A.; da Costa, A. B.; Gobbi, A. L.; Hantao, L. W.; Lima, R. S. Point-of-Use Electroanalytical Platform Based on Homemade Potentiostat and Smartphone for Multivariate Data Processing. *Electrochim Acta* **2016**, *219* (2016), 170–177. https://doi.org/10.1016/j.electacta.2016.09.157.

(77) Imani, S.; Bandodkar, A. J.; Mohan, A. M. V.; Kumar, R.; Yu, S.; Wang, J.; Mercier, P. P. A Wearable Chemical-Electrophysiological Hybrid Biosensing System for Real-Time Health and Fitness Monitoring. *Nat Commun* **2016**, *7* (May), 1–7. https://doi.org/10.1038/ncomms11650.

(78) Pruna, R.; Palacio, F.; Baraket, A.; Zine, N.; Streklas, A.; Bausells, J.; Errachid, A.; López, M. A Low-Cost and Miniaturized Potentiostat for Sensing of Biomolecular Species Such as TNF-α by Electrochemical Impedance Spectroscopy. *Biosens Bioelectron* **2018**, *100* (July 2017), 533–540. https://doi.org/10.1016/j.bios.2017.09.049.

(79) Bianchi, V.; Boni, A.; Fortunati, S.; Giannetto, M.; Careri, M.; De Munari, I. A Wi-Fi Cloud-Based Portable Potentiostat for Electrochemical Biosensors. *IEEE Trans Instrum Meas* **2020**, *69* (6), 3232–3240. https://doi.org/10.1109/TIM.2019.2928533.

(80) Adams, S. D.; Doeven, E. H.; Quayle, K.; Kouzani, A. Z. MiniStat: Development and Evaluation of a Mini-Potentiostat for Electrochemical Measurements. *IEEE Access* **2019**, *7*, 31903–31912. https://doi.org/10.1109/ACCESS.2019.2902575.

(81) Burke, P. J. A Safe, Open Source, 4G Connected Self-Flying Plane With 1 Hour Flight Time and All Up Weight (AUW) <300 g: Towards a New Class of Internet Enabled UAVs. *IEEE Access* **2019**, *7*, 67833–67855. https://doi.org/10.1109/ACCESS.2019.2917851.

(82) Wallace, D. C.; Fan, W. Energetics, Epigenetics, Mitochondrial Genetics. *Mitochondrion* **2010**, *10* (1), 12–31. https://doi.org/10.1016/j.mito.2009.09.006.

(83) Enríquez, J. A. Supramolecular Organization of Respiratory Complexes. *Annu Rev Physiol* **2016**, *78* (1), 533–561. https://doi.org/10.1146/annurev-physiol-021115-105031.

(84) Burke, P. J. Mitochondria, Bioenergetics and Apoptosis in Cancer. *Trends Cancer* **2017**, *3* (12), 857–870. https://doi.org/10.1016/j.trecan.2017.10.006.

(85) Kondadi, A. K.; Anand, R.; Reichert, A. S. Cristae Membrane Dynamics – A Paradigm Change. *Trends Cell Biol* **2020**, *30* (12), 923–936. https://doi.org/10.1016/j.tcb.2020.08.008.

(86) Iovine, J. C.; Claypool, S. M.; Alder, N. N. Mitochondrial Compartmentalization: Emerging Themes in Structure and Function. *Trends Biochem Sci* **2021**, *46* (11), 902–917. https://doi.org/10.1016/j.tibs.2021.06.003.

(87) Cogliati, S.; Frezza, C.; Soriano, M. E.; Varanita, T.; Quintana-Cabrera, R.; Corrado, M.; Cipolat, S.; Costa, V.; Casarin, A.; Gomes, L. C.; Perales-Clemente, E.; Salviati, L.; Fernandez-Silva, P.; Enriquez, J. A.; Scorrano, L. Mitochondrial Cristae Shape Determines Respiratory Chain Supercomplexes Assembly and Respiratory Efficiency. *Cell* **2013**, *155* (1), 160–171. https://doi.org/10.1016/j.cell.2013.08.032.

(88) Glancy, B.; Kim, Y.; Katti, P.; Willingham, T. B. The Functional Impact of Mitochondrial Structure Across Subcellular Scales. *Front Physiol* **2020**, *11* (November), 1–24. https://doi.org/10.3389/fphys.2020.541040.

(89) Anand, R.; Reichert, A. S.; Kondadi, A. K. Emerging Roles of the MICOS Complex in Cristae Dynamics and Biogenesis. *Biology (Basel)* **2021**, *10* (7), 600. https://doi.org/10.3390/biology10070600.

(90) Hackenbrock, C. R. Ultrastructural Bases for Metabolically Linked Mechanical Activity in Mitochondria. I. Reversible Ultrastructural Changes with Change in Metabolic Steady State in Isolated Liver Mitochondria. *J Cell Biol* **1966**, *30* (2), 269–297. https://doi.org/10.1083/jcb.30.2.269.

(91) Hackenbrock, C. R. Ultrastructural Bases for Metabolically Linked Mechanical Activity in Mitochondria. II. Electron Transport-Linked Ultrastructural Transformations in Mitochondria. *J Cell Biol* **1968**, *37* (2), 345–369. https://doi.org/10.1083/jcb.37.2.345.

(92) Patten, D. A.; Wong, J.; Khacho, M.; Soubannier, V.; Mailloux, R. J.; Pilon-Larose, K.; MacLaurin, J. G.; Park, D. S.; McBride, H. M.; Trinkle-Mulcahy, L.; Harper, M.; Germain, M.; Slack, R. S. OPA1-dependent Cristae Modulation Is Essential for Cellular Adaptation to Metabolic Demand. *EMBO J* **2014**, *33* (22), 2676–2691. https://doi.org/10.15252/embj.201488349.

(93) Jakobs, S.; Stephan, T.; Ilgen, P.; Brüser, C. Light Microscopy of Mitochondria at the Nanoscale. *Annu Rev Biophys* **2020**, *49* (1), 289–308. https://doi.org/10.1146/annurev-biophys-121219-081550.

(94) Wolf, D. M.; Segawa, M.; Kondadi, A. K.; Anand, R.; Bailey, S. T.; Reichert, A. S.; Bliek, A. M.; Shackelford, D. B.; Liesa, M.; Shirihai, O. S. Individual Cristae within the Same Mitochondrion Display Different Membrane Potentials and Are Functionally Independent. *EMBO J* **2019**, *38* (22), e101056. https://doi.org/10.15252/embj.2018101056.

(95) Stephan, T.; Roesch, A.; Riedel, D.; Jakobs, S. Live-Cell STED Nanoscopy of Mitochondrial Cristae. *Sci Rep* **2019**, *9* (1), 12419. https://doi.org/10.1038/s41598-019-48838-2.

(96) Song, Y.; Zhang, X.; Shen, Z.; Yang, W.; Wei, J.; Li, S.; Wang, X.; Li, X.; He, Q.; Zhang, S.; Zhang, Q.; Gao, B. Improving Brightness and Stability of Si-Rhodamine for Super-Resolution Imaging of Mitochondria in Living Cells. *Anal Chem* **2020**, *92* (18), 12137–12144. https://doi.org/10.1021/acs.analchem.9b04926.

(97) Yang, X.; Yang, Z.; Wu, Z.; He, Y.; Shan, C.; Chai, P.; Ma, C.; Tian, M.; Teng, J.; Jin, D.; Yan, W.; Das, P.; Qu, J.; Xi, P. Mitochondrial Dynamics Quantitatively Revealed by STED Nanoscopy with an Enhanced Squaraine Variant Probe. *Nat Commun* **2020**, *11* (1), 3699. https://doi.org/10.1038/s41467-020-17546-1.

(98) Scaduto, R. C.; Grotyohann, L. W. Measurement of Mitochondrial Membrane Potential Using Fluorescent Rhodamine Derivatives. *Biophys J* **1999**, *76* (1), 469–477. https://doi.org/10.1016/S0006-3495(99)77214-0.

(99) Lim, T.-S.; Davila, A.; Wallace, D. C.; Burke, P. J. Assessment of Mitochondrial Membrane Potential Using an On-Chip Microelectrode in a Microfluidic Device. *Lab Chip* **2010**, *10*, 1683–1688.

(100) Lim, T.-S.; Davila, A.; Zand, K.; Wallace, D. C.; Burke, P. J. Wafer-Scale Mitochondrial Membrane Potential Assays. *Lab Chip* **2012**, *12* (15), 2719–2725. https://doi.org/10.1039/c2lc40086c.

(101) Demura, M.; Kamo, N.; Kobatake, Y. Mitochondrial Membrane Potential Estimated with the Correction of Probe Binding. *Biochimica et Biophysica Acta (BBA) - Bioenergetics* **1987**, *894* (3), 355–364. https://doi.org/10.1016/0005-2728(87)90113-7.

(102) Gerencser, A. A.; Chinopoulos, C.; Birket, M. J.; Jastroch, M.; Vitelli, C.; Nicholls, D. G.; Brand, M. D. Quantitative Measurement of Mitochondrial Membrane Potential in Cultured Cells: Calcium-Induced de- and Hyperpolarization of Neuronal Mitochondria. *J Physiol* **2012**, *590* (Pt 12), 2845–2871. https://doi.org/10.1113/jphysiol.2012.228387.

(103) Vergun, O.; Reynolds, I. J. Fluctuations in Mitochondrial Membrane Potential in Single Isolated Brain Mitochondria: Modulation by Adenine Nucleotides and Ca2+. *Biophys J* **2004**, *87* (5), 3585–3593. https://doi.org/10.1529/biophysj.104.042671.

(104) Jacobson, J.; Duchen, M. R.; Heales, S. J. R. Intracellular Distribution of the Fluorescent Dye Nonyl Acridine Orange Responds to the Mitochondrial Membrane Potential: Implications for Assays of Cardiolipin and Mitochondrial Mass. *J Neurochem* **2002**, *82* (2), 224–233. https://doi.org/10.1046/j.1471-4159.2002.00945.x.

(105) Nicholls, D. G. Fluorescence Measurement of Mitochondrial Membrane Potential Changes in Cultured Cells. *Methods Mol Biol* **2012**, *810*, 119–133. https://doi.org/10.1007/978-1-61779-382-0_8.

(106) Duchen, M. R.; Surin, A.; Jacobson, J. Imaging Mitochondrial Function in Intact Cells. *Methods Enzymol* **2003**, *361* (2001), 353–389. https://doi.org/10.1016/s0076-6879(03)61019-0.

(107) Teodoro, J. S.; Palmeira, C. M.; Rolo, A. P. Mitochondrial Membrane Potential (ΔΨ) Fluctuations Associated with the Metabolic States of Mitochondria. *Methods Mol Biol* **2018**, *1782*, 109–119. https://doi.org/10.1007/978-1-4939-7831-1_6.

(108) Rottenberg, H. Membrane Potential and Surface Potential in Mitochondria: Uptake and Binding of Lipophilic Cations. *J Membr Biol* **1984**, *81* (2), 127–138. https://doi.org/10.1007/BF01868977.

(109) Komlódi, T.; Geibl, F. F.; Sassani, M.; Ambrus, A.; Tretter, L. Membrane Potential and Delta PH Dependency of Reverse Electron Transport-Associated Hydrogen Peroxide Production in Brain and Heart Mitochondria. *J Bioenerg Biomembr* **2018**, *50* (5), 355–365. https://doi.org/10.1007/s10863-018-9766-8.

(110) Cortese, J. D.; Voglino, A. L.; Hackenbrock, C. R. The Ionic Strength of the Intermembrane Space of Intact Mitochondria Is Not Affected by the PH or Volume of the Intermembrane Space. *Biochim Biophys Acta* **1992**, *1100* (2), 189–197. https://doi.org/10.1016/0005-2728(92)90081-c.

(111) Porcelli, A. M.; Ghelli, A.; Zanna, C.; Pinton, P.; Rizzuto, R.; Rugolo, M. PH Difference across the Outer Mitochondrial Membrane Measured with a Green Fluorescent Protein Mutant. *Biochem Biophys Res Commun* **2005**, *326* (4), 799–804. https://doi.org/10.1016/j.bbrc.2004.11.105.

(112) Santo-Domingo, J.; Demaurex, N. The Renaissance of Mitochondrial PH. *J Gen Physiol* **2012**, *139* (6), 391–393. https://doi.org/10.1085/jgp.201210819.

(113) Rieger, B.; Junge, W.; Busch, K. B. Lateral PH Gradient between OXPHOS Complex IV and F(0)F(1) ATP-Synthase in Folded Mitochondrial Membranes. *Nat Commun* **2014**, *5*, 3103. https://doi.org/10.1038/ncomms4103.

(114) Silverstein, T. P. The Proton in Biochemistry: Impacts on Bioenergetics, Biophysical Chemistry, and Bioorganic Chemistry. *Front Mol Biosci* **2021**, *8*, 764099. https://doi.org/10.3389/fmolb.2021.764099.

(115) Goch, W.; Bal, W. Stochastic or Not? Method To Predict and Quantify the Stochastic Effects on the Association Reaction Equilibria in Nanoscopic Systems. *J Phys Chem A* **2020**, *124* (7), 1421–1428. https://doi.org/10.1021/acs.jpca.9b09441.

(116) Shon, M. J.; Cohen, A. E. Mass Action at the Single-Molecule Level. *J Am Chem Soc* **2012**, *134* (35), 14618–14623. https://doi.org/10.1021/ja3062425.

(117) Żurawik, T. M.; Pomorski, A.; Belczyk-Ciesielska, A.; Goch, G.; Niedźwiedzka, K.; Kucharczyk, R.; Krężel, A.; Bal, W. Revisiting Mitochondrial PH with an Improved Algorithm for Calibration of the Ratiometric 5(6)-Carboxy-SNARF-1 Probe Reveals Anticooperative Reaction with H+ Ions and Warrants Further Studies of Organellar PH. *PLoS One* **2016**, *11* (8), e0161353. https://doi.org/10.1371/journal.pone.0161353.

(118) Silverstein, T. P. A Critique of the Capacitor-Based “Transmembrane Electrostatically Localized Proton” Hypothesis. *Journal of Bioenergetics and Biomembranes*. Springer April 1, 2022, pp 59–65. https://doi.org/10.1007/s10863-022-09931-w.

(119) Lee, J. W. Protonic Capacitor: Elucidating the Biological Significance of Mitochondrial Cristae Formation. *Sci Rep* **2020**, *10* (1), 10304. https://doi.org/10.1038/s41598-020-66203-6.

(120) Usselman, R. J.; Chavarriaga, C.; Castello, P. R.; Procopio, M.; Ritz, T.; Dratz, E. A.; Singel, D. J.; Martino, C. F. The Quantum Biology of Reactive Oxygen Species Partitioning Impacts Cellular Bioenergetics. *Sci Rep* **2016**, *6* (1), 38543. https://doi.org/10.1038/srep38543.

(121) Nie, L.; Nusantara, A. C.; Damle, V. G.; Sharmin, R.; Evans, E. P. P.; Hemelaar, S. R.; van der Laan, K. J.; Li, R.; Perona Martinez, F. P.; Vedelaar, T.; Chipaux, M.; Schirhagl, R. Quantum Monitoring of Cellular Metabolic Activities in Single Mitochondria. *Sci Adv* **2021**, *7* (21), 1–9. https://doi.org/10.1126/sciadv.abf0573.

(122) Chen, H.; Chan, D. C. Mitochondrial Dynamics-Fusion, Fission, Movement, and Mitophagy-in Neurodegenerative Diseases. *Hum Mol Genet* **2009**, *18* (R2), R169–R176. https://doi.org/10.1093/hmg/ddp326.

(123) Friedman, J. R.; Nunnari, J. Mitochondrial Form and Function. *Nature* **2014**, *505* (7483), 335–343. https://doi.org/10.1038/nature12985.

(124) Chan, D. C. Fusion and Fission: Interlinked Processes Critical for Mitochondrial Health. *Annu Rev Genet* **2012**, *46* (1), 265–287. https://doi.org/10.1146/annurev-genet-110410-132529.

(125) Huang, X.; Fan, J.; Li, L.; Liu, H.; Wu, R.; Wu, Y.; Wei, L.; Mao, H.; Lal, A.; Xi, P.; Tang, L.; Zhang, Y.; Liu, Y.; Tan, S.; Chen, L. Fast, Long-Term, Super-Resolution Imaging with Hessian Structured Illumination Microscopy. *Nat Biotechnol* **2018**, *36* (5), 451–459. https://doi.org/10.1038/nbt.4115.

(126) Guo, Y.; Li, D.; Zhang, S.; Yang, Y.; Liu, J. J.; Wang, X.; Liu, C.; Milkie, D. E.; Moore, R. P.; Tulu, U. S.; Kiehart, D. P.; Hu, J.; Lippincott-Schwartz, J.; Betzig, E.; Li, D. Visualizing Intracellular Organelle and Cytoskeletal Interactions at Nanoscale Resolution on Millisecond Timescales. *Cell* **2018**, *175* (5), 1430-1442.e17. https://doi.org/10.1016/j.cell.2018.09.057.

(127) Kondadi, A. K.; Anand, R.; Hänsch, S.; Urbach, J.; Zobel, T.; Wolf, D. M.; Segawa, M.; Liesa, M.; Shirihai, O. S.; Weidtkamp-Peters, S.; Reichert, A. S. Cristae Undergo Continuous Cycles of Membrane Remodelling in a MICOS -dependent Manner . *EMBO Rep* **2020**, *21* (3), 1–22. https://doi.org/10.15252/embr.201949776.

(128) Liu, T.; Stephan, T.; Chen, P.; Keller-Findeisen, J.; Chen, J.; Riedel, D.; Yang, Z.; Jakobs, S.; Chen, Z. Multi-Color Live-Cell STED Nanoscopy of Mitochondria with a Gentle Inner Membrane Stain. *Proc Natl Acad Sci U S A* **2022**, *119* (52). https://doi.org/10.1073/pnas.2215799119.

(129) Yang, Z.; Li, L.; Ling, J.; Liu, T.; Huang, X.; Ying, Y.; Zhao, Y.; Zhao, Y.; Lei, K.; Chen, L.; Chen, Z. Cyclooctatetraene-Conjugated Cyanine Mitochondrial Probes Minimize Phototoxicity in Fluorescence and Nanoscopic Imaging. *Chem Sci* **2020**, *11* (32), 8506–8516. https://doi.org/10.1039/d0sc02837a.

(130) Kilian, N.; Goryaynov, A.; Lessard, M. D.; Hooker, G.; Toomre, D.; Rothman, J. E.; Bewersdorf, J. Assessing Photodamage in Live-Cell STED Microscopy. *Nat Methods* **2018**, *15* (10), 755–756. https://doi.org/10.1038/s41592-018-0145-5.

(131) Waldchen, S.; Lehmann, J.; Klein, T.; Van De Linde, S.; Sauer, M. Light-Induced Cell Damage in Live-Cell Super-Resolution Microscopy. *Sci Rep* **2015**, *5*, 1–12. https://doi.org/10.1038/srep15348.

(132) Laissue, P. P.; Alghamdi, R. A.; Tomancak, P.; Reynaud, E. G.; Shroff, H. Assessing Phototoxicity in Live Fluorescence Imaging. *Nat Methods* **2017**, *14* (7), 657–661. https://doi.org/10.1038/nmeth.4344.

(133) Wang, C.; Taki, M.; Sato, Y.; Tamura, Y.; Yaginuma, H.; Okada, Y.; Yamaguchi, S. A Photostable Fluorescent Marker for the Superresolution Live Imaging of the Dynamic Structure of the Mitochondrial Cristae. *Proceedings of the National Academy of Sciences* **2019**, *116* (32), 15817–15822. https://doi.org/10.1073/pnas.1905924116.

(134) Ge, J.; Wood, D. K.; Weingeist, D. M.; Prasongtanakij, S.; Navasumrit, P.; Ruchirawat, M.; Engelward, B. P. Standard Fluorescent Imaging of Live Cells Is Highly Genotoxic. *Cytometry Part A* **2013**, *83 A* (6), 552–560. https://doi.org/10.1002/cyto.a.22291.

(135) Mutoh, H.; Perron, A.; Akemann, W.; Iwamoto, Y.; Knöpfel, T. Optogenetic Monitoring of Membrane Potentials. *Exp Physiol* **2011**, *96* (1), 13–18. https://doi.org/10.1113/expphysiol.2010.053942.

(136) Kwon, J.; Elgawish, M. S.; Shim, S.-H. Bleaching-Resistant Super-Resolution Fluorescence Microscopy. *Adv Sci (Weinh)* **2022**, *9* (9), e2101817. https://doi.org/10.1002/advs.202101817.

(137) Wolf, D. M.; Segawa, M.; Shirihai, O. S.; Liesa, M. Method for Live-Cell Super-Resolution Imaging of Mitochondrial Cristae and Quantification of Submitochondrial Membrane Potentials. *Methods Cell Biol* **2020**, *155*, 545–555. https://doi.org/10.1016/bs.mcb.2019.12.006.

(138) Ojha, A.; Ojha, N. K. Excitation Light-Induced Phototoxicity during Fluorescence Imaging. *J Biosci* **2021**, *46* (3).

(139) Minamikawa, T.; Sriratana, A.; Williams, D. A.; Bowser, D. N.; Hill, J. S.; Nagley, P. Chloromethyl-X-Rosamine (MitoTracker Red) Photosensitises Mitochondria and Induces Apoptosis in Intact Human Cells. *J Cell Sci* **1999**, *112* (14), 2419–2430. https://doi.org/10.1242/jcs.112.14.2419.

(140) Icha, J.; Weber, M.; Waters, J. C.; Norden, C. Phototoxicity in Live Fluorescence Microscopy, and How to Avoid It. *Bioessays* **2017**, *39* (8). https://doi.org/10.1002/bies.201700003.

(141) Chen, Y.; Liu, W.; Zhang, Z.; Zheng, C.; Huang, Y.; Cao, R.; Zhu, D.; Xu, L.; Zhang, M.; Zhang, Y. H.; Fan, J.; Jin, L.; Xu, Y.; Kuang, C.; Liu, X. Multi-Color Live-Cell Super-Resolution Volume Imaging with Multi-Angle Interference Microscopy. *Nat Commun* **2018**, *9* (1). https://doi.org/10.1038/s41467-018-07244-4.

(142) Magidson, V.; Khodjakov, A. Circumventing Photodamage in Live-Cell Microscopy. In *Methods in Cell Biology*; Academic Press Inc., 2013; Vol. 114, pp 545–560. https://doi.org/10.1016/B978-0-12-407761-4.00023-3.

(143) Mubaid, F.; Brown, C. M. Less Is More: Longer Exposure Times with Low Light Intensity Is Less Photo-Toxic. *Micros Today* **2017**, *25* (6), 26–35. https://doi.org/10.1017/S1551929517000980.

(144) Boudreau, C.; Wee, T. L.; Duh, Y. R.; Couto, M. P.; Ardakani, K. H.; Brown, C. M. Excitation Light Dose Engineering to Reduce Photo-Bleaching and Photo-Toxicity. *Sci Rep* **2016**, *6*. https://doi.org/10.1038/srep30892.

(145) Markova, L.; Novohradsky, V.; Kasparkova, J.; Ruiz, J.; Brabec, V. Dipyridophenazine Iridium(III) Complex as a Phototoxic Cancer Stem Cell Selective, Mitochondria Targeting Agent. *Chem Biol Interact* **2022**, *360*. https://doi.org/10.1016/j.cbi.2022.109955.

(146) Ray, R. S.; Mujtaba, S. F.; Dwivedi, A.; Yadav, N.; Verma, A.; Kushwaha, H. N.; Amar, S. K.; Goel, S.; Chopra, D. Singlet Oxygen Mediated DNA Damage Induced Phototoxicity by Ketoprofen Resulting in Mitochondrial Depolarization and Lysosomal Destabilization. *Toxicology* **2013**, *314* (2–3), 229–237. https://doi.org/10.1016/j.tox.2013.10.002.

(147) Tosheva, K. L.; Yuan, Y.; Matos Pereira, P.; Culley, S.; Henriques, R. Between Life and Death: Strategies to Reduce Phototoxicity in Super-Resolution Microscopy. *J Phys D Appl Phys* **2020**, *53* (16), 163001. https://doi.org/10.1088/1361-6463/ab6b95.

(148) Stockley, J. H.; Evans, K.; Matthey, M.; Volbracht, K.; Agathou, S.; Mukanowa, J.; Burrone, J.; Káradóttir, R. T. Surpassing Light-Induced Cell Damage in Vitro with Novel Cell Culture Media. *Sci Rep* **2017**, *7* (1). https://doi.org/10.1038/s41598-017-00829-x.

(149) Klein Geltink, R. I.; O'Sullivan, D.; Corrado, M.; Bremser, A.; Buck, M. D.; Buescher, J. M.; Firat, E.; Zhu, X.; Niedermann, G.; Caputa, G.; Kelly, B.; Warthorst, U.; Rensing-Ehl, A.; Kyle, R. L.; Vandersarren, L.; Curtis, J. D.; Patterson, A. E.; Lawless, S.; Grzes, K.; Qiu, J.; Sanin, D. E.; Kretz, O.; Huber, T. B.; Janssens, S.; Lambrecht, B. N.; Rambold, A. S.; Pearce, E. J.; Pearce, E. L. Mitochondrial Priming by CD28. *Cell* **2017**, *171* (2), 385-397.e11. https://doi.org/10.1016/j.cell.2017.08.018.

(150) Hibshman, J. D.; Sherwood, D. R. Acute and Intergenerational Nutrient Responses in Caenorhabditis Elegans, 2017. https://www.proquest.com/docview/1983444510?pq-origsite=gscholar&fromopenview=true (accessed 2022-10-16).

(151) Rasmussen, M. L.; Taneja, N.; Neininger, A. C.; Wang, L.; Robertson, G. L.; Riffle, S. N.; Shi, L.; Knollmann, B. C.; Burnette, D. T.; Gama, V. MCL-1 Inhibition by Selective BH3 Mimetics Disrupts Mitochondrial Dynamics Causing Loss of Viability and Functionality of Human Cardiomyocytes. *iScience* **2020**, *23* (4), 101015. https://doi.org/10.1016/j.isci.2020.101015.

(152) Bahat, A.; Goldman, A.; Zaltsman, Y.; Khan, D. H.; Halperin, C.; Amzallag, E.; Krupalnik, V.; Mullokandov, M.; Silberman, A.; Erez, A.; Schimmer, A. D.; Hanna, J. H.; Gross, A. MTCH2-Mediated Mitochondrial Fusion Drives Exit from Naïve Pluripotency in Embryonic Stem Cells. *Nat Commun* **2018**, *9* (1), 5132. https://doi.org/10.1038/s41467-018-07519-w.

(153) Bagamery, L. E.; Justman, Q. A.; Garner, E. C.; Murray, A. W. A Putative Bet-Hedging Strategy Buffers Budding Yeast against Environmental Instability. *Current Biology* **2020**, *30* (23), 4563-4578.e4. https://doi.org/10.1016/j.cub.2020.08.092.

(154) Cackovic, J.; Gutierrez-Luke, S.; Call, G. B.; Juba, A.; O'Brien, S.; Jun, C. H.; Buhlman, L. M. Vulnerable Parkin Loss-of-Function Drosophila Dopaminergic Neurons Have Advanced Mitochondrial Aging, Mitochondrial Network Loss and Transiently Reduced Autophagosome Recruitment. *Front Cell Neurosci* **2018**, *12* (February), 1–14. https://doi.org/10.3389/fncel.2018.00039.

(155) Balboa, E.; Castro, J.; Pinochet, M.-J.; Cancino, G. I.; Matías, N.; Sáez, P. J.; Martínez, A.; Álvarez, A. R.; Garcia-Ruiz, C.; Fernandez-Checa, J. C.; Zanlungo, S. MLN64 Induces Mitochondrial Dysfunction Associated with Increased Mitochondrial Cholesterol Content. *Redox Biol* **2017**, *12* (February), 274–284. https://doi.org/10.1016/j.redox.2017.02.024.

(156) Schermelleh, L.; Ferrand, A.; Huser, T.; Eggeling, C.; Sauer, M.; Biehlmaier, O.; Drummen, G. P. C. Super-Resolution Microscopy Demystified. *Nat Cell Biol* **2019**, *21* (1), 72–84. https://doi.org/10.1038/s41556-018-0251-8.

(157) Jacquemet, G.; Carisey, A. F.; Hamidi, H.; Henriques, R.; Leterrier, C. The Cell Biologist's Guide to Super-Resolution Microscopy. *J Cell Sci* **2020**, *133* (11). https://doi.org/10.1242/jcs.240713.

(158) Fry, M. Y.; Navarro, P. P.; Hakim, P.; Ananda, V. Y.; Qin, X.; Landoni, J. C.; Rath, S.; Inde, Z.; Lugo, C. M.; Luce, B. E.; Ge, Y.; McDonald, J. L.; Ali, I.; Ha, L. L.; Kleinstiver, B. P.; Chan, D. C.; Sarosiek, K. A.; Chao, L. H. In Situ Architecture of Opa1-Dependent Mitochondrial Cristae Remodeling. *bioRxiv* **2023**. https://doi.org/10.1101/2023.01.16.524176.

(159) Torrens-Mas, M.; Collado-Solé, A.; Sola-Leyva, A.; Carrasco-Jiménez, M. P.; Oliver, J.; Pons, D. G.; Roca, P.; Sastre-Serra, J. Mitochondrial Functionality Is Regulated by Alkylphospholipids in Human Colon Cancer Cells. *Biology (Basel)* **2023**, *12* (12), 1457. https://doi.org/10.3390/biology12121457.

(160) Sagar, S.; Faizan, M. I.; Chaudhary, N.; Singh, V.; Singh, P.; Gheware, A.; Sharma, K.; Azmi, I.; Singh, V. P.; Kharya, G.; Mabalirajan, U.; Agrawal, A.; Ahmad, T.; Sinha Roy, S. Obesity Impairs Cardiolipin-Dependent Mitophagy and Therapeutic Intercellular Mitochondrial Transfer Ability of Mesenchymal Stem Cells. *Cell Death Dis* **2023**, *14* (5), 324. https://doi.org/10.1038/s41419-023-05810-3.

(161) Dong, J.; Chen, L.; Ye, F.; Tang, J.; Liu, B.; Lin, J.; Zhou, P.-H.; Lu, B.; Wu, M.; Lu, J.-H.; He, J.-J.; Engelender, S.; Meng, Q.; Song, Z.; He, H. Mic19 Depletion Impairs Endoplasmic Reticulum-Mitochondrial Contacts and Mitochondrial Lipid Metabolism and Triggers Liver Disease. *Nat Commun* **2024**, *15* (1), 168. https://doi.org/10.1038/s41467-023-44057-6.

(162) Cinat, D.; Souza, A. L. De; Soto-Gamez, A.; Jellema-de Bruin, A. L.; Coppes, R. P.; Barazzuol, L. Mitophagy Induction Improves Salivary Gland Stem/Progenitor Cell Function by Reducing Senescence after Irradiation. *Radiotherapy and Oncology* **2024**, *190*, 110028. https://doi.org/10.1016/j.radonc.2023.110028.

(163) Zhang, Z.; Zhou, H.; Gu, W.; Wei, Y.; Mou, S.; Wang, Y.; Zhang, J.; Zhong, Q. CGI1746 Targets Σ1R to Modulate Ferroptosis through Mitochondria-Associated Membranes. *Nat Chem Biol* **2024**. https://doi.org/10.1038/s41589-023-01512-1.

(164) Kok, C. Y.; Ghossein, G.; Igoor, S.; Rao, R.; Titus, T.; Tsurusaki, S.; Chong, J. J.; Kizana, E. Ghrelin Mediated Cardioprotection Using in Vitro Models of Oxidative Stress. *Gene Ther* **2024**. https://doi.org/10.1038/s41434-023-00435-9.

(165) Septinus, M.; Berthold, Th.; Naujok, A.; Zimmermann, H. W. [Hydrophobic Acridine Dyes for Fluorescent Staining of Mitochondria in Living Cells. 3. Specific Accumulation of the Fluorescent

Dye NAO on the Mitochondrial Membranes in HeLa Cells by Hydrophobic Interaction. Depression of Respiratory Activity, Changes in the Ultrastructure of Mitochondria Due to NAO. Increase of Fluorescence in Vital Stained Mitochondria in Situ by Irradiation]. *Histochemistry* **1985**, *82* (1), 51–66. https://doi.org/10.1007/BF00502091.

(166) Almendro-Vedia, V. G.; García, C.; Ahijado-Guzmán, R.; de la Fuente-Herreruela, D.; Muñoz-Úbeda, M.; Natale, P.; Viñas, M. H.; Albuquerque, R. Q.; Guerrero-Martínez, A.; Monroy, F.; Pilar Lillo, M.; López-Montero, I. Supramolecular Zippers Elicit Interbilayer Adhesion of Membranes Producing Cell Death. *Biochim Biophys Acta Gen Subj* **2018**, *1862* (12), 2824–2834. https://doi.org/10.1016/j.bbagen.2018.08.018.

(167) Vianello, C.; Dal Bello, F.; Shin, S. H.; Schiavon, S.; Bean, C.; Magalhães Rebelo, A. P.; Knedlík, T.; Esfahani, E. N.; Costiniti, V.; Lacruz, R. S.; Covello, G.; Munari, F.; Scolaro, T.; Viola, A.; Rampazzo, E.; Persano, L.; Zumerle, S.; Scorrano, L.; Gianelle, A.; Giacomello, M. High-Throughput Microscopy Analysis of Mitochondrial Membrane Potential in 2D and 3D Models. *Cells* **2023**, *12* (7), 1089. https://doi.org/10.3390/cells12071089.

(168) Lee, C.; Wallace, D. C.; Burke, P. J. Super-Resolution Imaging of Voltages in the Interior of Individual, Vital Mitochondria. *ACS Nano* **2024**, *18* (2), 1345–1356. https://doi.org/10.1021/acsnano.3c02768.

(169) Keij, J. F.; Bell-Prince, C.; Steinkamp, J. A. Staining of Mitochondrial Membranes with 10-Nonyl Acridine Orange, MitoFluor Green, and MitoTracker Green Is Affected by Mitochondrial Membrane Potential Altering Drugs. *Cytometry* **2000**, *39* (3), 203–210. https://doi.org/10.1002/(sici)1097-0320(20000301)39:3<203::aid-cyto5>3.0.co;2-z.

(170) Garcia Fernandez, M. I.; Ceccarelli, D.; Muscatello, U. Use of the Fluorescent Dye 10-N-Nonyl Acridine Orange in Quantitative and Location Assays of Cardiolipin: A Study on Different Experimental Models. *Anal Biochem* **2004**, *328* (2), 174–180. https://doi.org/10.1016/j.ab.2004.01.020.

(171) Hennig, S.; Manstein, D. J. Improvement of Image Resolution by Combining Enhanced Confocal Microscopy and Quantum Dot Triexciton Imaging. *FEBS Open Bio* **2021**, *11* (12), 3324–3330. https://doi.org/10.1002/2211-5463.13246.

(172) Scorrano, L.; Ashiya, M.; Buttle, K.; Weiler, S.; Oakes, S. A.; Mannella, C. A.; Korsmeyer, S. J. A Distinct Pathway Remodels Mitochondrial Cristae and Mobilizes Cytochrome c during Apoptosis. *Dev Cell* **2002**, *2* (1), 55–67. https://doi.org/10.1016/S1534-5807(01)00116-2.

(173) Frezza, C.; Cipolat, S.; Martins de Brito, O.; Micaroni, M.; Beznoussenko, G. V; Rudka, T.; Bartoli, D.; Polishuck, R. S.; Danial, N. N.; De Strooper, B.; Scorrano, L. OPA1 Controls Apoptotic Cristae Remodeling Independently from Mitochondrial Fusion. *Cell* **2006**, *126* (1), 177–189. https://doi.org/10.1016/j.cell.2006.06.025.

(174) Sun, M. G.; Williams, J.; Munoz-Pinedo, C.; Perkins, G. A.; Brown, J. M.; Ellisman, M. H.; Green, D. R.; Frey, T. G. Correlated Three-Dimensional Light and Electron Microscopy Reveals

Transformation of Mitochondria during Apoptosis. *Nat Cell Biol* **2007**, *9* (9), 1057–1072. https://doi.org/10.1038/ncb1630.

(175) Yamaguchi, R.; Lartigue, L.; Perkins, G.; Scott, R. T.; Dixit, A.; Kushnareva, Y.; Kuwana, T.; Ellisman, M. H.; Newmeyer, D. D. Opa1-Mediated Cristae Opening Is Bax/Bak and BH3 Dependent, Required for Apoptosis, and Independent of Bak Oligomerization. *Mol Cell* **2008**, *31* (4), 557–569. https://doi.org/10.1016/j.molcel.2008.07.010.

(176) Yamaguchi, R.; Perkins, G. Dynamics of Mitochondrial Structure during Apoptosis and the Enigma of Opa1. *Biochimica et Biophysica Acta (BBA) - Bioenergetics* **2009**, *1787* (8), 963–972. https://doi.org/10.1016/j.bbabio.2009.02.005.

(177) MacVicar, T.; Langer, T. OPA1 Processing in Cell Death and Disease – the Long and Short of It. *J Cell Sci* **2016**, *129* (12), 2297–2306. https://doi.org/10.1242/jcs.159186.

(178) Head, B.; Griparic, L.; Amiri, M.; Gandre-Babbe, S.; van der Bliek, A. M. Inducible Proteolytic Inactivation of OPA1 Mediated by the OMA1 Protease in Mammalian Cells. *J Cell Biol* **2009**, *187* (7), 959–966. https://doi.org/10.1083/jcb.200906083.

(179) Jiang, X.; Jiang, H.; Shen, Z.; Wang, X. Activation of Mitochondrial Protease OMA1 by Bax and Bak Promotes Cytochrome c Release during Apoptosis. *Proceedings of the National Academy of Sciences* **2014**, *111* (41), 14782–14787. https://doi.org/10.1073/pnas.1417253111.

(180) Cafiso, D. S.; Hubbell, W. L. Estimation of Transmembrane Potentials from Phase Equilibriums of Hydrophobic Paramagnetic Ions. *Biochemistry* **1978**, *17* (1), 187–206.

(181) Callen, H. B.; Scott, H. L. Thermodynamics and an Introduction to Thermostatistics, 2nd Ed. *Am J Phys* **1998**, *66* (2), 164–167. https://doi.org/10.1119/1.19071.

(182) Bradford, M. A Rapid and Sensitive Method for the Quantitation of Microgram Quantities of Protein Utilizing the Principle of Protein-Dye Binding. *Anal Biochem* **1976**, *72* (1–2), 248–254. https://doi.org/10.1006/abio.1976.9999.

APPENDIX A. LITERATURE DISCUSSION ABOUT THE MEMBRANE BINDING FACTORS

The electron spin resonance spectra of certain spin labeled lipophilic cations depend on whether the cation was bound or free. This was used to measure the amount of bound vs. free cation in liposome suspensions in 1978 [180], for zero voltage and the controlled voltage across the liposome. This proved that the amount of bound cation was voltage-dependent. Furthermore, measurements showed that the rate/binding constants were such that the amount of bound cation (by mole #) was much larger than that free and inside the liposome, by at least an order of magnitude.

The rate constants and binding were quantitatively measured in mitochondrial suspensions in 1987 by Kamo [101] for tetraphenylphosphonium (TPP^+) lipophilic cations: By using electrochemical detection of the TPP^+ concentration in the buffer under various conditions, the authors were able to show that, similar to the liposomes, 1) the amount of TPP^+ cation bound to the mitochondrial membrane was voltage-dependent, and 2) the number of TPP^+ molecules bound to the mitochondrial membrane was much larger than the # free inside the mitochondria (matrix). A similar series of experiments used TMRE (as we do) and optical detection of the amount in the buffer to find the quantitative rate constants for mitochondria [98]. They found that, at 28 ℃, the ratio of # TMRE molecules bound to the inner membrane to the # of TMRE molecules free in the inner matrix was 60, and 129 for the similar ratio for the outer membrane binding (buffer side). (See units discussion in supporting information.)

A detailed description of the binding model

The TMRE is assumed to be low enough density (at 10 nM) so that:

- The # of TMRE per surface area of the bilayer is not saturating all of the possible binding sites. (Large-density TMRE will saturate the binding, as shown in [101,108].)
- The TMRE charge does not significantly perturb the electrostatics (electric fields), since other charged species such as H^+, K^+, Cl^-, and OH^-, are many orders of magnitude higher in concentration (μM to 0.1 M), and the fields generated by those charges is not changed much by the presence/absence of TMRE at 10 nM. That said, there will be some small OH^- or other negative charges to balance the TMRE positive charge.

The fundamental thermodynamic model regarding the binding of TMRE or any other lipophilic cation is based on the following assumption: The TMRE can move between different compartments, and the compartments are in equilibrium. The model used in this paper has four compartments, shown in Figure 3-3.

Here, equilibrium means there is no net change in the average TMRE concentration with time, although it may fluctuate about the mean. Thermodynamics considerations of the Gibbs Free energy [181] imply that the electrochemical potential is constant. (At zero membrane voltage, the electrochemical potential is the chemical potential). If the energy of each compartment was the same, this would mean that the density of TMRE is the same in each compartment. However, there is a potential well for bound TMRE (see Figure 3-3 in the main text), indicating that the densities will not be the same, even though the chemical potentials are the same.

The "density" of TMRE in the bilayer membrane is defined as the # of TMRE molecules/volume of the membrane compartment. The volume of the membrane compartment is equal to the membrane surface area times the width of the compartment (indicated as δ in Figure 3-3). This is a model, which will be compared to experiments presently (below).

We make the following definitions for the density of TMRE molecules: n_i is the free TMRE inside a liposome or in the case of mitochondria inside the mitochondria, i.e. in the region called the matrix. n_{bi} is the density of bound TMRE bound to the inside surface of the membrane (in the case of a liposome) or the inside i.e. matrix surface of the membrane (in the case of mitochondria). Similarly, n_o is the density of free TMRE on the outside of the liposome or (in the case of mitochondria) on the cytosol (in cells) or buffer (in isolated suspensions of mitochondria). n_{bo} is the density of TMRE bound to the outer membrane surface (in the case of liposomes) or the outer mitochondria membrane surface (cytosol or buffer side) in the case of mitochondria. The bilayer is not assumed to be symmetric.

We define a_o as the constant of proportionality between n_o and n_{bo}. Through the following equation:

$$n_{bo} = a_o n_o$$

Similarly, for a_i:

$$n_{bi} = a_i n_i$$

Our definition does not provide any sort of a microscopic model for the origins of a_o or a_i, other than the assumptions of thermodynamic equilibrium and the overall shape of the potential shown in Figure 3-3. The bilayer is not assumed to be symmetric, so we do not assume a_o and a_i are equal. Our definition is for expositional clarity in this paper's context, and not a standard in the literature. We do assume a_o and a_i are constants regardless of the membrane potential. This assumption is implicit in all of the literature to date [98,101,180].

Various authors in the literature have provided microscopic models for the value of a_o. Rottenberg [108], instead of a_o, used $K_{mo}\alpha_o$, where "K_{mo} is the ion partition coefficient for the external surface of the membrane and α_o is a function of the external surface potential ψ_o". Note that the surface potential is NOT the membrane potential, and is assumed to be constant [7].

The units of a_o or a_i are dimensionless. However, in practice, one does not easily know, and cannot easily measure, the exact surface area of the lipid bilayer of a mitochondrion. Furthermore, one cannot easily know, and cannot easily measure, the width of the binding potential well (δ in Figure 3-3). Therefore, one cannot easily know or measure the "density" n_{bi} or n_{bo} of TMRE in the membrane compartment.

Binding constant per mg of mitochondrial protein:

Case I: $\Delta\Psi_m$ **= 0**:

The experimental quantity measured with regard to mitochondrial suspensions is the total amount of protein in mg. This is usually measured by the Bradford assay, which measures optical absorption at a specific wavelength and converts this to mg of mitochondrial protein using an agreed upon constant from the literature [182].

The inner volume of the mitochondria (matrix volume) is usually taken as 1-2 μl/(mg of mitochondrial protein). From this, the total # of TMRE molecules can be estimated in the matrix, given the quantity of mitochondrial protein measured via the Bradford assay, and the density of TMRE (in moles/μl i.e. molarity). At $\Delta\Psi_m = 0$, the molarity of TMRE is the same on the inside (matrix) and outside (buffer), which is easily measured.

For a given amount of mitochondrial protein in mg, how many TMRE molecules are bound to the surface? This can be expressed as moles/(mg mitochondrial protein). For a given amount of mitochondrial protein in mg, how much "volume" of membrane binding compartment is there? (This would be in Figure 3-3 the membrane surface area times δ.) This would be expressed as μl/(mg mitochondrial protein).

Matrix side:

(Considering the matrix side first): Rottenberg [108] defines "apparent internal partition coefficient" K_i' as our a_i times the membrane volume V_{mi} per mg mitochondrial protein:

$K_i' \equiv a_i V_{mi}$ / (mg mitochondrial protein)

With these units, for a concentration n_i of TMRE in the matrix, the # of bound TMRE molecules would be:

(eq. 1) # bound TMRE molecules (matrix side) = $n_{bi}\ V_{mi} = a_i\ n_i\ V_{mi} = K_i'$ (mg mitochondrial protein) n_i

From Rottenberg, 1984 [108]:

> *The membrane volume occupied by the phospholipids on the matrix and cytosolic surface of the inner membrane is approximately half the volume of the total phospholipids of the inner membrane. Quite likely the lipophylic cations occupy only a fraction of this volume. While this volume fraction is unknown it is proportional to the total membrane volume and therefore to the membrane protein content which is routinely measured. In the applications that follow the apparent surface membrane concentration is expressed in units of nmol/mg protein. The units of the apparent partition coefficients K', (nmol/mg protein)/(nmol/ μl), are therefore expressed in μl /mg protein.*

These units are confusing, but they are what Rottenberg [108] chose to use, and also authors since then [101,180] have used this nomenclature. Similarly, the # of free TMRE molecules in the matrix can be expressed as:

free TMRE molecules (in matrix) = $n_i\ V_i$

Again, one does not know the internal volume V_i easily. However, since the inner volume of the mitochondria (matrix volume) is usually taken as 1-2 μl/(mg of mitochondrial protein), one can calculate:

(eq. 2) # free TMRE molecules (in matrix) = $n_i\ V_i$ = (mg mitochondrial protein) (2 μl/mg) n_i

On comparison with the formula for the # of bound TMRE molecules, one can see the K_i' has units of μl/mg.

Rottenberg and other authors have expressed experimentally determined binding constants as K_i'.

In comparing eq. 1, 2, once can see that if K_i' > 1-2 μl/mg, more TMRE is bound to the membrane than is free in the matrix, i.e. the ratio is:

bound TMRE molecules (matrix side) / # free TMRE molecules (in matrix) = K_i' / (1-2 μl/mg).

Scaduto[98] found, for TMRE at 28 C, K_i'= 60 (Table 1, Scaduto). ***This indicates 60x more TMRE molecules are bound to the inner membrane (matrix side) than free TMRE molecules in the matrix (at*** $\Delta\Psi_m$ ***=0).***

Buffer side:

A similar line of definitions applies for binding to the outer side of the membrane (the buffer side):

$n_{bo} = a_o\ n_o$

$K_o' \equiv a_o\ V_{mo}$ / (mg mitochondrial protein)

(eq. 3) # bound TMRE molecules (buffer side)
= $n_{bo}\ V_{mo} = a_o\ n_o\ V_{m0} = K_o'$ (mg mitochondrial protein) n_o

In comparing eq. 1, 3, once can see that if K_o' > 1-2 μl/mg, more TMRE is bound to the membrane than is free in the matrix, i.e. the ratio is:

bound TMRE molecules (buffer side) / # free TMRE molecules (in matrix) = K_o' / (1-2 μl/mg).

Scaduto[98] found, for TMRE at 28 C, K_i'= 129 (Table 1, Scaduto). ***This indicates 129x more TMRE molecules are bound to the outer membrane (buffer side) than free TMRE molecules in the matrix (at*** $\Delta\Psi_m$ ***=0).***

Case II: $\Delta\Psi_m \neq 0$:

If $\Delta\Psi_m \neq 0$, the free concentration ratio is governed by the Nernst equation:

$n_i/n_o = e^{(-q\Delta\Psi_m /k_BT)}$,

From equation 3, the # bound TMRE molecules (buffer side) do not change from the $\Delta\Psi_m$ = 0 value.

From equation 2, the # bound TMRE molecules (matrix side) do change from the $\Delta\Psi_m = 0$ value, and it becomes larger by the factor $e^{(-q\Delta\Psi_m / k_B T)}$.

Both cases are shown for n_o = 10 nM in Figure 3-3.

APPENDIX B. COMPARISON OF AIRYSCAN AND STED

The Airyscan functions by reducing the point spread function, while STED functions with a donut photobleaching. Depending on the conditions, Airyscan can have a resolution down to 90 nm with Airyscan Joint Deconvolution. In principle, STED can have a much better resolution, down to 20 nm. STED is very dependent on the bleach pump intensity and dye characteristics, while Airyscan is not. For this reason, it has been believed that Airscan is gentler on mitochondria, which are particularly sensitive to phototoxicity. However, it is possible to perform STED on live cells and mitochondria, at least for short periods of time. Note that STED's super-resolution only happened in the red emission range (~600-700 nm), which also depends on the property of the dye used. If one tries to image in the green emission range (~500-550 nm), the resolution one can get is only confocal resolution (~250 nm). Therefore, one should be aware of the fluorescence requirements for use in the experiments.

We have performed STED and Airyscan imaging on mitochondria isolated using the same protocol (other than the imaging technology), in order to compare the two approaches. For structural studies, the resolution of STED was significantly better than Airyscan. The Full-width-half-maximum (FWHM) analysis gave us a 140 nm resolution of Airyscan with NAO dye and an 80 nm resolution of STED with MitoTracker DeepRed (MTDR) dye. This is consistent with the two prior studies of mitochondria in cells which quoted the resolution [95–97,133], which found ~50 nm and 80 nm, 35-71 nm, and 45 nm, respectively. Those studies did not approach the ultimate resolution of STED of 10 nm, presumably because the dyes were not optimized and the pump intensity needed to achieve those resolutions would have killed the cells instantly. Thus, for structural imaging STED is clearly outperforming Airyscan, in terms of resolution, for imaging of intact functional mitochondria.

In our work, we are more interested in functional assays. Since the mitochondria are intact and functional, they should sustain a membrane voltage, and we aimed to find the method with the best possible resolution. To our knowledge, at this time there is not a STED optimized lipophilic cationic dye that can image voltages with the full potential of STED. Therefore, we used TMRE for voltage imaging. Attached image shows a line profile of TMRE-labeled mitochondria imaged under nominally identical conditions, optimized for the specific method, for both Airyscan and STED. We find a FWHM of 140 nm and 145 nm for Airyscan and STED, respectively, indicating that both methods provide comparable spatial resolution for voltage imaging. Hopefully, future research on new voltage dyes that are more optimized for STED can improve the spatial resolution beyond this.

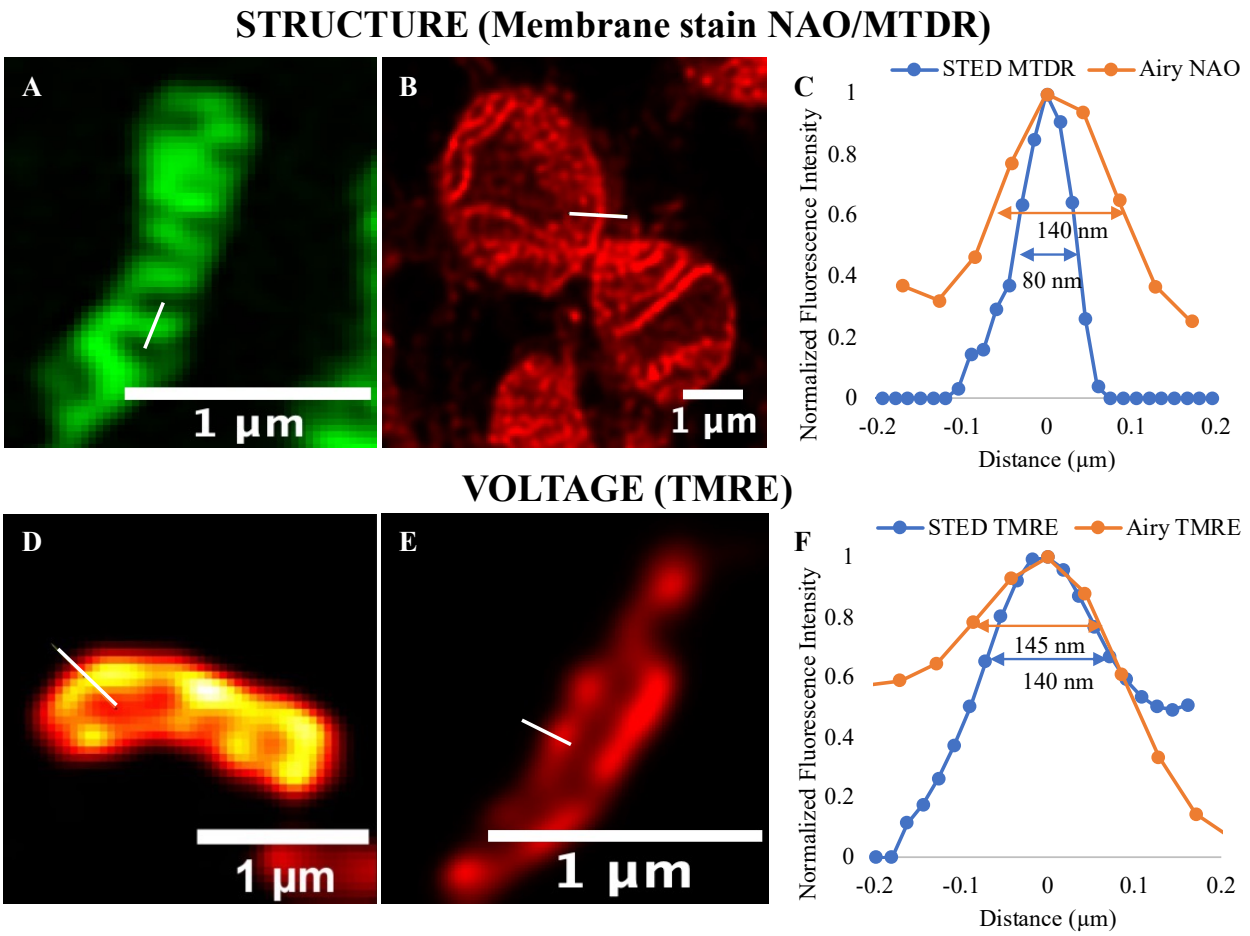

Appendix 1. Line profile of mitochondria STRUCTURE image (A) NAO + Airyscan and (B) MTDR + STED. (C) Image resolution comparison on structure image (Normalized intensity, Full-width-half-maximum (FWHM)). Line profile of mitochondria VOLTAGE image with (D) TMRE +Airyscan and (E) TMRE + STED. (F) Image resolution comparison on voltage image (Normalized intensity, FWHM).

APPENDIX C. MITOCHONDRIA CIRCULARITY ANALYSIS CODE FOR CHAPTER 4

The code used to analyze mitochondria circularity below can also be accessed on the github (https://github.com/shiown026/mitoAnnotation).

mitoAnnotation

The ImageJ macro file provide scripts to automatic annotate mitochondria and analyze its morphology in fluorescent images. The Segmentation is done by applying K-means clustering algorithm to separate mitochondria and the background by fluorescence intensity. In the Data forder, we have fluorescent images of mitochondria stained with 100 nM NAO as sample images. To run this macro, you will need additional plugins listed below.

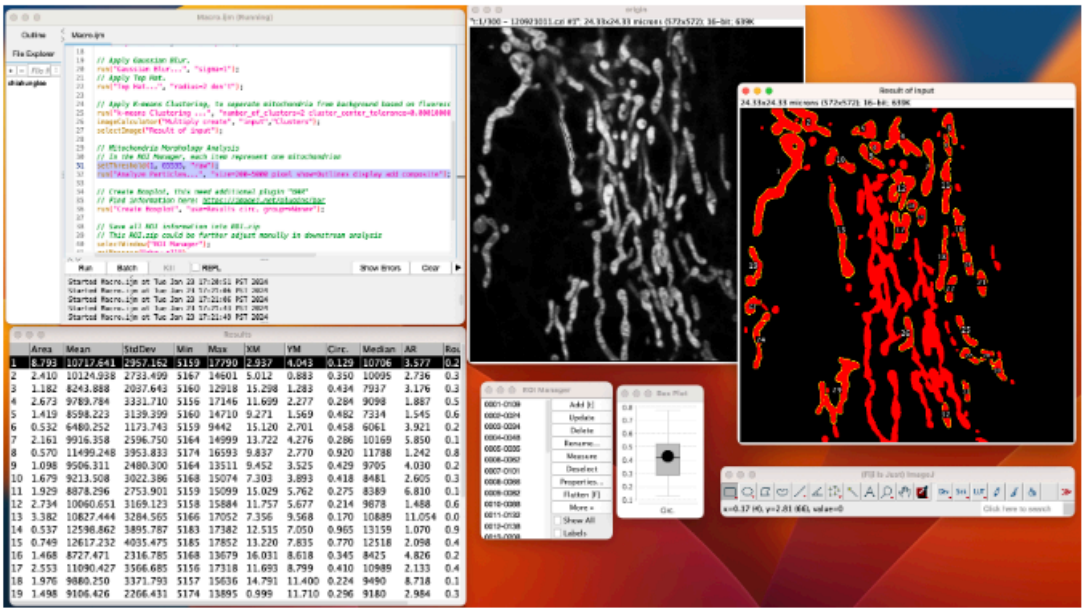

Appendix 2. Github: mitoAnnotation

```
// Set Measurement Parameters.

run("Set Measurements...", "area mean standard min center shape median redirect=None decimal=3");

// Clear records in Results Window.

run("Clear Results");

// Close all Windows

run("Close All");


// Clear records in roiManager.

if (roiManager("count")!= 0) {
```

```
        roiManager("show all");
        roiManager("delete");
        };

// Import 2D Image.
open();
rename("origin");
run("Duplicate...", "title=input");

// Apply Gaussian Blur.
run("Gaussian Blur...", "sigma=1");
// Apply Top Hat.
run("Top Hat...", "radius=2 don't");

// Apply K-means Clustering, to seperate mitochondria from background based on fluorescence intensity.
run("k-means Clustering ...", "number_of_clusters=2 cluster_center_tolerance=0.00010000 enable_randomization_seed randomization_seed=48");
imageCalculator("Multiply create", "input","Clusters");
selectImage("Result of input");

// Mitochondria Morphology Analysis
// In the ROI Manager, each item represent one mitochondrion
setThreshold(1, 65535, "raw");
run("Analyze Particles...", "size=200-5000 pixel show=Outlines display add composite");

// Create Boxplot, this need additional plugin "BAR"
// Find information here: https://imagej.net/plugins/bar
run("Create Boxplot", "use=Results circ. group=*None*");
```

```
// Save all ROI information into ROI.zip
// This ROI.zip could be further adjust manully in downstream analysis
selectWindow("ROI Manager");
roiManager("show all")
roiManager("Save","");

// Save Results to .csv
saveAs("Results", "");
```

APPENDIX D. AIRYSCAN TUTORIALS

This tutorial is for new users to learn how to use the basic functions of the Zeiss Airyscan microscopy. In the tutorial, we have prepared 2 exercises for reader to get familiar with the whole process of using Airyscan for imaging bio samples.

Exercise 1: we use a calibration chip to go through basic image localization, acquisition, saving to post image processing. By following all steps, one will be able to quickly get familiar to the basic manipulation of the Airyscan.

Exercise 2:

This tutorial writeup is mainly for system setup and sample loading. For the detail of operation, Please see the movie for step-by-step introduction

To start, make sure you have the following item ready first:

1. Zeiss Airyscan Microscopy
2. The immersion oil for lens
3. The sample calibration chip

Starting up the system

To starting up the system, follows the steps below:

1. Turn on the power switches "**SYSTEM**" on the main rack.
2. Turn on the power switches "**COMPONENTS**" on the main rack.
3. Turn on the **main power strop** affixes to the left side of the air table.
4. Turn on the **PC power**.

* Once the experiment is done, **reverse the starting up process to turn off the system**.

Launching the Zen 3.5 software

To starting up the software:

1. Double-click on the ZEN 3.5 (blue edition).

2. Select the "**ZEN system**" option to initialize the hardware. ("**ZEN image processing**" is used for offline data viewing)

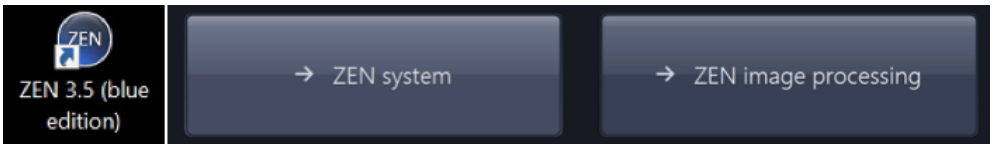

Sample setup on Airyscan microscopy

In this tutorial, we use the calibration chip (Convallaria) to go through the whole process of the bio-sample imaging. The following figure shows the User Interface for Airyscan. The Interface contains (1) the control panel, (2) the observation panel, (3) the channel and threshold panel, and (4) Image gallery and stage controller.

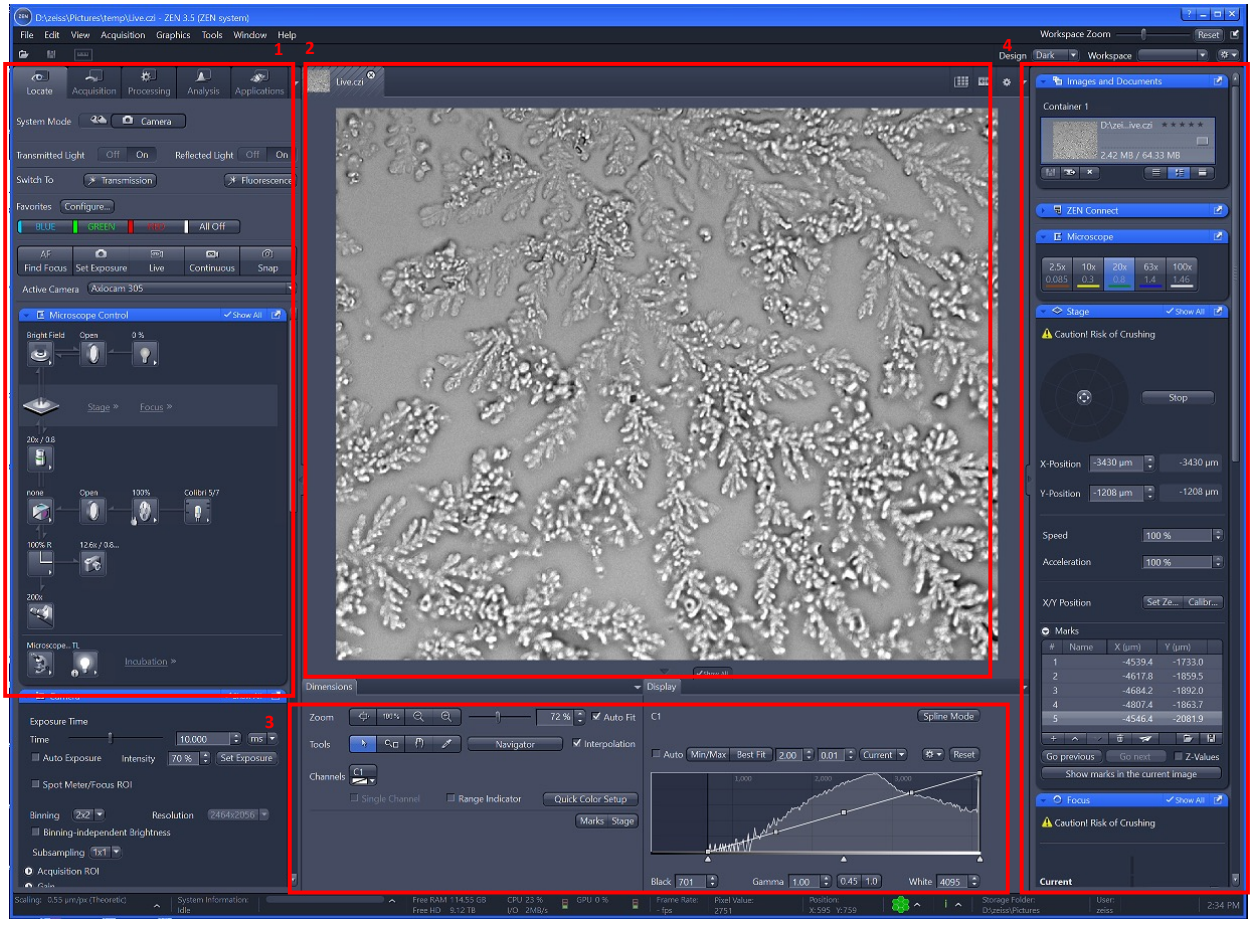

The following are steps to setup the bio-samples:

1. Select the appropriate objective for examining the slide/dish.

a. Start with 20x LED light for localization, adjust intensity within 8-15% for the LED.

2. Once located the cell of interest, change the lens to higher magnitude for detail imaging.
3. If using oil immersion (63x, 100x), add a drop of oil (w/o 30: for normal temperature environment, w/ 30: for high temperature environment) directly to the objective front lens.
4. Place samples on the stage with the coverslip facing downwards.
5. Use the stage XY joystick to center the objective front lens over the area of interest.

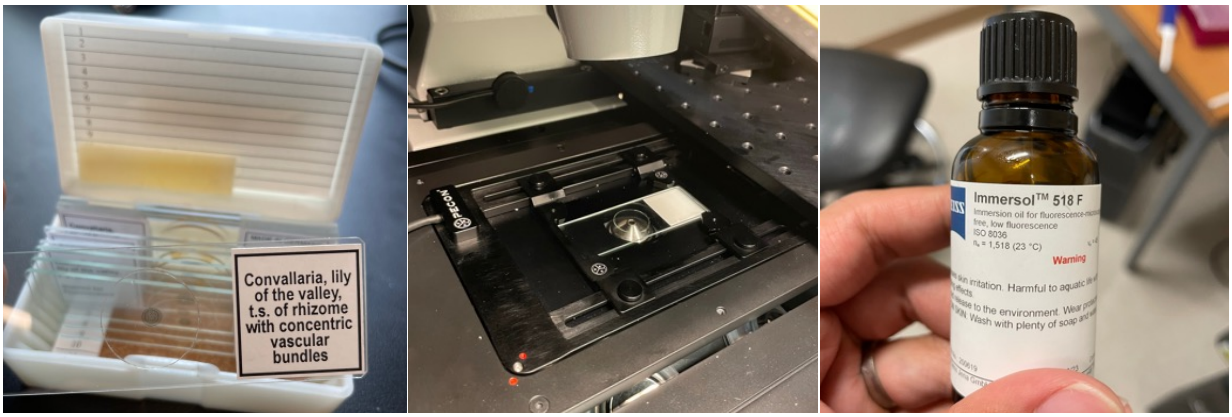

The control panel (1) contains the main tabs for microscope and camera settings (**Locate** tab), image acquisition (**Acquisition** tab), image processing (**Processing** tab), and image analysis (**Analysis** tab). The main tabs are organized in an order which follows the typical workflow of experiments in bioscience or material science. Once the sample is set up, push the "**Transmission**" button to turn on the light for white-view imaging. You can use the "**Fluorescence**" button for fluorescent imaging. The "Live" button is for live imaging and the "**Snap**" button is for taking a snap image.

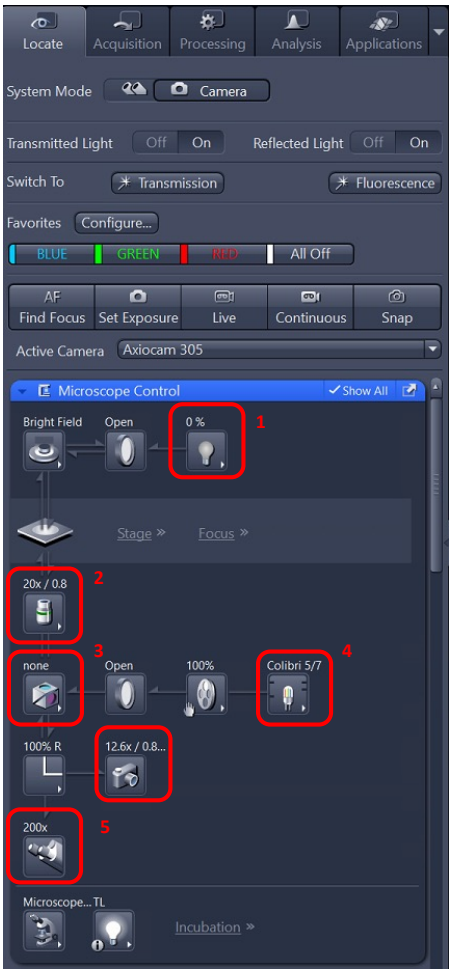

At the "**Microscope Control**" panel, we can:

1. Adjust the light intensity for white-view imaging.
2. Change the objective lens.
3. change.
4. Adjust the laser intensity for fluorescent imaging.
5. Change the observation mode between eyes and camera.

APPENDIX E. PROTOCOL FOR CELL CULTURE

This protocol is for whoever want to learn growing cells for experiment and preparing samples for Zeiss Airyscan imaging. We will cover the common cell culture skills to maintain a cell line for long-term experiment use. The method described here are built on the condition and utilities in the BurkeLab, one can change the content if the condition changes.

E-1. Chemical preparation and purchase links:

Here we listed the chemicals and preparation protocols that will be used in cell culturing. We also listed out the purchase link to the items. Note the protocols in this document is designed the condition and utilities in the BurkeLab. One should consider the requirements of their own experiment to make adjustment to the chemicals.

1. Cell culture medium (store in 4 °C)
   - DMEM/F-12, HEPES, 500 ml (https://www.thermofisher.com/order/catalog/product/11330057)
   - Fetal Bovine Serum, qualified, United States, 50ml (https://www.thermofisher.com/order/catalog/product/26140079?SID=srch-srp-26140079)
   - Penicillin-Streptomycin, 5ml (https://www.sigmaaldrich.com/US/en/product/sigma/p0781?gclid=Cj0KCQjw18WKBhCUARIsAFiW7JwsMld8NV1lt849tff7tiTCQEwLAq59GtZEJDvgBZBx28-5Hb5VLJ4aAuv5EALw_wcB)
   - MEM Non-Essential Amino Acids Solution (100X), 5ml (https://www.thermofisher.com/order/catalog/product/11140050)
   - Sodium Pyruvate (100 mM), 5ml (https://www.thermofisher.com/order/catalog/product/11360070)
   - L-Glutamine (200 mM), 5ml (https://www.thermofisher.com/order/catalog/product/25030081)

2. Trypsin (store in -20 °C)
   - Gibco Trypsin-EDTA (0.25%), phenol red (https://www.thermofisher.com/order/catalog/product/25200056)

3. PBS (store in room temperature)
   - Gibco PBS, pH 7.4 (https://www.thermofisher.com/order/catalog/product/10010049)

4. DMSO (store in 4 °C)
   - Dimethylsulfoxide (DMSO) (https://www.atcc.org/products/4-x)

E-2. thawing cells (from -80 °C freezer)

This step is used when starting the new cell lines.

Material:

1. Cell culture medium x 1.
2. PBS x 1.
3. Frozen cell vial from -80 °C freezer x 1.
4. 15 ml falcon tube x1

Steps:

1. Prepare the warmed up the cell culture medium in the 37 °C water bath for 20 min.
2. **(Important)** Took out the Frozen cell vial from the freezer and put it into the 37 °C water bath quickly. Be careful not to submerge the vial to avoid contamination. Shake the vial with hands until all thawing into liquid.
3. Quickly move the cell solution into 15 ml falcon tube.
4. **(Important)** Slowly add the warmed cell culture medium into the falcon tube. Add first 3-5 drops slowly to avoid temperature shock to the cells. Make the final solution to 10 ml in the falcon tube and pipette the solution to make the cell well-dispersed in the solution.
5. Centrifuge the cell solution with 1500 rpm for 5 min to pellet the cells.
6. Removed the supernatant and resuspend the cell pellet in 3 ml fresh medium.
7. Add 1 ml cell solution into culture flask with another 9 ml fresh medium solution addition. Mix well the solution by shaking the flask around.
8. Put the flask into incubator. Check the cell attachment after 24 hr incubation.

Reference:

https://www.youtube.com/watch?v=4HxqQOHifkU&t=83s

E-3. Freezing cells for long-term preservation

This step is used to store the cells for future use.

Material:

1. Cell culture medium x 1.
2. Trypsin x 1
3. PBS x 1.
4. DMSO x 1
5. Cell vial x 2
6. 15 ml falcon tube x1

Steps:

1. Prepare the warmed up the cell culture medium, trypsin in the 37 °C water bath for 20 min.
2. Prepare 5 ml freezing solution with 7% DMSO (4650 µl medium + 350 µl DMSO)
3. Take out the flask of cell from the incubator. Remove the medium solution inside with vacuum sucker and wash the cells with PBS for 2 (or more) times.
4. Add 5 ml warmed Trypsin into the flask and put the flask back into the incubator for 3 min.
5. Take the flask out from the incubator, watch if the cells are detached (tapping on the edge to check). If not, put the flask back to the incubator for another 1 min and recheck.
6. Add 5 ml warmed medium into the flask and pipette to mix the solution well.
7. Move the solution into falcon tube and centrifuge the cell solution with 1500 rpm for 5 min to pellet the cells.
8. Removed the supernatant and resuspend the cell pellet in 3 ml freezing solution.
9. Add 1.5 ml cell solution to each vial, put them in vial container and store in -80 °C freezer.

Reference:

https://www.youtube.com/watch?v=dXMG_R8vh18&t=16s

E-4. Passaging cells for long-term culture

This step is used to passage cells (remove excess cells keep growing cells) for long-term culturing. This protocol is designed to perform every 4 days.

Material:

1. Cell culture medium x 1.
2. Trypsin x 1
3. PBS x 1.
4. Flask of cells x 1 (75 ml)
5. 15 ml falcon tube x1

Steps:

1. Prepare the warmed up the cell culture medium, trypsin in the 37 °C water bath for 20 min.
2. Take out the flask of cell from the incubator. Remove the medium solution inside with vacuum sucker and wash the cells with PBS for 2 (or more) times.
3. Add 5 ml warmed Trypsin into the flask and put the flask back into the incubator for 3 min.
4. Take the flask out from the incubator, watch if the cells are detached (tapping on the edge to check). If not, put the flask back to the incubator for another 1 min and recheck.
5. Add 5 ml warmed medium into the flask and pipette to mix the solution well.
6. Move the solution into falcon tube and centrifuge the cell solution with 1500 rpm for 5 min to pellet the cells.
7. Removed the supernatant and resuspend the cell pellet in 3 ml fresh medium.
8. Add 1 ml cell solution into culture flask with another 9 ml fresh medium solution addition. Mix well the solution by shaking the flask around.
9. Marked the passage # on the flask.
10. Put the flask into incubator. Check the cell attachment after 24 hr incubation.

E-5. preparing sample for airyscan imaging

This step is used to prepare the samples for Airyscan imaging. This step is usually done with passaging since they go through all the same process.

Material:

1. Cell culture medium x 1.
2. Trypsin x 1
3. PBS x 1.
4. Flask of cells x 1 (75 ml)
5. 15 ml falcon tube x1

Steps:

1. Prepare the warmed up the cell culture medium, trypsin in the 37 °C water bath for 20 min.
2. Take out the flask of cell from the incubator. Remove the medium solution inside with vacuum sucker and wash the cells with PBS for 2 (or more) times.
3. Add 5 ml warmed Trypsin into the flask and put the flask back into the incubator for 3 min.
4. Take the flask out from the incubator, watch if the cells are detached (tapping on the edge to check). If not, put the flask back to the incubator for another 1 min and recheck.
5. Add 5 ml warmed medium into the flask and pipette to mix the solution well.
6. Move the solution into falcon tube and centrifuge the cell solution with 1500 rpm for 5 min to pellet the cells.
7. Removed the supernatant and resuspend the cell pellet in 1 ml fresh medium.
8. Add 20 µl cell solution into 1980 µl fresh medium and pipette to mix well.
9. Add 500 µl solution per well to the cartridge. Put the cartridge into incubator for at least 24 hour for cell attachments.